Geomorphic evidence for geologically recent groundwater flow associated with the Cerberus Fossae magmatic and volcanic system, Mars

A Thesis

Presented in Partial Fulfillment of the Requirements for the

Degree of Master of Science

with a

Major in Geology

in the

College of Graduate Studies

University of Idaho

by

Matthew W. Pendleton

Major Professor: Simon Kattenhorn, Ph.D.

Committee Members: Brian Yanites, Ph.D.; Gwen Barnes, Ph.D.; Amanda Nahm, Ph.D.

Department Administrator: Mickey Gunter, Ph.D.

June 2015

Authorization to Submit Thesis

This thesis of Matthew W. Pendleton, submitted for the degree of Master of Science with a Major in Geological Sciences and titled “Geomorphic evidence for geologically recent groundwater flow associated with the Cerberus Fossae magmatic and volcanic system, Mars,” has been reviewed in final form. Permission as indicated by the signatures and dates below, is now granted to submit final copies to the College of Graduate Studies for approval.

Major Professor: _____ Date: _____
Simon Kattenhorn, Ph.D.

Committee Members: _____ Date: _____
Brian Yanites, Ph.D.

_____ Date: _____
Gwen Barnes, Ph.D.

_____ Date: _____
Amanda Nahm, Ph.D.

Department Administrator: _____ Date: _____
Mickey Gunter, Ph.D.

Abstract

The Cerberus Fossae is one of the youngest large-scale tectonic landforms on Mars. An investigation of the geomorphology of the fossae margins and adjacent areas reveals a range of features indicative of surface modification. Volcanotectonic features indicate that dike intrusion was the driving mechanism behind fossae formation. Associated volcanic eruptions emplaced lavas that flowed away from the fossae down the regional slope. Volcanic deposits are incised by sapping features that formed along the fossae as a result of hydrothermal circulation. Magmatic heat may also have mobilized water to the surface where it combined with sediment to produce ice-rich flows that subsequently degraded in a similar manner to terrestrial periglacial features in response to seasonal thaw. The wide range of processes documented may provide context for the development of larger and more degraded fluvio-volcano-tectonic systems and expands our understanding of magma-surface interactions on Mars.

Acknowledgements

In completion of this document, I recognize the importance and quality of academic and scientific support from Professor Simon A. Kattenhorn. The training that Professor Kattenhorn bestowed on me will continue to act as a significant contributing factor towards my development into adulthood. Many individuals served as integral components to my scientific growth during and beyond my residence at the University of Idaho. Inclusive of its faculty, staff, and students, I thank the Department of Geological Sciences. The creativity that stemmed from worlds within which I travelled each and every day was amplified through extracurricular scientific-related activities. Of the many who influenced my actions, I specifically recognize Dr. Emily Martin, Dr. Amanda Nahm, Dr. Alex Patthoff, Alex Moody, James Muirhead, Kristina Pourtabib, Erika Rader, and Darin Schwartz. The scientific advancements presented in this thesis would not have been possible without funding from NASA, the University of Idaho College of Science, Alex Lindsay, Dr. Tom Smith, and Brad Zahlen. I thank Professor Devon M. Burr for our scientific collaborations. I acknowledge NASA for capturing image products utilized in my thesis. Lastly, to my family, I thank you for your love and support.

Dedication

i dedicate my thesis to Sir Alex Lindsay. Without Your high-level management of me, I would have never been able to graduate under the advisement of Professor Simon Kattenhorn.

Love, boy maddy.

Table of Contents

List of Figures

1. Introduction

The Cerberus Fossae, Mars which is a >1200 km long series of sub-parallel, steep-sided troughs located in central Elysium Planitia whose surface morphology suggests formation by volcanic dikes (Head et al., 2003; Mège and Masson, 1996). The term fossa (plural, fossae) refers to a long, narrow trough or depression on the surface of a planetary body, but has no explicit genetic affinity, and could thus result from a range of potential causes. The fossae are spatially related to Elysium Mons, extending somewhat radially from the volcanic center towards the east-southeast (Fig. 1). Past studies documented the close association of geologically very recent lava flows and fluvial channels emanating from Cerberus Fossae (Berman and Hartmann, 2002; Burr et al., 2002a, b; Head et al., 2003; Plescia, 1990, 2003). Results from these studies suggest that aqueous flow preceded volcanic eruptions and lava emplacement (Berman and Hartmann, 2002; Burr et al., 2002a; Head et al., 2003; Plescia, 1990, 2003). The source of both aqueous and volcanic fluids appears to be the Cerberus Fossae. The fossae are dated to the very Late Amazonian (< 20 Ma) based on the inferred age of the youngest surface that they crosscut (e.g., Berman and Hartmann, 2002; Burr et al., 2002a; Taylor et al., 2013).

The surface manifestation of the fossae has been variably hypothesized to be the result of subsidence-related depressions caused by magmatic melting of the cryosphere (Head et al., 2003), dike-induced faulting (Burr et al., 2002a; Hanna and Phillips, 2006; Taylor et al., 2013), or collapse into evacuated magmatic fissures (Pendleton et al., 2013). While significant aspects of the volcanic and fluvial history have been well documented, the primary formation mechanisms of the fossae have not been satisfactorily explained. Furthermore, the eroding capability of groundwater flow driven by hydrothermal systems along the fossae has not previously been determined (Craft and Lowell, 2012).

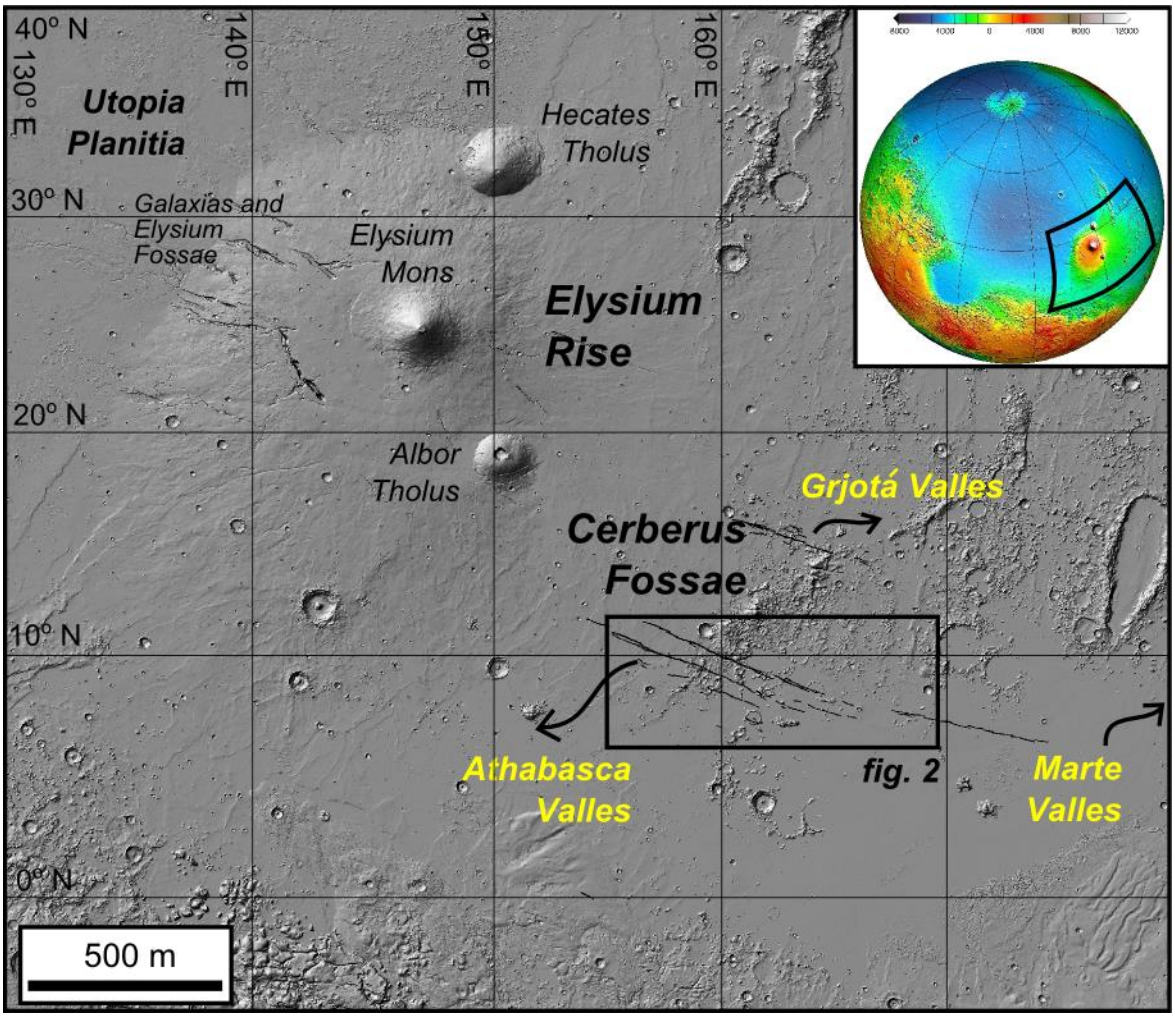

Figure 1. MOLA hillshade of the Elysium region (-5° N to 40° N, 130° E to 180° E; north is up) demonstrating the spatial relationship between the Elysium Rise, Cerberus Fossae, Galaxias and Elysium Fossae, and Utopia Planitia. The locations of three megaflood channels are shown relative to the Cerberus Fossae with arrows indicating flow directions inferred by Burr et al. (2002a). The Cerberus Fossae are mapped with black lines in the southwest quadrant of the region shown in the figure.

Magmatic dike intrusion at Cerberus Fossae is hypothesized to have resulted in the release of pressurized groundwater to the surface (Burr et al., 2002a, b; Head et al., 2003). Dikes may also have initiated hydrothermal systems adjacent to the fossae by melting permafrost and ground ice (Head et al., 2003). The hydrothermal processes that would have occurred at Cerberus Fossae are likely to be similar to those proposed on Earth (Craft and Lowell, 2012). As hydrothermal systems have been linked to the origin of life on Earth (e.g., Baross and Hoffman, 1985), the Cerberus Fossae may provide clues to potential habitable environments elsewhere in the solar system (Craft and Lowell, 2012). It is therefore of critical scientific importance to identify potential sites of hydrothermal processes on Mars and elsewhere.

Nonetheless, few studies have found direct evidence of hydrothermal flow affecting the surface of Mars. Thomas (2012) interpreted incised channels and leveed flows adjacent to a series of pits associated with a wrinkle ridge near the Cerberus Fossae to have formed through multiple outflow events of fluids of different viscosities. Flume experiments demonstrate that channels like those described by Thomas (2012) can be formed by low viscosity fluids such as water and/or low-viscosity lava (Marra et al., 2014). The upper surface of a lava flow have been dated using crater retention ages to be ~11 Ma (Thomas, 2012), indicating the possibility of aqueous and volcanic eruptions at Cerberus Fossae in the Late Amazonian. The results of Thomas (2012) imply the presence of groundwater, but do not explicitly identify seepage landforms that can result from hydrothermal circulation. Head et al. (2003) propose late-stage melting contributed to mass wasting processes that affected the geomorphology of the fossa as they are expressed today; however, this mechanism is not supported by morphologic evidence suggestive of groundwater modification of Cerberus Fossae.

A suite of landforms located near the source of the megaflood channel Athabasca Valles provides some evidence that ground ice may persist in areas proximal to the Cerberus

Fossae (Balme and Gallagher, 2009). The surfaces are characterized by polygonal textures that are bound by erosional scarps with indented cirque-shaped niches. Morphologically, these features are consistent with retrogressive thaw slumps (RTS), which are landforms typical of terrestrial periglacial environments (Lantuit and Pollard, 2008). RTS landforms imply the presence of surficial liquid water, which may have been supplied by thawing of ground ice and would be indicative of geologically-recent thaw degradation of ice-rich terrain at Cerberus Fossae (Balme and Gallagher, 2009). While seasonal thaw has been proposed as the mechanism for the melting of ground ice (Balme and Gallagher, 2009), residual heat from magmatic dike intrusion beneath the Cerberus Fossae may also have contributed to local thermal perturbations within the crust that contributed to melting.

Other morphology-based studies at Cerberus Fossae suggest that the surfaces on which RTS landforms exist are of a purely volcanic lithology that were not modified post-emplacement (Jaeger et al., 2010). Convincing lines of evidence in support of a volcanic interpretation include the presence of platy-ridged lava textures (Jaeger et al., 2010; Keszthelyi et al., 2004, 2008), rootless cones (Hamilton et al., 2011; Jaeger et al., 2007; Lanagan et al., 2001), and lava coils (Ryan and Christensen, 2012). These observations are diagnostic of basaltic flood lava flow fields on Earth, some of which closely resemble morphological landforms created by the 1783-1784 Laki eruptions in Iceland (Keszthelyi et al., 2004). Unlike terrestrial eruptive sites, however, the region adjacent to Cerberus Fossae lacks constructional landforms such as scoria cones and spatter ramparts that are diagnostic of the Laki-type volcanic fissure eruptions (Keszthelyi et al., 2004). Positive topographic landforms along the Cerberus Fossae may have been destroyed during subsidence of the fossa floor as a result of normal faulting (Keszthelyi et al., 2008), which is presumably the most recent geologic event at Cerberus Fossae (Berman and Hartmann, 2002; Burr et al., 2002a,b; Taylor et al., 2013). Alternatively, melting of ground ice by magma-driven hydrothermal systems may have contributed to the geomorphic modification of the fossa

walls (Head et al., 2003), masking the presence of primary eruptive structures contained within the fissures.

Landforms elsewhere on Mars demonstrate that the processes that created the Cerberus Fossae are not unique. For example, Memnonia Fossae and Elysium Fossae are morphologically consistent with the Cerberus Fossae and have been proposed to have formed through a similar sequence of events (Leask et al., 2007; Russell and Head, 2003). Like the Cerberus Fossae, Memnonia and Elysium Fossae are also oriented approximately radial to a volcanic rise (Elysium and/or Tharsis) and are proposed to be the result of dike-intrusion that fractured a cryosphere and released pressurized water from a subcryospheric aquifer (Leask et al., 2007; Russell and Head, 2003). Normal faulting at the tip of a propagating magmatic dike (Rubin and Pollard, 1988; Rubin, 1992) is the most straightforward formation process for Memnonia Fossae (Schultz et al., 2004) and Elysium Fossae (Russell and Head, 2003), however cryospheric melting in the region above the dikes may also have contributed to subsidence (Leask et al., 2007; Russell and Head, 2003). While detailed morphological assessments of Memnonia Fossae and Elysium Fossae have been performed (Leask et al., 2007; Russell and Head, 2003), there lacks compelling evidence for the presence of magma-driven hydrothermal systems at Martian fissure systems. As the Cerberus Fossae are the youngest volcanic-tectonic-fluvial feature on Mars, a detailed assessment of its geomorphology will provide insight into the possible existence of hydrothermal systems on Mars. The morphology of landforms at Cerberus Fossae, if affected by hydrothermal processes, may then be used as an analog for the development of older, more eroded fissure systems that may have formed through similar processes.

The intention of this study is to conduct a geomorphic investigation of the Cerberus Fossae to determine the presence of hydrothermal systems that may have resulted from dike intrusion and/or features indicative of magma-water interaction. An additional aim of this study is to distinguish features that formed through volcanic processes from those that

formed through non-volcanic processes, such as groundwater sapping, overland flow, and mass wasting. We postulate that hydrothermal systems adjacent to dikes intruded beneath the Cerberus Fossae may have melted ground ice and promoted hydrothermal circulation. Subsurface fluid flow may have promoted small, sediment-water (mass) flows at the surface as well as groundwater sapping that affected the morphology of the surface adjacent to the Cerberus Fossae. Surface flows away from the fossae may have solidified into icy deposits that were later modified by periglacial processes. We conducted a detailed geomorphic assessment to test these predictions. The results of our study suggest that groundwater flow occurred in the past several tens of millions of years at Cerberus Fossae.

2. Geological setting of the Cerberus Fossae

The Cerberus Fossae region (6-12° N; 154-174° E) is located southeast of the >1200 km wide Elysium rise in central Elysium Planitia (Fig. 1). The main part of the fossae consists of a cluster of four prominent, SE-trending parallel fissures. An individual fossa is up to 2 km wide, 1 km deep, and are up to ~1200 km long (Fig. 2). A second cluster of fissures, associated with Grjotá Valles, occurs parallel to, and 350 km north of, the main fissure cluster (Fig. 1). The Cerberus Fossae are young relative to other geological features in the area based on the observation that they crosscut local topographic highs and all craters along their length. They are likely to have formed in the Late Amazonian (Burr et al., 2002a; Jaeger et al., 2010; McEwen et al., 2005; Plescia, 2003) and are perhaps tens of millions of years old. All of the fissures are approximately radial to Elysium Mons and likely reflect magmatic intrusions (dikes) that propagated away from Elysium Mons driven by magma pressure in the central volcanic complex (Berman and Hartmann, 2002; Burr et al., 2002; Head et al., 2003; Plescia, 2003; Vetterlein and Roberts, 2010), typical of dike patterns on both Earth and elsewhere on Mars (Mège and Masson, 1996). Radial magmatic dike intrusions that propagated away from Elysium Mons, and which may have formed the Cerberus Fossae, may have been driven by flexural loading caused by the formation of the Tharsis and Elysium Mons regions (Hall et al., 1986; Hanna and Phillips, 2006). The association of Cerberus Fossae with dikes is evidenced by effusive products (i.e., lava) along the edges of the fractures, implying that they are eruptive fissures (Jaeger et al., 2007, 2010; Keszthelyi et al., 2000; Plescia, 2003), similar to those observed along Earth's rift zones, found in Iceland, East Africa, and Hawaii.

The Elysium rise is the second largest volcanic province on Mars and is ascribed to Late Hesperian to Early Amazonian (~3.3 to 2.9 Ga) (Hartmann and Neukum, 2001) volcanic and tectonic activity. The rise consists of three volcanoes: Elysium Mons and the two flank volcanoes, Albor Tholus to the south and Hecates Tholus to the north (Fig. 2) (Carr, 1973;

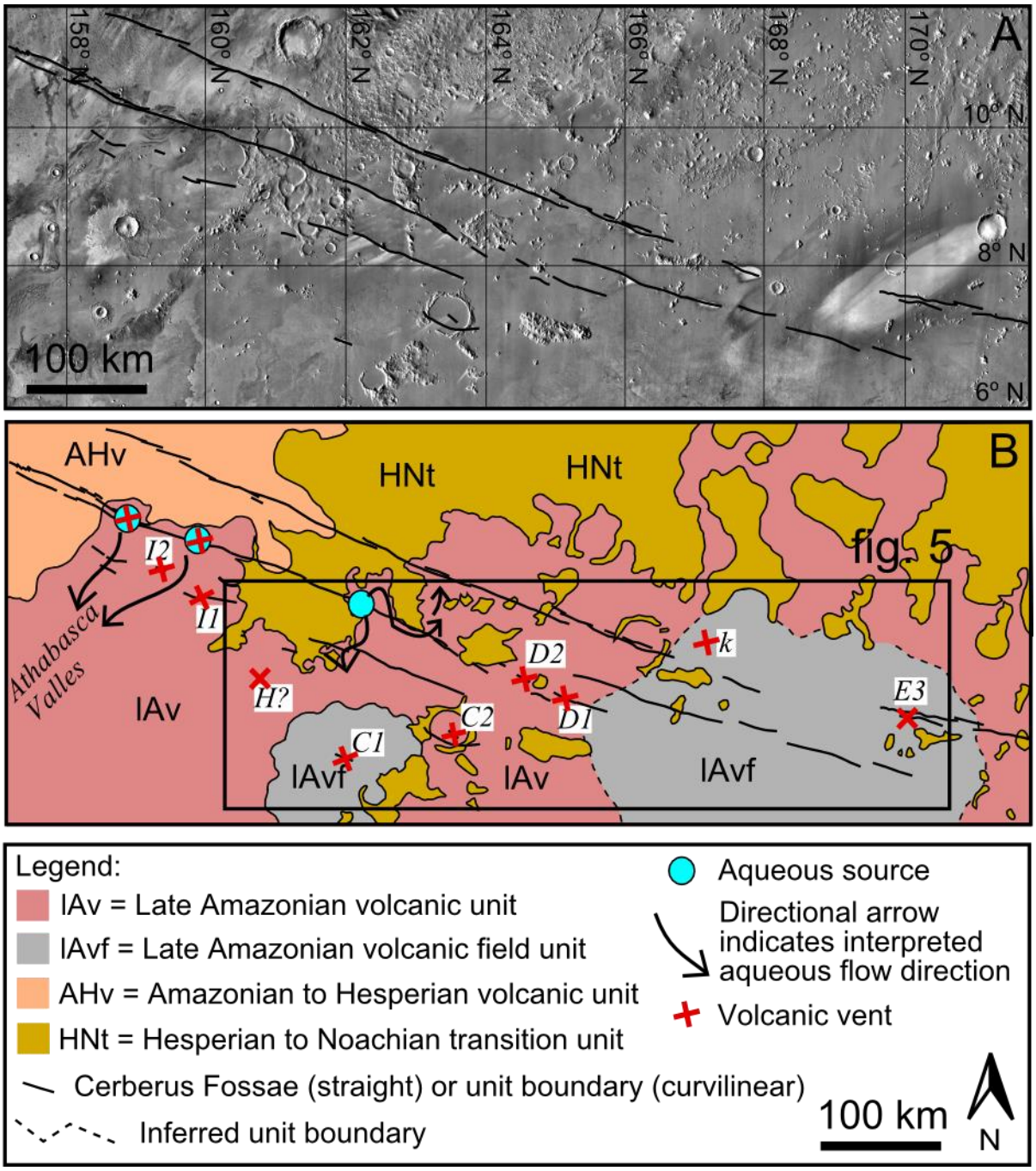

Figure 2. (A) THEMIS IR day image mosaic (resolution 100 m/pixel) from 6.00° to 11.80° N and 155.19° to 169.70° E, showing a portion of the Cerberus Fossae (black lines). Context is provided in Fig. 1. (B) Geomorphic map of (A), after Tanaka et al. (2014). Aqueous sources and directional flow indicators are taken directly from Vaucher et al. (2009). Black letters in white boxes correspond to volcanic vent sites identified by Vaucher et al. (2009).

Greeley and Guest, 1987; Tanaka et al., 1992, 2005). The Elysium rise is located along the southeastern rim of the large (>3300 km diameter) Utopia basin (Fig. 2). Based on the global geologic map of Tanaka et al. (2005), volcaniclastic deposits shed from the Elysium rise extend over an area of ~3.4 x 10^6 km^2 (Platz and Michael, 2011). This volcaniclastic unit corresponds to the Amazonian and Hesperian volcanic unit (AHv) mapped by Tanaka et al. (2014), which appears at the northwestern end of the Cerberus Fossae in Fig. 2. Unit AHv is comprised of stacked and gently sloping lobate flows that are meters to tens of meters thick and hundreds of kilometers long (Tanaka et al., 2014). These flows constitute the bulk of the Tharsis and Elysium rises and are interpreted to be flood lavas and large lava flows.

The western-most portion of the Cerberus Fossae (Fig. 2B) crosscuts AHv as well as three other geological units mapped by Tanaka et al. (2014). From youngest to oldest, these are (1) a Late Amazonian volcanic unit (lAv), (2) a Late Amazonian volcanic field unit (lAvf), and (3) a Hesperian and Noachian transition unit (HNt) (Tanaka et al., 2014). The youngest units constrain the formation of the Cerberus Fossae to within the past 20 Ma (e.g., Berman and Hartmann, 2002; Burr et al., 2002a; Taylor et al., 2014; Vaucher et al., 2009; Werner et al., 2003;). The age of the Cerberus Fossae thus dates to the very Late Amazonian and has been referred to by Plescia (2003) as one of the youngest large-scale features on the surface of Mars.

Fissure eruptions along the Cerberus Fossae emplaced the deposits that comprise the Late Amazonian volcanic unit (lAv) and the Late Amazonian volcanic field unit (lAvf) (Tanaka et al., 2014). The emplacement of lAv by eruptive fissures and shield edifices produced planar deposits containing steep-sided lobate flows that extend hundreds to more than 1000 km; lava channels, sinuous troughs, ridges, and platy textures are common. In contrast to unit lAv, the Late Amazonian volcanic field unit (laVf) was emplaced predominantly from low shields (i.e., not fissure vents), some of which have been described in detail by Plescia (2003), Keszthelyi et al. (2004), and Vaucher et al. (2009) (Fig. 2B).

The oldest geologic unit crosscut by the Cerberus Fossae in Fig. 2B is the Hesperian and Noachian transition unit (HNt) (Tanaka et al., 2014). HNt is composed of Noachian impact breccias, sediments, and volcanic deposits with intervening aprons of Hesperian mass-wasted materials (Tanaka et al., 2014). The unit may be tens to hundreds of meters thick and is interpreted to have experienced contraction in the form of wrinkle ridges. Mass wasting of the Cerberus Fossae walls have widened the fossae where they cross the looser and more unconsolidated unit HNt.

3. Volcanic aspects of the Cerberus Fossae

Volcanic eruptions from the Cerberus Fossae produced some of the better preserved flood lavas on Mars (Jaeger et al., 2010). Platy-ridged surfaces characterize the morphology of Cerberus-sourced flood lava deposits. Keszthelyi et al. (2004) document platy-ridged surfaces to be characterized by: (1) ridges tens of meters tall, tens of meters wide, and hundreds of meters long, (2) plates bounded by ridges, (3) smooth surfaces broken into polygons several meters across and bowed up slightly in the center, (4) parallel grooves, and (5) inflated pahoehoe margins. Jaeger et al. (2010) estimate that a single eruption from the Cerberus Fossae produced 5000–7500 km^3 of mafic or ultramafic lava, covering an area of ~250,000 km^2 in western Elysium Planitia. This sole eruption created the Athabasca Valles flood lavas, which occupy the megaflood channel of the same name (Jaeger et al., 2010; Fig. 2), and indicate that the Cerberus Fossae were associated with voluminous eruptive events.

By comparison to a single, well-preserved flood basalt flow on Earth, the Roza Member of the Columbia River Basalt Group, has a volume of 1300 km^3, an area of 40,300 km^2, and a maximum lava transport distance of ~300 km (Thordarson and Self, 1998; Tolan et al., 1989). Other large lava flow fields on Earth include the Deccan and Rajahmundry Traps, which span a total distance of ~1000 km (Self et al., 2008). Individual flow fields in the Deccan and Rajahmundry Traps cover 80,000-185,000 km^2 and may have exceeded 5000 km^3 (Self et al., 2008). The flood lavas at Cerberus Fossae are more aerially extensive than these large flood lavas on Earth and are of a similar volume (Jaeger et al., 2010).

The Mars Orbiter Camera on the Mars Odyssey spacecraft provided some of the first clues of volcanic deposits directly adjacent to the fossae. Smaller volcanic eruptions produced both thin lava flows and inflationary flows in closer proximity to the Cerberus Fossae (Burr et al., 2002b; Head et al., 2003; Keszthelyi et al., 2008). Head et al. (2003) propose that some of the deposits flanking the fossae are spatter-fed lava flows emplaced in a Hawaiian-style eruption. Keszthelyi et al. (2008) provide a more in-depth geomorphic study of the near-vent

deposits at Cerberus Fossae. Some of the documented lava surface characteristics include lava ponds with ridged boundaries, flow margins with smooth and rough surface textures, and shear-induced fractures that formed as mobile lava underlying a hardened slab induced stresses in the flow surface carapace (Fig. 3). Keszthelyi et al. (2008) also document flows that have raised surfaces with circular pits whose bottoms reside at the level of the original surface, called “amoeboid raised plateaus,” and are diagnostic of lava inflation (Keszthelyi et al., 2000, 2004).

Based on Mars Orbital Laser Altimeter (MOLA) topographic data and Mars Orbiter Camera (MOC) images, Plescia (2003) identified linear fissure vents and low shields within the Cerberus Fossae region, with associated lobate flows that extend downslope from the fissures (Fig. 3). Fissure vents result in elongate topographic highs, whereas low shields are more equant, having a localized summit vent and narrow flows that extend down the flanks. Low shields may represent sources that produced only limited amounts of lava for a short period of time at low eruption rates, whereas fissure vents would have produced lava at higher effusion rates (Plescia, 2003).

The locations of some of the identified low shields are shown in Fig. 2B, with labels that correspond to the mapping nomenclature of Vaucher et al. (2009). Their mapping included an assessment of the ages of thirty-five surfaces corresponding to volcanic vent products in the Cerberus Fossae region. Their results suggest that some volcanic features formed in the very Late Amazonian (~2 Ma), with eleven stages of volcanic activity that extends to at least 250 Ma.

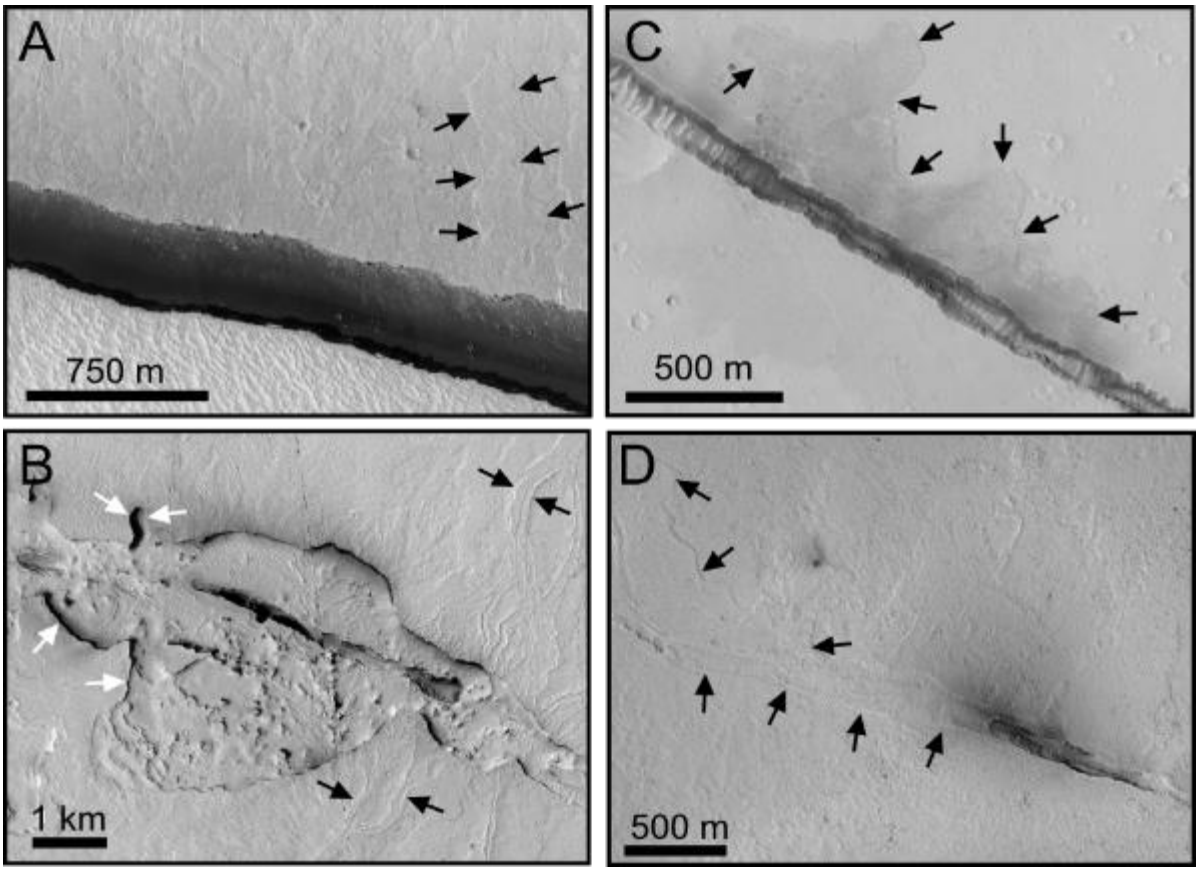

Figure 3. Lava flow morphologies associated with volcanic vents at Cerberus Fossae. Lava flow deposits are subtly defined in HiRISE images by albedo variations indicative of the perimeter of constructive flows. Black arrows point to flow boundaries. (A) Showing linear fissure with subtle flanking deposits; 9.220° N, 157.831° E; HiRISE observation ESP_023798_1895; vent I1 in Fig. 2. (B) White arrows identify a boundary adjacent to the fossa that confines a topographic low within the summit region of the vent; 6.915° N, 159.976° E; HiRISE observations PSP_003096_1870 and ESP_036048_1870; vent C1 in Fig. 2. (C) Linear vent with deposits associated along length; 10.665° N, 156.461° E; HiRISE observation PSP_007197_1910. (D) Inflationary lavas associated with linear vent; 7.708° N, 164.366° E; HiRISE observation PSP_003531_1880.

4. Hydrothermal systems on Mars: processes and landforms

4.1. Overview of hydrothermal systems on Mars

Hydrothermal systems exist where heat sources drive fluid circulation (e.g., Lowell, 1991; Lowell and Rona, 2004) (Fig. 4). Approximately a quarter of Earth's global heat flux is generated from hydrothermal flow in oceanic crust younger than ~65 Ma, with only a small fraction of heat loss from continental crust (Elderfield and Schultz, 1996). Analogous systems may have existed on Mars (Craft et. al., 2012). The formation of hydrothermal systems on Mars requires environmental conditions that allow for fluid stability near the surface and likely occur where volcanism and impacts generate large thermal gradients to drive fluid flow (Craft and Lowell, 2012). Hydrothermal processes have existed on Mars since the Noachian period (≥3.5 billion years ago), as evidenced by fluvial features associated with volcanic activity and hydrothermal deposits (Craft and Lowell, 2012). The Noachian period had a relatively denser atmosphere than at present (e.g., Jakosky and Phillips, 2001; Pollack et al., 1987) and rainfall may have been a primary contributor for outflows that carved surface features (Baker et al., 1991; Craddock and Maxwell, 1993; Gulick, 1998). Branching valley networks, that in plan view resemble terrestrial river systems, are common throughout Noachian terrain (Carr, 2012). Most Martian valleys that supposedly formed by aqueous flow are narrow and inset into an otherwise poorly dissected terrain (Carr, 2012). The valleys are mostly 1-4 km wide with U-shaped to rectangular cross sections (Carr, 2012). Larger, more prominent valleys, such as the circum-Chryse channels associated with Valles Marineris, that exceed 2000 km in length with depths up to 300 m and drain into local depressions (Carr, 2012).

Outflow channels and valleys are also interpreted to have formed more recently than the Noachian, when rainfall was not thermodynamically possible (Baker, 2001; Hamilton et al., 2011; Mouginis-Mark, 1990). In contrast to the early Mars precipitation-sourced outflow channels, younger outflow channels are more likely to have been generated by groundwater

outflow (Gulick and Baker, 1993; Gulick, 1993, 1998; Gulick et al., 1997) and the pressurized release of subcryospheric water (Fuller and Head, 2002; Head et al., 2003; Leask et al., 2007; Phillips and Hanna, 2006; Russell and Head, 2003). Landforms related to hydrothermal activity include valleys carved by either aqueous outflow events or groundwater sapping (Baker et al., 1992).

4.2. Magma-driven hydrothermal flow model

Gulick (1998) proposed conceptual and numerical models that outline the feasibility of the development of hydrothermal systems adjacent to magmatic intrusions on Mars (Fig. 4A). Their results find that a cylindrically shaped magmatic intrusion within the upper 3 km of a permeable ice-rich crust (Fanale, 1976; Rossbacher and Judson, 1981) initially results in conductive heat transfer between the intrusion and the country rock. As magma intrusion proceeds, heat will advect within the intrusion as a result of repeated injections, thereby increasing the rate of heat transfer to the surrounding water and ice (Craft and Lowell, 2015). Heat transfer occurs immediately after intrusion as the temperature of the magma body decreases. Following magma emplacement, the outer portion of the magma chamber starts to solidify, forming a low permeability outer shell of hot rock, the thickness of which increases with time (Gasparini and Mantovani, 1984). Thermal energy is carried into the surrounding country rock via conduction from the magma through the shell and then by convection into the saturated, permeable country rock. In this model, the shell is presumed to act as a physical barrier between the groundwater and the intrusion itself. The impermeable shell likely forms as a result of the cooling and contraction of the outer intrusion surface against the colder country rock.

Groundwater heated by the magma forms an upwardly moving buoyant plume of groundwater near the intrusion (arrows in Fig. 4A,B; Gulick, 1998).

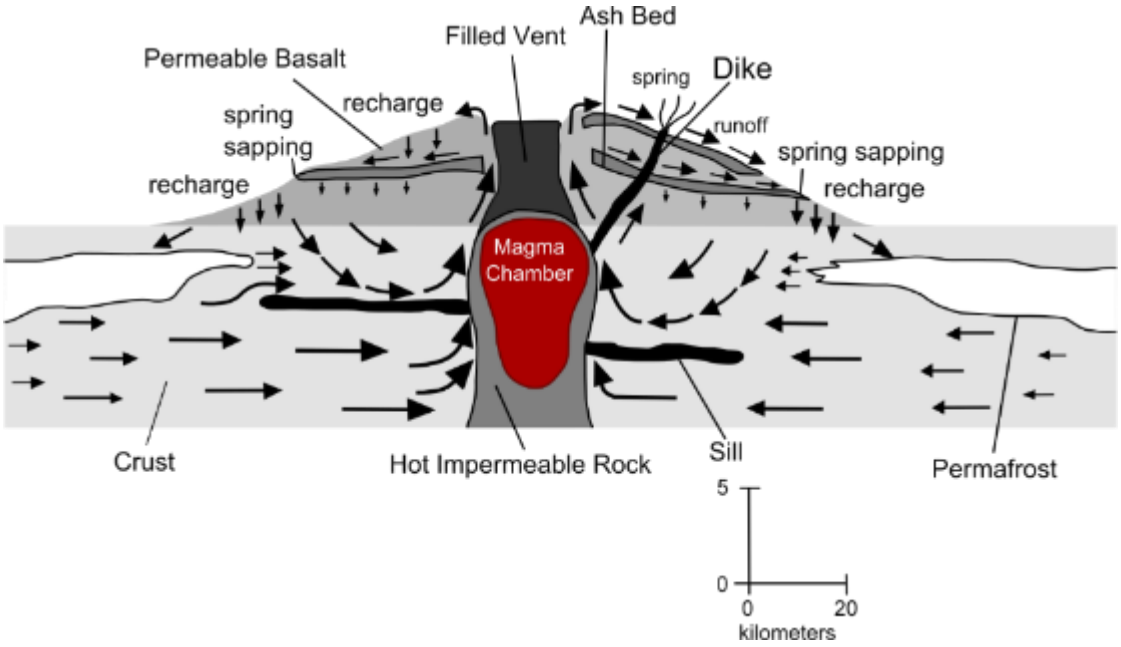

Figure 4A. Groundwater flow field within a vigorous hydrothermal system associated with a magmatic intrusion. Arrows indicate flow directions of water transport. Frozen groundwater is inferred to be present within permafrost lenses (e.g., near-surface aquifers) that are recharged as surface flows infiltrate permeable basalt that exist farther from the magma chamber. Crustal materials are presumed to be porous and able to facilitate groundwater flow. Relevant surface processes that may have occurred at Cerberus Fossae are highlighted, assuming hydrothermal activity was pronounced before, during, and/or after the formation of the fossae. Modified from Gulick (1998).

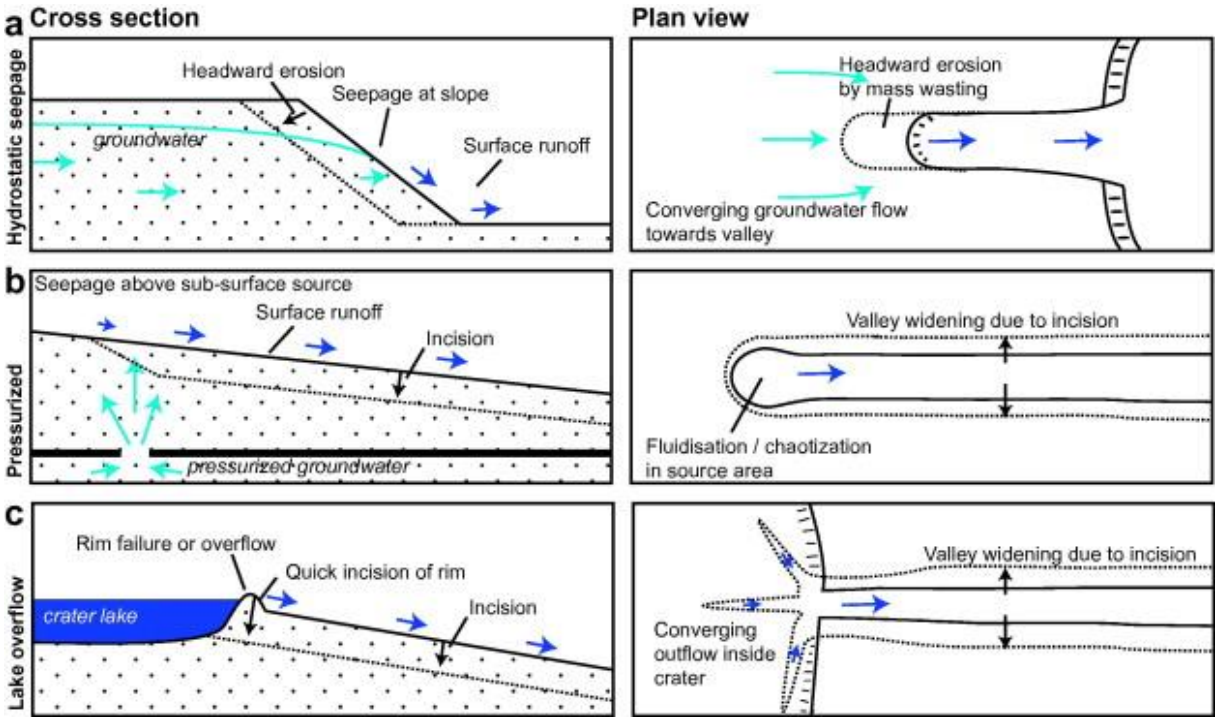

Figure 4B. Groundwater seepage scenarios proposed by Marra et al. (2014). Cross section and plan view images show subsurface process and the resultant geomorphology. Three scenarios are shown: (a) hydrostatic seepage, (b) pressurized flow, (c) crater-lake overflow. Taken from Marra et al. (2014).

As colder and denser groundwater flows in toward the intrusion from the surrounding regions, the buoyant plume is resupplied as long as a thermal gradient exists. Any groundwater that reaches the near-surface may then contribute to the geomorphic modification of that surface. Depending on the local hydrologic and lithologic conditions, surface runoff could re-enter the groundwater system in regions where the rate of infiltration is sufficiently high. However, if atmospheric conditions (e.g., temperature and pressure) do not favor liquids at the surface, groundwater would initially start to boil and evaporate but then freeze due to the heat liberated in the process of evaporation (Gulick, 1998). This process may result in an insulating ice-rich surface layer beneath which outflows of hydrothermal water may move as ice-covered rivers (Brakenridge et al., 1985; Carr, 1983; Wallace and Sagan, 1979).

Groundwater that does not reach the surface potentially recharges near-surface aquifers that may expand to the point of promoting future outflows (natural springs) that span progressively greater distances from the intrusion site (Gulick, 1998). The resultant groundwater sapping (i.e., erosion of the surface by groundwater outflow) can potentially develop into a dominant valley-forming process. Mantling of ash on the flanking surface above the intrusion caused by volcanic eruption may create a lower permeability layer than the underlying basalt and promote runoff. Groundwater processes may then erode subsurface regolith to create sapping valleys while surface flow incises fluvial networks.

The model proposed by Gulick (1998) (Fig. 4A) has been widely applied to conceptualize hydrothermal activity driven by magmatic systems on Mars (Baker, 2001; Berman and Hartmann, 2002; Burr et al., 2002a; Carr and Head, 2010; Craft and Lowell, 2012; Fuller and Head, 2002; Head and Wilson, 2002; Head et al., 2003; Leask et al., 2006, 2007; Pedersen, 2013; Russell and Head, 2003). Craft and Lowell (2012) expanded upon the Gulick (1998) hydrothermal flow model, modifying the parameters to determine the heat and

water outputs that would result from a sheet-like dike intrusion as opposed to the cylindrical intrusion originally modeled.

Craft and Lowell (2012) applied steady-state boundary layer models to a single phase, dike-driven hydrothermal system beneath the surface of Mars and demonstrated that dikes are capable of heat and liquid water outputs for a range of crustal permeabilities and dike dimensions. A heat output of ~1.8 x 10^{19} J yr^{-1} from a 10 km tall, 200 km long, 200 m wide dike, with a host rock permeability of 10^{-11} m^2 could produce ~20 km^3 yr^{-1} of liquid water and a cumulative total of ~6000 km^3 over its 300 year cooling history. These dike dimensions are comparable to those envisioned for a segment of the Cerberus Fossae that is regarded as the source of copious water that carved Athabasca Valles (Fig. 1) (e.g., Berman and Hartmann, 2002; Burr et al., 2002a,b; Plescia, 2003). The model results by Craft and Lowell (2012) thus quantitatively demonstrate the feasibility of producing subsurface and surface aqueous flow by dike-induced hydrothermal systems, which we hypothesize to be an important contributor to the geomorphic evolution of the Cerberus Fossae.

4.3. Landforms related to magma-driven hydrothermal processes on Mars

Few investigations have addressed Martian magma-driven hydrothermal systems and their effects on surface morphology (e.g., Craft et al., 2012; Leask et al., 2006). Sill intrusions have been proposed to induce hydrothermal systems on Mars as well as large-scale collapse structures, such as the Aromatum Chaos depression (Leask et al., 2006) in the Xanthe Terra region. The hypothesized sill induced tensile stresses in the cryosphere while enhancing the local heat flow at shallow depths, melting the ice-rich cryosphere. Pressurized water was then released from an underlying aquifer, creating the outflow channel system Ravi Vallis, located at 1.1°S, 317.0°E. Similarly, Coleman (2003) suggested that Aromatum Chaos formed through interactions between the cryosphere, hydrosphere, and intruding magma. Dike intrusions into the Martian cryosphere may have also generated hydrothermal

processes that affected the land surface. Head et al. (2003) postulated that dike intrusion into the cryosphere resulted in mass wasting into the developing Cerberus Fossae, although a specific model for fossae formation was not presented.

Landforms that develop as a result of the collapse of the surface in response to the removal of ground ice or volatiles were described by Sharp (1973) and referred to as chaotic terrain. These landforms include surfaces that comprise irregular patterns of angular blocks of various sizes (kilometers to tens of kilometers), many of which preserve the original morphology of the collapsed surface. The blocks are generally flat topped and appear to have collapsed along arcuate head scarps, producing alcove-like depressions (Chapman and Tanaka, 2002; Nummedal and Prior, 1981; Rodriguez et al., 2006). Sharp (1973) proposed that magmatic heat can induce melting and collapse of ground ice near the surface, whereas Soderblom and Wenner (1978) argue for erosion of flowing water in the subsurface, causing collapse and the formation of chaotic terrains. Alternatively, Zegers et al. (2010) suggest that water ice contained at a depth of 1-3 km may melt due to thermal insulation caused by the overlying sediment. As a result, the overlying material destabilizes as water escapes, creating chaos terrain.

Aqueous flows produced by hydrothermal circulation may potentially combine with loose sediment at the surface to form mass flows. A mass flow is a sediment-water mixture and can form with a range of sediment to water ratios. The term mass flow is used here in the general sense in contrast to the terms debris flows and hyperconcentrated flows, which have prescribed sediment to water ratios (≥60% and 20-60%, respectively) (Lavigne and Thouret, 2000; Vallence and Scott, 1997).

Unusual Early Amazonian-aged flow-like deposits that extend into Utopia away from deep radial fossae on the northwest flanks of the Elysium rise (Christiansen, 1981; Greeley and Guest, 1987; Tanaka et al., 1992) have been interpreted to be the result of lahars (Pedersen, 2013; Russell and Head, 2003). Lahar is the general term for a water-sediment

mixture that flows rapidly from a volcano (Smith and Fritz, 1989), implying that the sediment is composed of volcanic material such as ash. Terrestrial studies indicate that lahars can form during or after an eruption if there is abundant water and unconsolidated debris, steep slopes, and a triggering mechanism (Lavigne and Thouret, 2000; Vallence, 2000). Martian lahars have distinctive morphological properties such as smooth, lobate flow fronts with upward convex snouts and unusual crater morphologies (from later impacts onto their surfaces (Pedersen, 2013). Unlike terrestrial lahars, Martian lahars localize flow to their central regions as the outer margins of the flow freezes. The interior surface layer is ice-poor due to the downslope drainage of the fluid away from the source, whereas the margins form as a result of deposition and freezing of ice-rich flows when the lahar spills over the valley-confining walls.

If atmospheric conditions were suitable, ice-rich lahar deposits may have experienced high rates of thermal and mechanical erosion similar to periglacial landscapes on Earth that erode due to thawing permafrost and melting of ground ice (Lantuit and Pollard, 2008). Balme and Gallagher (2009) propose that surfaces to the immediate south of the Athabasca Valles source at Cerberus Fossae represents a periglacial environment that was affected by thawing permafrost. They identify a series of polygonally-patterned surfaces that are bounded by erosional scarps and indented with cirque-shaped niches whose morphology is controlled by the polygonal surfaces. The polygonal surfaces are contained within shallow basins that are interconnected through a series of narrow constrictions. Associated with the scarps are dendritic channels and gullies, blocky debris, and hummocky terminal deposits. Together, this suite of landforms in the region adjacent to the Cerberus Fossae are morphologically consistent with terrestrial retrogressive thaw slumps (RTS) (Balme and Gallagher, 2009), which are typical landforms of degrading periglacial and thermokarst environments on Earth (Lantuit and Pollard, 2008). Ground ice deposited by mass flows at Cerberus Fossae also may have degraded to produce morphological features consistent with

RTS landforms, similar to those identified by Balme and Gallagher (2009). If mass flows contributed to the emplacement of ice at Cerberus Fossae, the deposits may degrade and produce erosional scarps that are indented by cirque-shaped niches. We also may expect to find polygonal surfaces, channels, and gullies adjacent to the affected surfaces.

Hydrothermal systems also may promote the formation of sapping features at the surface above the intrusion where magmatic heat is localized (Gulick, 1998) (Fig. 4A). Groundwater sapping implies the undercutting of a slope in response to groundwater seepage (Marra et al., 2014). Sapping processes are grouped into two categories: (1) hydrostatic seepage, (2) pressurized seepage, and (3) crater lake overflow (Fig. 4B) . In the hydrostatic scenario, groundwater seepage is affected by landscape irregularities, such as topographic depressions or differences in hydrological parameters of the near-surface crustal rock or soil (Marra et al., 2014). This type of seepage has been observed to produce amphitheater-headed valleys in unconsolidated sand (Howard and McLane, 1988; Kochel and Piper, 1986). The amphitheater shape results from headward erosion by mass wasting caused by converging groundwater flow towards a topographic depression. In the pressurized aquifer scenario, water is released from a confined aquifer through a narrow constriction. Groundwater travels to the surface to produce undercutting of the slope and incises a channel as a result of surface runoff. In contrast to the amphitheater-headed valleys that develop in hydrostatic examples, the source area of a pressurized seepage example produces a distinct pit formed by the seeping groundwater. Experimental flume studies by Marra et al. (2014) demonstrate that the source pit has varied morphologies that is dictated by water pressure, with larger pressures generally resulting in larger source pits.

4.4. Evidence for ground ice within outflow channels at Cerberus Fossae

Two irrefutable outflow channels emanate from the Cerberus Fossae (Athabasca Valles and Grjotá Valles) (Fig. 1) (Berman and Hartmann, 2002; Burr et al., 2002a,b;

Plescia, 1990, 2003). A third outflow channel, Marte Valles, was initially identified by Burr et al. (2002a) on the basis of morphological features that reflect aqueous processes. Similar to the interpretations for Athabasca and Grjotá Valles, aqueous flow is hypothesized to have initially carved Marte Valles (Burr et al., 2002a; Fuller and Head, 2002; Morgan et al., 2012; Plescia, 2003); however, the aqueous source along the easternmost portion of the fossae is now buried beneath an approximately 80-m-thick stack of lava flows (Morgan et al., 2012) that masks the fossae surface expression (Burr et al., 2002a; Morgan et al., 2012; Plescia, 2003; Vaucher et al., 2009).

Aqueous fluids are envisioned to have been released both catastrophically (e.g., Berman and Hartmann, 2002; Burr et al., 2002a,b; Fuller and Head, 2002; Plescia, 2003) and non-catastrophically (Plescia, 2003) from the Cerberus Fossae to produce the outflow channels, Athabasca, Grjotá, and Marte Valles. The magmatic dike origin for the Cerberus Fossae (Berman and Hartmann, 2002; Burr et al., 2002a,b; Head et al., 2003; Mège and Masson, 1996) and the presence of a near-global sub-cryospheric aquifer (Clifford, 1993) promotes the interpretation that fracturing (Head et al., 2003) and/or faulting (Berman and Hartmann, 2002; Burr et al., 2002a,b; Phillips and Hanna, 2006; Plescia, 2003) associated with intrusion acted as the conduits for groundwater release, likely driven by hydrothermal circulation beneath the fossae (cf. Gulick, 1998; Fig. 4A).

The presence of rootless cones on the surface of both Athabasca (Jaeger et al., 2007, 2010) and Marte Valles (Hamilton et al., 2011) provide the most direct evidence for the existence of water ice in the near-surface environment at Cerberus Fossae (e.g., Lanagan, 2001). Rootless cones are also known as pseudocraters or phreatovolcanic constructs and appear as mounds that are generally tens to hundreds of meters in diameter with an enclosed, semi-circular shaped depression, similar to a crater, at their apex (Dundas and Keszthelyi, 2013; Jaeger et al., 2007). On Earth, rootless cones form when lava flows over wet ground, leading to steam explosions that build mounds atop the flow (Thorarinsson,

1953). While alternative explanations depict these cone-like features in Athabasca and Marte Valles as being ice-cored mounds (i.e., pingos) (Burr et al., 2005; Page, 2010), mud volcanoes, evaporite deposits, and/or springs (Ferrand et al., 2005; Keszthelyi et al., 2010), numerous morphology-based studies support their formation from lava flow over ground ice (Fagents et al., 2002; Fagents and Thordarson, 2007; Greeley and Fagents, 2001; Hamilton et al., 2010, 2011; Jaeger et al., 2007; Keszthelyi et al., 2010; Lanagan et al., 2001).

The presence of rootless cones within megaflood channels associated with the Cerberus Fossae implies ground ice was present prior to the volcanic eruptions that emplaced flood lavas in Elysium Planitia. Burr et al. (2002b) suggest that some of this ground ice was emplaced as a result of aqueous floods, such as the megaflood that carved Athabasca. In their model, Burr et al. (2002b) suggest that magmatic dikes may have melted ground ice and opened pathways for water to travel to the surface. Floodwaters may have initially carved Athabasca Valles and percolated through interconnected pores comprised of fractures and lava tubes where it would have been stored prior to the emplacement of the Athabasca Valles flood lava. At present, the specific mechanisms that resulted in the production of sufficient groundwater output to form valley-carving megafloods prior to volcanic emplacement remains unresolved (e.g., Dundas and Keszthelyi, 2013).

5. Data and methods

The detailed observations we report are based on grayscale images captured by the Mars Reconnaissance Orbiter's (MRO) Context Camera (CTX; 6 m/pixel) (Malin et al., 2007) and High Resolution Imaging Science Experiment (HiRISE; 0.25 m/pixel) (McEwen et al., 2007). We present CTX observations to provide context for smaller-scale features, surface textures, and fossa-adjacent surface morphologies that can only be identified using HiRISE images. HiRISE images that cover isolated field sites were individually downloaded as map-projected JP2 products in an equirectangular projection from <www.uahirise.org/[OBSERVATION_ID]>. CTX images were retrieved as unprojected products from <http://viewer.mars.asu.edu/planetview/inst/ctx[OBSERVATION_ID]> and manually georeferenced in an equirectangular projected ArcGIS environment.

Topographic measurements from the Mars Orbiter Laser Altimeter (MOLA) Precision Experiment Data Record (PEDR) dataset (Smith et al., 2003) are used to characterize the cross-strike topography of the landforms that occur in close spatial proximity to the Cerberus Fossae. MOLA PEDR data are a series of spot elevations taken along the orbital ground track of the Mars Global Surveyor (MGS) satellite. Spot elevations have a center-to-center along-track spacing of ~300 m and the footprint for each spot elevation measurement is ~168 m in diameter (Smith et al., 2003). The vertical precision of each measurement is typically <1 m (Neumann et al., 2001). It is important to note that the between-track distance between MOLA orbits at this near-equatorial location is up to 10 km and does not fully characterize the topography of any of the field sites we study. The large between-track distance is caused by the non-overlapping orbital tracks of the MGS satellite near the equator (Smith et al., 2003). MOLA PEDR were extracted from individual orbital tracks and the track number is provided in each of the constructed topographic profiles for the field examples that follow. MOLA PEDR data were downloaded from <http://ode.rsl.wustl.edu/mars/dataPointSearch.aspx> as shape files that were directly

imported into an equirectangular projection in ArcGIS. To supplement MOLA PEDR data, we use the elevations contained within a single CTX digital terrain model (DTM) that covers one of our study sites. The CTX DTM was derived using photogrammetric techniques.

The depths of the fossae can be difficult to constrain using MOLA data because of the 300 m point spacing, which commonly results in no more than a single data point within a fossa, the data point may not fall directly on the bottom of the fissure. In narrow fossae, no data points may fall at the base of the fossae and the 168 m footprint radius results in the elevations at the top of the fossae walls being incorporated into the average elevation recorded at that MOLA data point, significantly underestimating the fissure depth. To determine depths of fossae where MOLA data were not reliable (or present), and where the DTM did not provide sufficient data, fossa depth was calculated using an alternative method based on photoclinometry:

$$h = d \tan \theta \quad (1)$$

where h depth of the fossa, d is the shadow length measured in the direction that the shadow is cast, and θ is the angle of the sun above the horizon at the time the image was captured by MRO. Each HiRISE observation provides the angle of the sun above the horizon as well as the solar incidence angle. The solar incidence angle is defined here as the angle between a vertical line that is orthogonal to the Martian surface and the position of the sun above the horizon (90-θ). The parameters d and θ were retrieved from <www.uahirise.org/[OBSERVATION_ID].>

6. Observations and interpretations of surface morphologies at the Cerberus Fossae

We conducted detailed geomorphic assessments of six field sites along the >1200 km length of the Cerberus Fossae (Fig. 5). Landforms at the selected sites are morphologically unique and exhibit characteristics that significantly differ from past observations at Cerberus Fossae. Previous studies characterized large-scale flow-formed features (Burr et al., 2002a,b, 2004; Burr and Parker, 2006) and lava flow textures, dynamics, and emplacement processes proximal to the fossae (Berman and Hartmann, 2002; Jaeger et al., 2010; Keszthelyi et al., 2004, 2008; Russell and Head, 2003; Vaucher et al., 2009; Werner et al., 2003). In this study, we focus instead on smaller-scale, previously undocumented landforms directly adjacent to the fossae that provide insights into the past existence of hydrothermal systems at Cerberus Fossae.

We categorize the six field sites into three groups based on morphological attributes. Group 1 consists of fossa-adjacent, elongate depressions with smooth surfaces and simple boundaries. Group 2 consists of fossae flanked by irregular, orthogonal, or trough-like depressions. Group 3 consists of valleys in the Hesperian and Noachian transition unit that we interpret to have formed as a result of a flowing fluid. Each group contains two field examples. In each case, we present field observations of fossa-adjacent morphologies, followed immediately by the associated interpretations. A review of the observations and interpretations for all three groups and six field sites is provided at the end of this section. The field observations highlight the geomorphic variability of the fossae along the length of the system and demonstrate that the Cerberus Fossae did not form from a single event or process, but rather represent the end result of many competing surface processes associated with dike intrusion beneath ice-rich surface materials. The study shows that the Cerberus Fossae are associated with a variety of landforms that likely formed through a combination of fluvial, volcanic, and tectonic mechanisms.

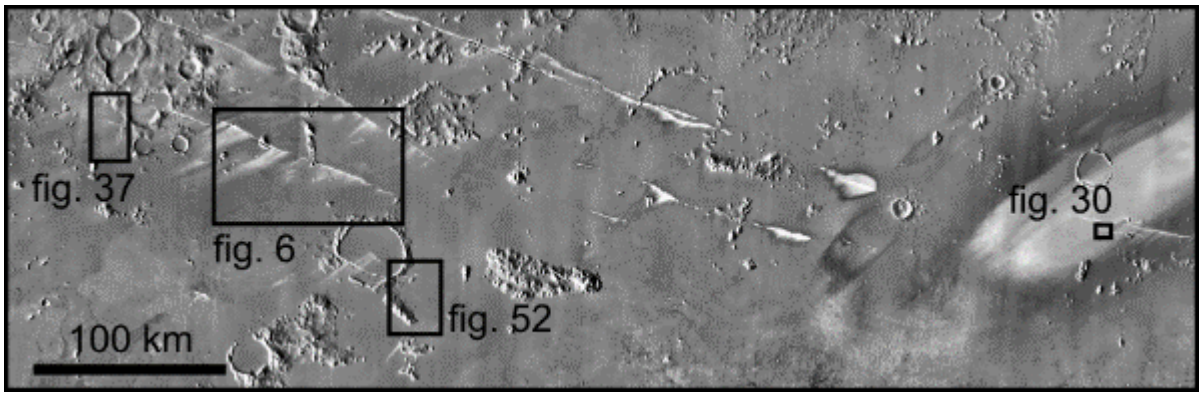

Figure 5. THEMIS IR-day 100 m/pixel image mosaic centered at 7.68° N, 163.99° E showing study site locations. Regional context is provided in Fig. 2.

6.1. Category 1: Fossae flanked by smooth, linear depressions

A series of WNW-ESE oriented, en echelon fossae are exposed near 8.150° N, 160.873° E and comprise a larger fossa that extends ~100 km (Fig. 6). The fossa is characterized by a range of fracture characteristics, surface morphologies adjacent to the fissure, and deposits apparently sourced from the fossa that were then transported away from it toward both the north and south. Two field sites are described in this category (locations are given in Fig. 6), which we refer to as the Bathtub Ring Depression Fossa (BRDF) and the Nested Depression Fossa (NDF), respectively. Descriptions comprise four parts: (1) topographic characterization, (2) geometric characteristics of the fossae and their manifestation at the surface, (3) evidence for modification in close proximity to the fossae, and (4) flow deposits on the flanks of the fossae.

6.1.1. Observations

6.1.1.1. Bathtub Ring Depression Fossa

Extending ~6 km WNW-ESE (from 8.065° N, 161.100° E to 8.0273° N, 161.193° E), the Bathtub Ring Depression Fossa (BRDF) consists of three subparallel fossae (labeled 1, 2, and 3 in Fig. 7; see Fig. 6 for regional context). The gradual albedo variation, both parallel and orthogonal to the fossae, is indicative of relative elevation. The centers of the fossae are deepest and darkest, whereas the western and eastern terminations of the fossae are lighter and shallower. The visible portions of the fossae canyon walls are also lighter in albedo than the bottoms of the fossae, but darker than the albedo of the regional surface dissected by the fossae. MOLA topography and photoclinometry both confirm that the fossae have the greatest depths at their centers, with less relief closer to the segment tips. The minimum elevation within the fossae measured using MOLA data is -2715 m, with neighboring flank elevations around -2682 m, giving a minimum relief of ~33 m.

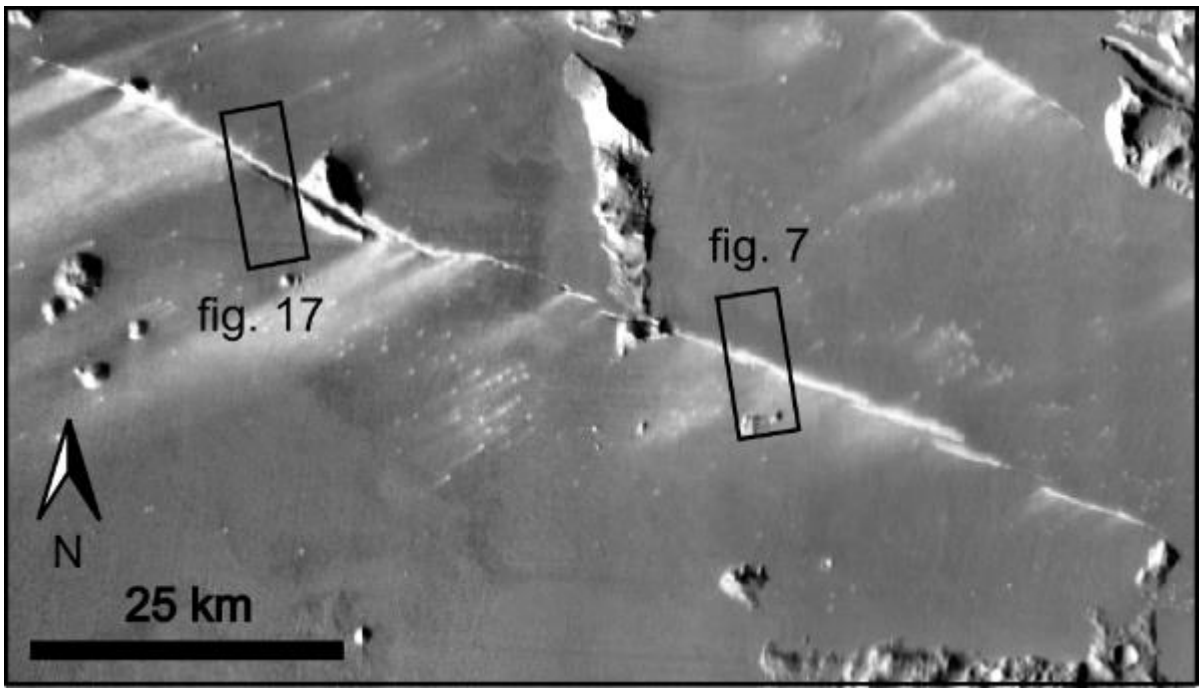

Figure 6. THEMIS-IR day image with 100 m/pixel resolution (centered at 8.150° N, 160.873° E) showing a ~100 km long fossa composed of numerous smaller en echelon fossae. Two field site locations are illustrated: (1) the Bathtub Ring Depression Fossa (BRDF; Fig.7) and (2) the Nested Depression Fossa (NDF; Fig. 17). Details of the surface morphologies adjacent to the fossae are not discernible here.

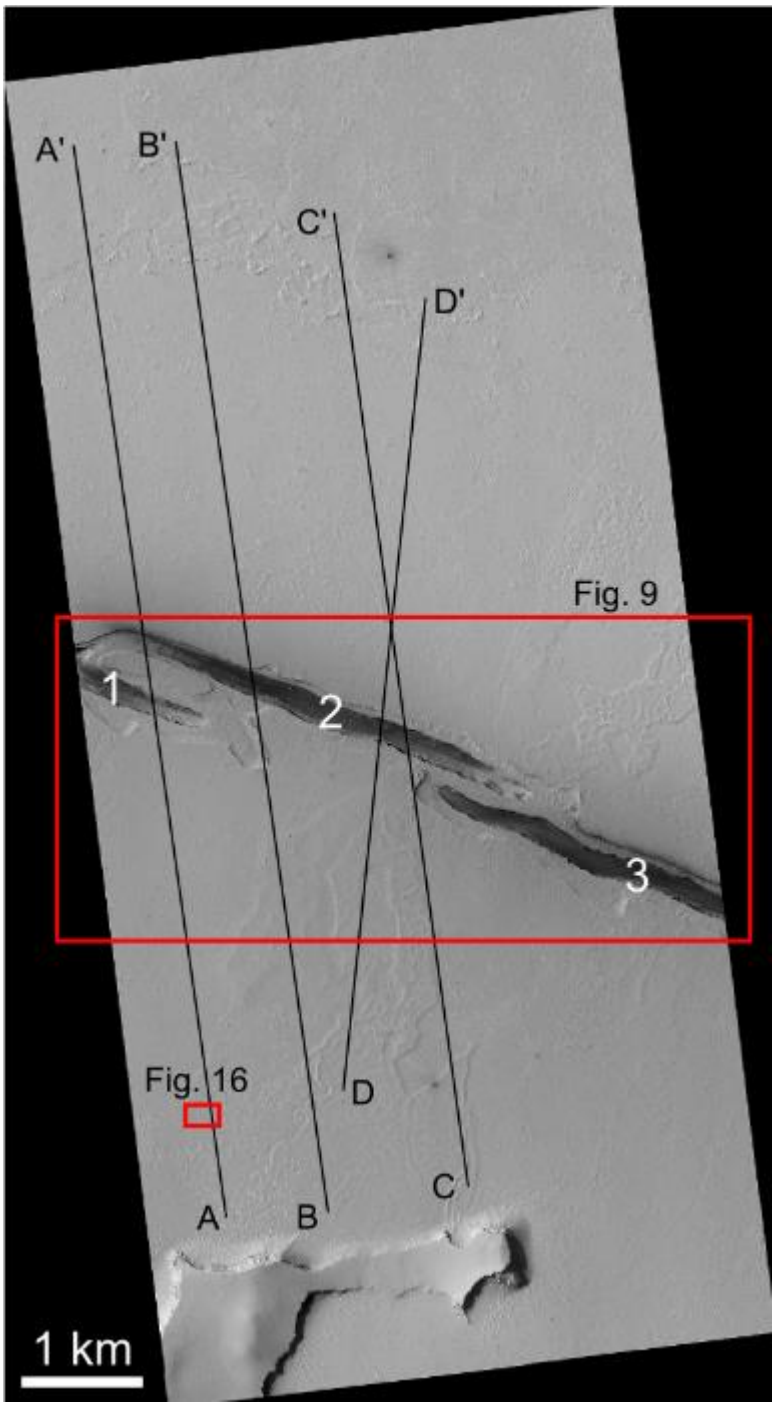

Figure 7. HiRISE observation ESP_036193_1880 (25 cm/pixel, north is up), centered at 8.042° N, 161.150° E. Three en echelon fossae located along the Bathtub Ring Depression Fossa (see Fig. 6 for regional context) have a dark surface albedo within their interior. Each fossa is identified with a number for reference in the text. MOLA profile lines A-A' to D-D' are shown in Fig. 8.

Photoclinometry measurements taken where shadows are pronounced along the edge of fossa 2 (Fig. 7) reveal that the fossa depth decreases towards its western and eastern ends. Topographic profiles drawn nearly perpendicular to the fossa using MOLA data demonstrate there is also a gradual rise of up to 10 meters leading up to the edges of the fossa from both sides (Fig. 8).

The overlapping fossae are closely spaced (100-200 m) and extend beyond the field of view in both the WNW and ESE directions (Fig. 9). This fossa segmentation at a scale of several km, with en echelon or stepping geometries involving subparallel fossae, is characteristic of the geometry of the majority of the Cerberus Fossae fissures. The 3.6 km long fissure (fossa 2 in Fig. 7) at the center of Fig. 9 has a maximum width of ~240 m approximately halfway along its length, decreasing toward the western and eastern terminations.

A characteristic feature preserved at the surface is a flanking depressed area extending the length of the 7 km long portion of the fossa visible in Fig. 9, referred to here as the Bathtub Ring Depression (BRD). The BRD forms a geomorphic halo around each of the three fossae. On average, the depression extends ~200 m perpendicularly away from the fissure walls, with a maximum of 341 m (Fig. 9). Beyond the fossae tips, the depressed surface extends an additional 200-600 m parallel to the fossae trend (Fig. 9). The elevation of the depressed surface is similar everywhere (-2696 m), indicating a relief of ~8 m relative to the adjacent regional surface. The surrounding unit is mapped as a Late Amazonian volcanic unit (lAv) by Tanaka et al. (2014), interpreted as largely unmodified flood lavas and lava channels sourced from fissures and shields.

The interior boundaries of the BRD are defined by the tops of the fissure walls, which appear broadly linear at the scale of 100s of m (Fig. 9), but which consist of an en echelon array of left-stepping fractures at the scale of 10s of m (Fig. 10). The fracture spacing along this en echelon array is on the order of 13 m (the perpendicular distance between two

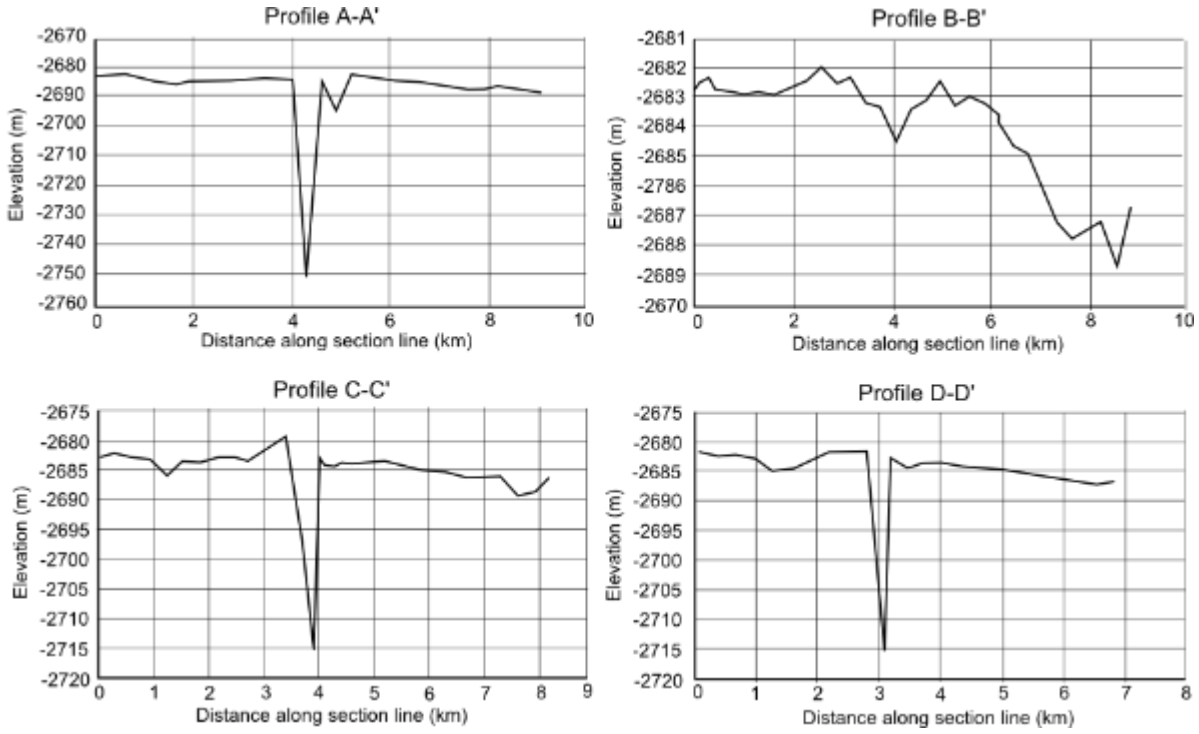

Figure 8. Topographic profiles generated from MOLA PEDR point data along profile lines in Fig. 7. Profile lines and corresponding MOLA orbits are as follows: A-A' (orbit: 17256), B-B' (orbit: 11232), C-C' (orbit: 10641), and D-D' (orbit: 17287). In each profile, a depression occurs where the cross section line intersects the fossa. On both sides of the fossa, a gradual rise in topography of up to 10 m occurs toward the near-vertical cliff face that comprises the fossa edge.

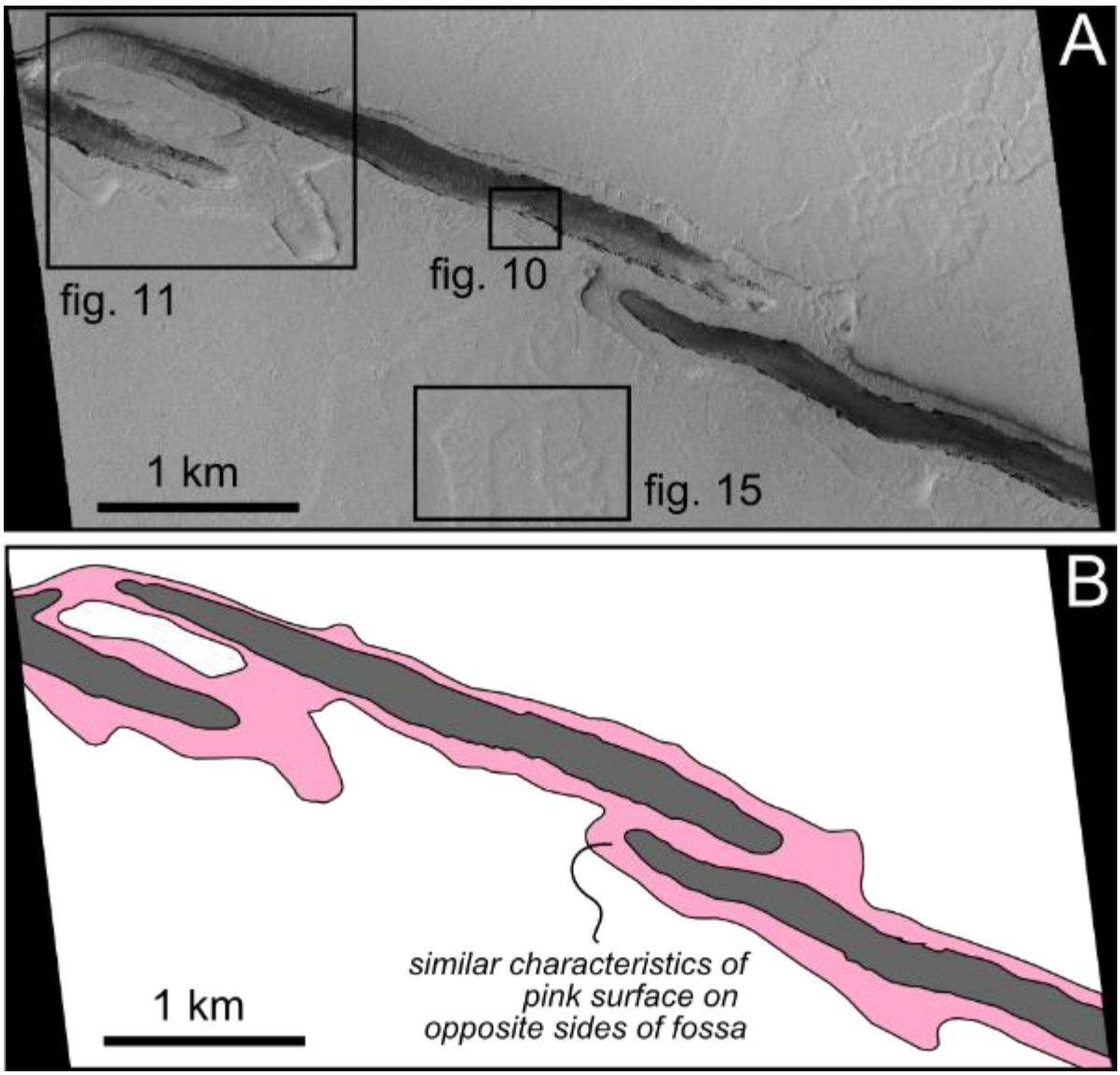

Figure 9. (A) HiRISE observation ESP_036193_1880 (25 cm/pixel; north is up) (sub-region from Fig. 7) showing a depressed geomorphic halo around each of the three fossae, referred to as the Bathtub Ring Depression (BRD). Boxes show locations of Figs. 10, 11, and 15. (B) Simplified geological map of (A). Each fossa (dark grey) crosscuts its adjacent BRD (pink). The white surrounding unit is presumably of volcanic lithology (mapped as lAv by Tanaka et al., 2014).

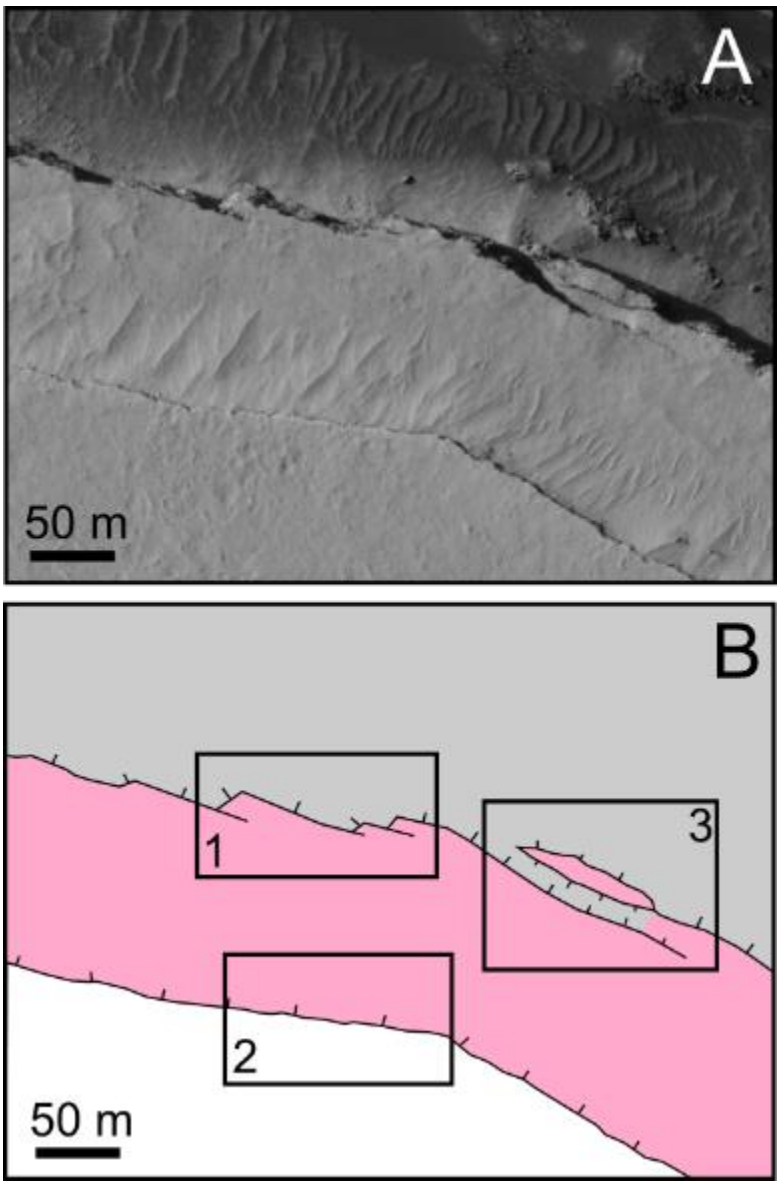

Figure 10. (A) Close-up of HiRISE observation ESP_036193_1880 (25 cm/pixel; north is up), showing the morphology of the fossa edge and the varying boundary types of the Bathtub Ring Depression (BRD) adjacent to the fossa. (B) Simplified geologic map. The small ticks are oriented in the direction of dip of the BRD boundaries. The white area represents the regional surface that the fossa dissects, pink is the depressed halo (BRD) around the fossa, and light grey is the deeper area interior to the fissure wall. Three areas highlighted by numbered black boxes are referred to in the main text.

parallel fractures in box 1 in Fig. 10). In one location, a sloping ramp appears to physically connect the BRD with the fissure floor (box 3 in Fig. 10), isolating an adjacent pinnacle along the fissure wall (69 m long by 13 m wide pink polygon within box 3 in Fig. 10). Mass wasting along the steep fissure walls is evidenced by the presence of 5-10 m diameter boulders that line the fissure walls along the fissure floor (Fig. 10). The fissure bottom is also mantled by fine grained sediments that comprise transverse dune forms caused by wind currents through the fissure canyon (as is characteristic in most of the Cerberus Fossae).

Box 2 in Fig. 10 shows the escarpment along the perimeter of the topographically subdued surface (BRD) adjacent to the fossa. Although there exists a small amount of irregularity or roughness to the boundary at the meter scale, the outer boundary of the BRD is relatively continuous and lacks the stepping fracture morphology that characterizes the fossa edges (box 1 in Fig. 10). The outer boundary of the BRD nonetheless mimics the shape of the fossae, with localized protrusions away from this trend (Figs. 9 and 11)

The bathtub ring depression (BRD) is mostly mantled by dust, masking the textures of its underlying upper surface. Nonetheless, some geomorphic characteristics are preserved on relative topographic rises within the BRD (Fig. 11). Since dust typically occupies lower lying areas, any higher standing surface devoid of dust permits an analysis of the surface textures within the BRD. One such feature is a ~250 m wide domal rise adjacent to the fossa edge (Fig. 12). Wind blown dunes outline the periphery of the domal rise (arrows in Fig. 12).

The domal rise is crosscut by the edge of a fossa, indicating that the domal rise exists on a surface that pre-dates the fossa. Due to a lack of shadows or MOLA tracks across the feature, the relative elevation of the domal rise above the topographically subdued BRD surface is not known. Polygonal shapes (~12 m across) can be discerned on the surface of the domal rise (Fig. 12), with high albedo interior surfaces and dark albedo inter-polygon regions, indicating that the polygons are raised at their centers and have relative lows between them (Fig. 12). In the region where the BRD haloes around fossae 1 and 2 in Fig. 7

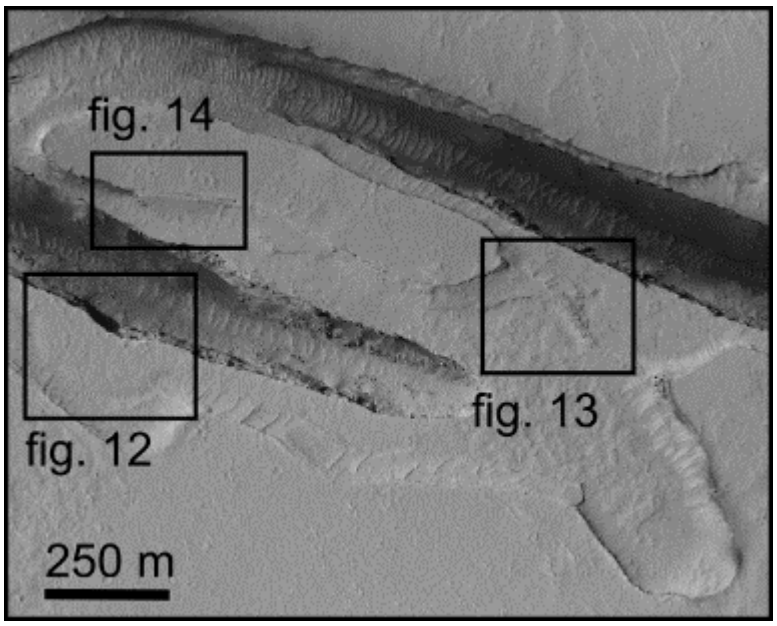

Figure 11. Close-up of HiRISE observation ESP_036193_1880 (25 cm/pixel; north is up) showing segment morphology relative to the Bathtub Ring Depression (BRD) surface. Boxes show locations of Figs. 12-14. The BRD forms a geomorphic halo around each fossa. Adjacent fossa haloes may be physically connected where the fossae overlap along strike (e.g., Fig. 13). The shallowing of the fossae bottoms toward the fossae tips is particularly evident here.

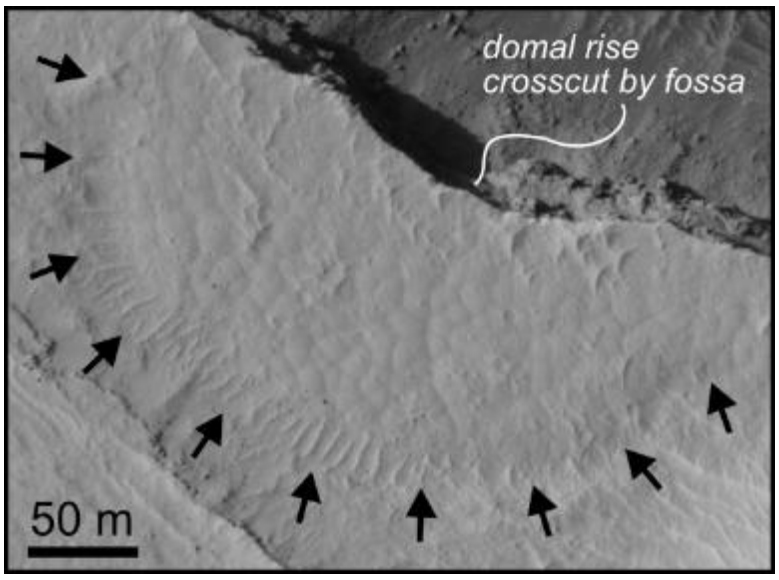

Figure 12. Close-up of HiRISE observation ESP_036193_1880 (25 cm/pixel; north is up), showing a topographic rise outlined by dunes and highlighted by arrows (see Fig. 11 for context). Note the lack of dunes on the surface of the domical rise. The lack of dust accumulation on the surface implies a relative high. Polygonal features on the surface of the domical rise form an interconnected network with narrow, dark-albedo troughs that separate the high-albedo polygon interiors.

are connected, the BRD surface is again exposed (Fig. 13). A prominent ridge (black arrows in Fig. 13) separates adjacent smoother surfaces (s1 and s2) with a polygonal texture similar to that expressed on the domal rise in Fig. 12.

The escarpment that defines the outer topographic boundary of the bathtub ring depression (BRD) forms an abrupt elevation change from the surrounding regional surface (Fig. 14). Although this escarpment differs from the fracture-bound edges of the fossae themselves (cf. Fig. 10), the exterior boundary of the BRD does exhibit morphologic variability. For example, the northern edge of the depressed surface adjacent to fossa 1 in Fig. 7 has a jagged outline with <10 m of vertical relief (calculated using photoclinometric methods; Fig. 14). Where the boundary is highlighted by white arrows in Fig. 14, there is an abrupt vertical scarp with a dark surface deposit along its base. In contrast, where the boundary is annotated with black arrows, a ~50-m-wide sloping surface defines the edge of the BRD and appears to have detached from the adjacent regional surface along a large crack that is up to ~15 m wide.

Fossae-adjacent deposits outside of the depressed BRD surface have distinctive morphologies that provide clues to their origin. For example, at a distance of 1 km from the BRD, a flow-like deposit extends south of the fossae (Fig. 15; see Fig. 9 for context and additional examples that extend northward from the fossae). Black arrows outline the periphery of a flow surface with two parallel lobes that extend across the field of view. The lobes have a hummocky surface, including elongate depressions oriented transverse to the flow edges (white arrows in Fig. 15).

A lobate flow unit 6 km south of the BRD appears to have been sourced from the fissures and exhibits similar surface characteristics to the BRD surface, such as polygons with raised centers and depressed edges (Fig. 16). The polygons are 5-10 m across, with an average of about 7 m, and resemble those on the domal rise in Fig. 12, suggesting this surface texture is characteristic of the surface processes in the region.

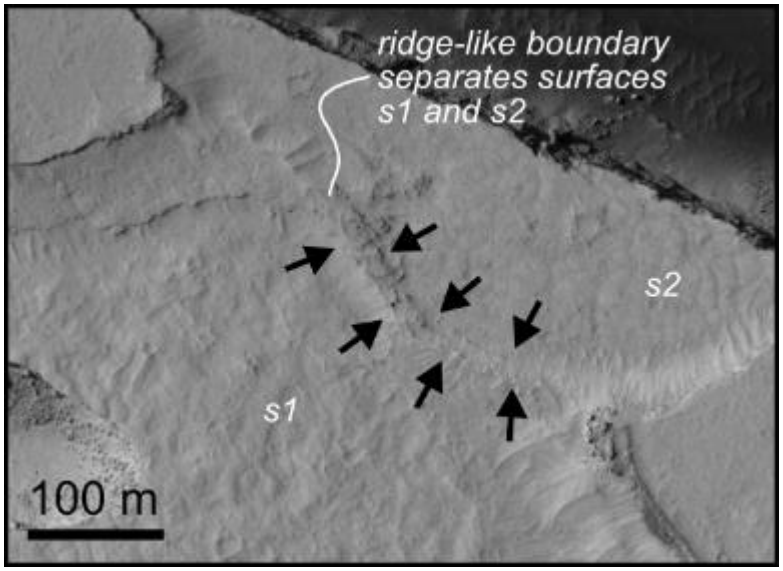

Figure 13. Close-up of HiRISE observation ESP_036193_1880 (25 cm/pixel; north is up), showing a ridge that separates two surfaces, s1 and s2, that appear to be at similar elevations (see Fig. 11 for context). A polygonal texture is evident on the BRD surface, best expressed to the north of the ridge, similar to the surface texture evident on the domal rise in Fig. 12.

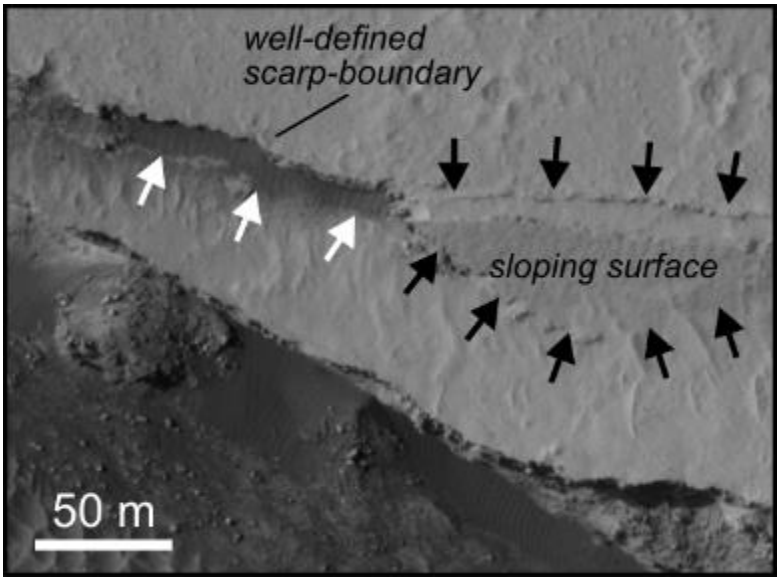

Figure 14. Close-up of HiRISE observation ESP_036193_1880 (25 cm/pixel; north is up) showing two contrasting styles of the Bathtub Ring Depression (BRD) outer boundary (see Fig. 11 for context). White arrows point to a jagged, abrupt escarpment that transitions to a ~15 m wide fissure, indicated by black arrows. Note the accumulation of narrow bands of dust at the base of the escarpments indicated by the white arrows. The location of this dust accumulation implies a different topographic level immediately adjacent to the fissure wall.

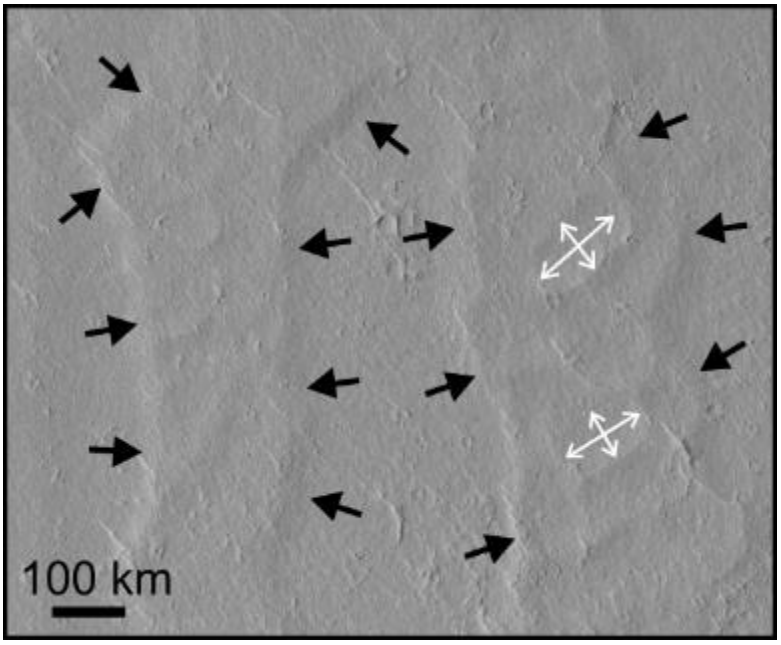

Figure 15. Close-up of HiRISE observation ESP_036193_1880 (25 cm/pixel; north is up; see Fig. 9 for context). Black arrows outline the edges of a lobate unit that extends south from the BRDF fissures. The flow surface is characterized by hummocks and bowl-shaped depressions, indicated by white arrows.

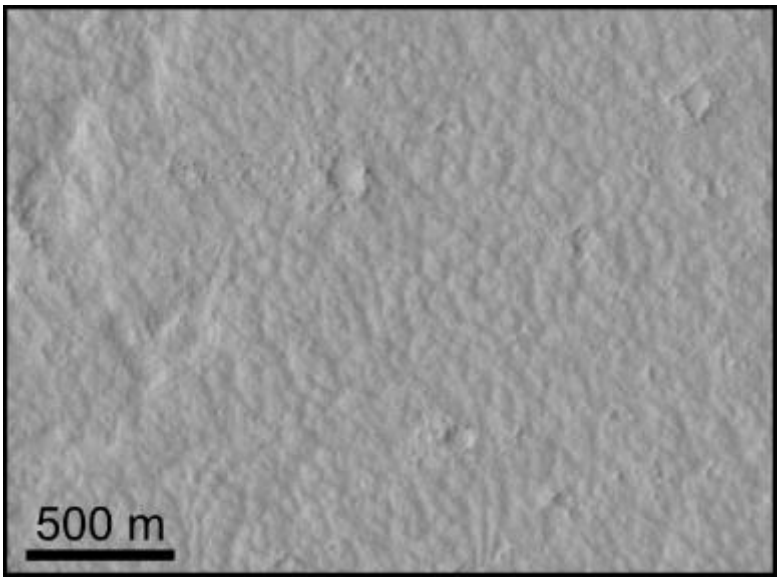

Figure 16. Close-up of HiRISE observation ESP_036193_1880 (25 cm/pixel; north is up; see Fig. 7 for context). This geological unit has a polygonal surface texture that is characteristic of the region. The polygons are similar to those on the domal rise in Fig. 11, but smaller in scale.

6.1.1.2. Nested Depression Fossa

The fossa in Fig. 17 extends 6.6 km across the field of view from 8.35° N, 160.40° E to 8.290° N, 160.495° E. Four texturally and topographically distinct surfaces characterize this fossa, identified using letter descriptors P, Q, R, and S (Fig. 17). Fossa-adjacent surfaces P and Q are texturally smooth relative to surfaces S and R, which exhibit many mounds, ridges, and impact craters that, together, create a more topographically rough surface. The topographic profile A-A' shows the variation in topographic expression across the four surfaces P, Q, R, and S (Fig. 18). A gradual elevation gain of ~5 m occurs from the start of the section line toward the fossa, which is encountered at ~7.5 km along A–A'. A shallow depression, up to 8 m deep, encircles the fossa, extending outward to between 1-1.5 km north and south of the fossa walls (evident between 6 and 10 km along A-A'; Fig. 18), and incorporates surfaces P and Q. Surface P corresponds to the gentle slope inward toward the fossa between ~8 and 10 km along A-A' (Fig. 18). South of the fossa, the gentle slope corresponds to surface Q, which extends along the length of the fissure as well as along an adjacent elongate, linear depression that runs parallel to the fossa, ~800 m south of the fossa rim (Figs. 17 and 19). Surface S is confined to a low region that sits ~10 m lower than the topographic high that separates it from surface P (Fig. 18). Although the fossa is shown by the MOLA profile to be only 33 meters deep (achieving a minimum elevation of -2693 m relative to the MOLA datum; Fig. 18), photoclinometry performed on the HiRISE image in Fig. 19 indicates a fossa depth of at least 500 m.

The fossa forms a continuous trough along strike, as shown in Fig. 19; however, its geometry is not perfectly linear, but exhibits several steps or bends that reflect a higher-order segmentation (e.g., a prominent right step at the center of Fig. 19A). Similar to the projections of the bathtub ring depression surfaces beyond the fossae tips in Fig. 9, depressed surface Q in Fig. 19 continues beyond the tips of the fracture segments that define the edges of the central fossa, forming westward-pointing protrusions on the southern

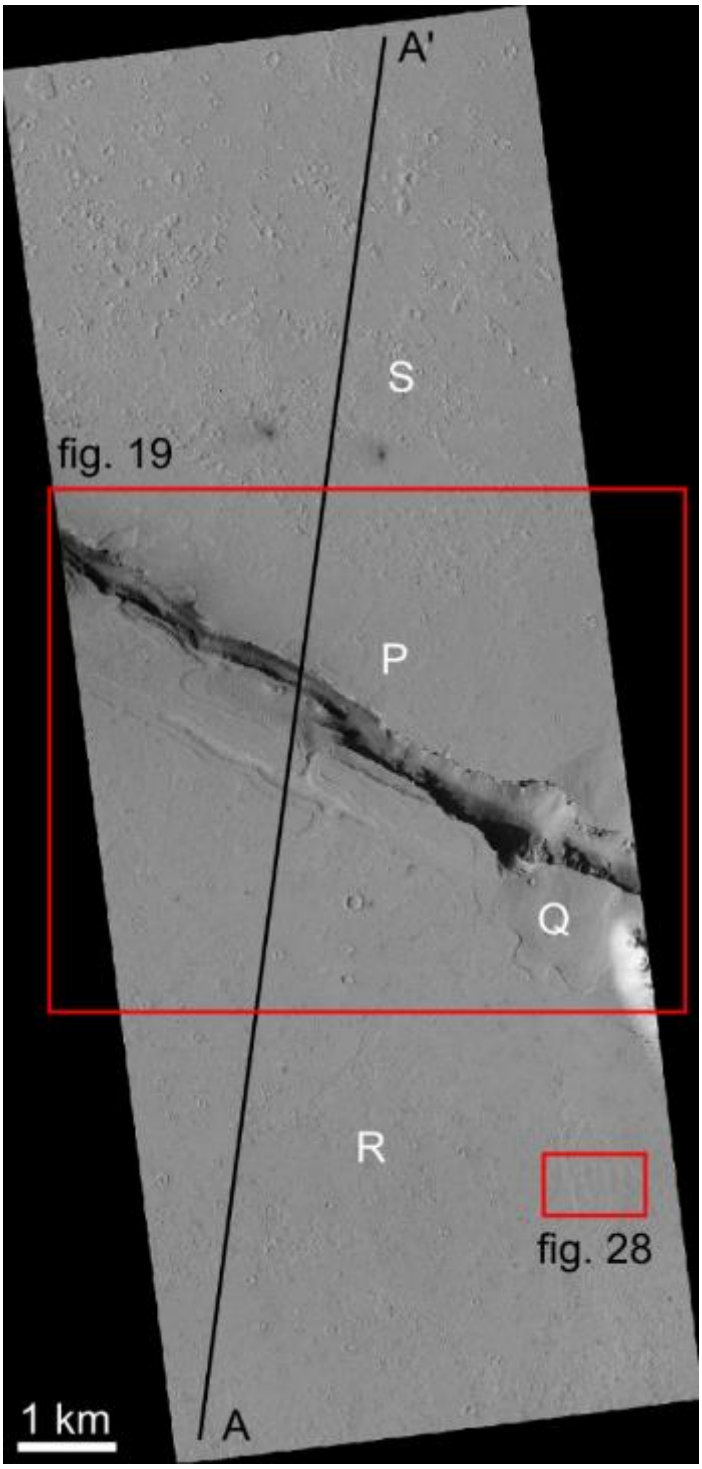

Figure 17. HiRISE observation ESP_037327_1885 (25 cm/pixel; north is up), centered at 8.309° N, 160.443° E. Immediately adjacent to the NW-SE trending fossa is a texturally muted and topographically subdued surface referred to here as the Nested Depressions (surface Q). The topographic profile along line A-A' is shown in Fig. 18. See main text for detailed descriptions of surfaces P, Q, R, and S.

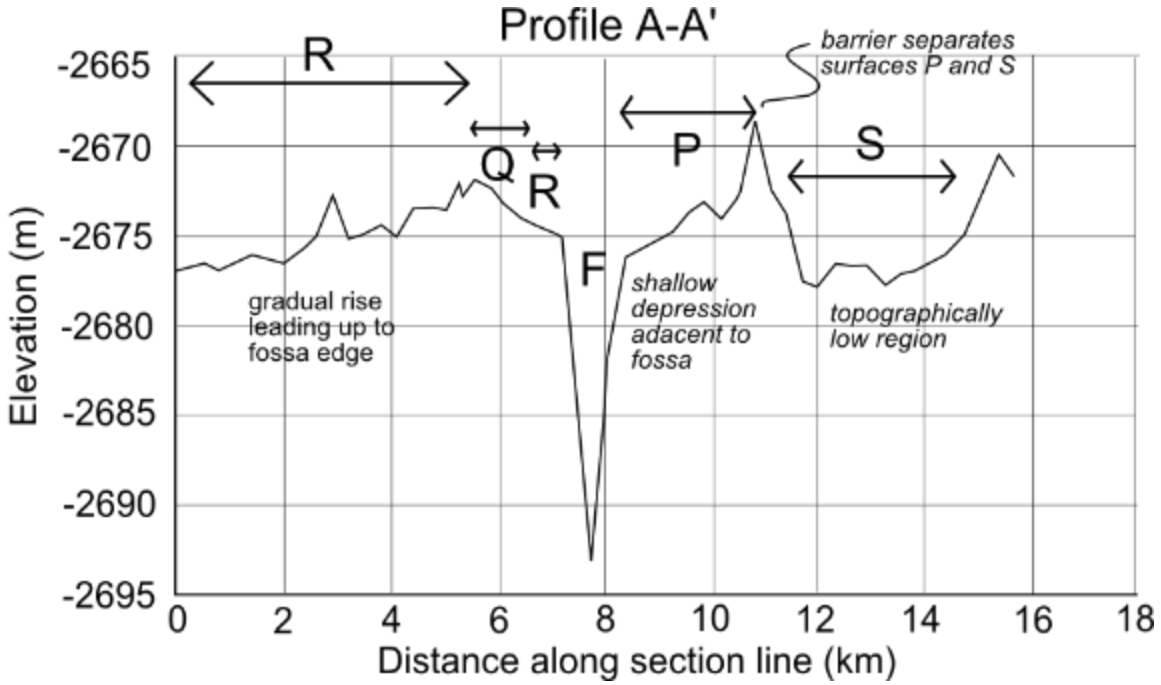

Figure 18. MOLA PEDR derived elevation data (orbit 11175) along profile A-A' (see Fig. 17 for context). Surfaces P, Q, R, and S, as well as fissure F, are shown in map view in Figs. 17 and 19.

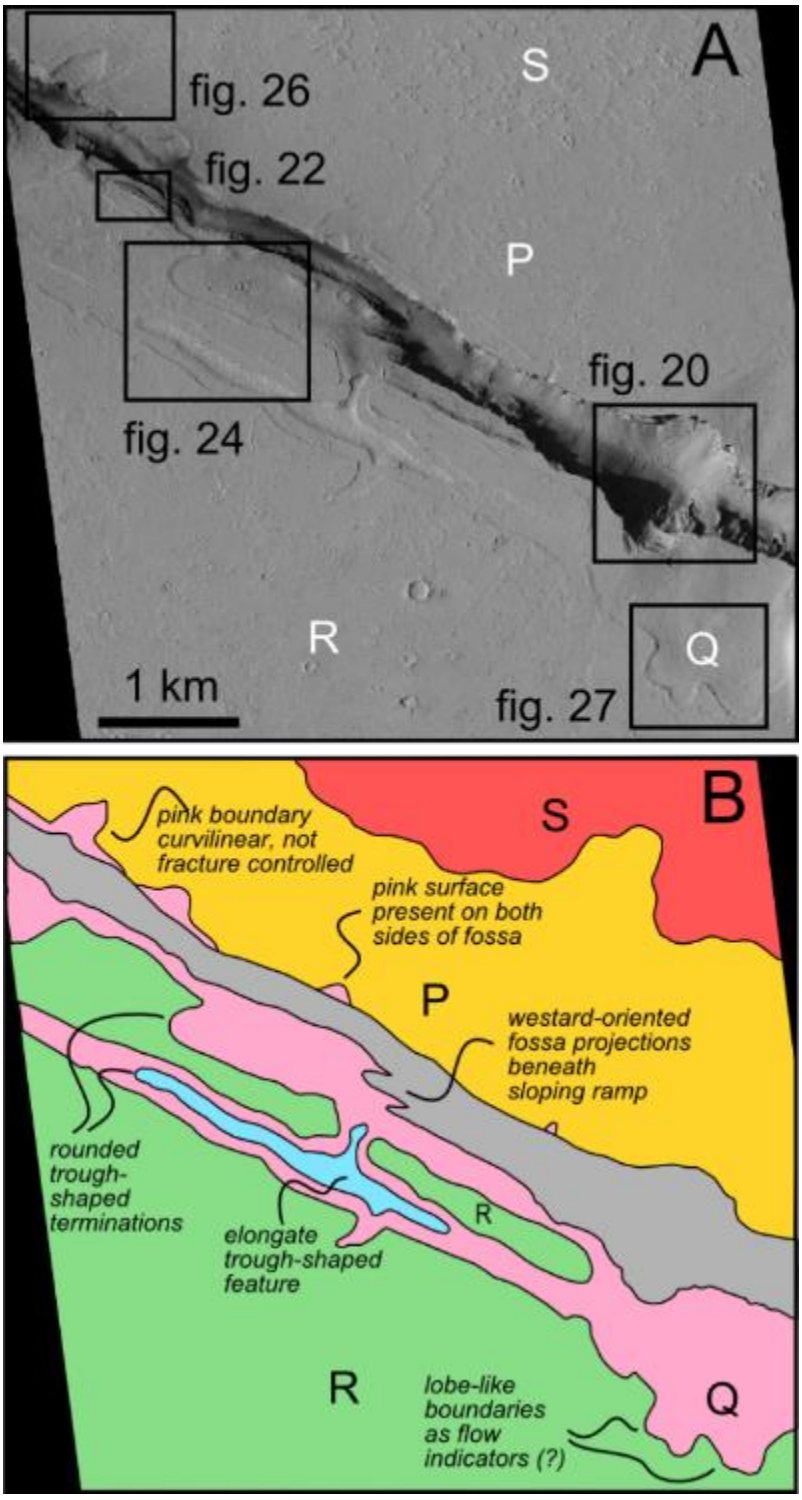

Figure 19. (A) HiRISE observation ESP_037327_1885 (25 cm/pixel; north is up) showing the Nested Depression Fossa. (B) Simplified geological map, with the nested depression in pink, and an elongate trough-like feature in blue. Boxes show image locations, and letters P (yellow), Q (pink), R (green), and S (red) correspond to the description of morphology and shown in Figures 17 and 18.

margin of the fossa (pink unit in Fig. 19B). The linear depression that runs parallel to the fossa ~800 m to its south also forms a westward protrusion of surface Q, but is not visibly associated with a fossa anywhere along its strike. This depression contains a second, lower linear depression nested within it (blue unit in Fig. 19), similar to the manner in which surface Q encompasses the fossa itself. This morphology provides the inspiration for the name used to describe the fossa in Figs. 17 and 19 as the Nested Depression Fossa (NDF).

Although the NDF is generally <500 m wide, it attains a local width of ~1 km at a bowl-shaped depression that protrudes outward from the fossa walls (Figs. 20 and 21). Collapse along resistant layers produced a near-vertical escarpment near the top of the south-facing fossa walls within the bowl-shaped depression (white arrows in Fig. 20). In contrast, the north-facing fossa wall is interrupted by a ~300-m-wide, semi-circular scalloped depression (black arrows in Fig. 20) that slopes toward the fossa floor in a series of steps created by rotated blocks, each with its own headwall scarp. These features emphasize the importance of slumping and other mass wasting in modifying the fossa margins. Angular boulders that collected at the bottom of the interior talus slopes within the fossa, approximately half-way between the north- and south-facing fossa walls, range in diameter from 3-15 m (Fig. 21).

Near the northwestern end of the Nested Depression Fossa in Fig. 19, the fossa wall is not a single vertical cliff that descends abruptly from surface Q to the fossa floor, but rather exhibits a series of step-wise transitions from higher to lower elevations that occurs as at least seven vertical steps (arrows in Fig. 22). Each step forms a terrace that appears to be resistant to erosion and resembles the stepwise descent into the canyons eroded into the multiple lava flows of the Columbia River flood basalts in the northwestern United States (e.g., Reidel, 1998) and the Deccan Traps in India (e.g., Jerram and Widdowson, 2005). Similar to Fig. 20, boulders appear sourced from the scarps and have accumulated on the fossa floor (Fig. 22). Most of the terraces exhibit near-vertical escarpments, although some

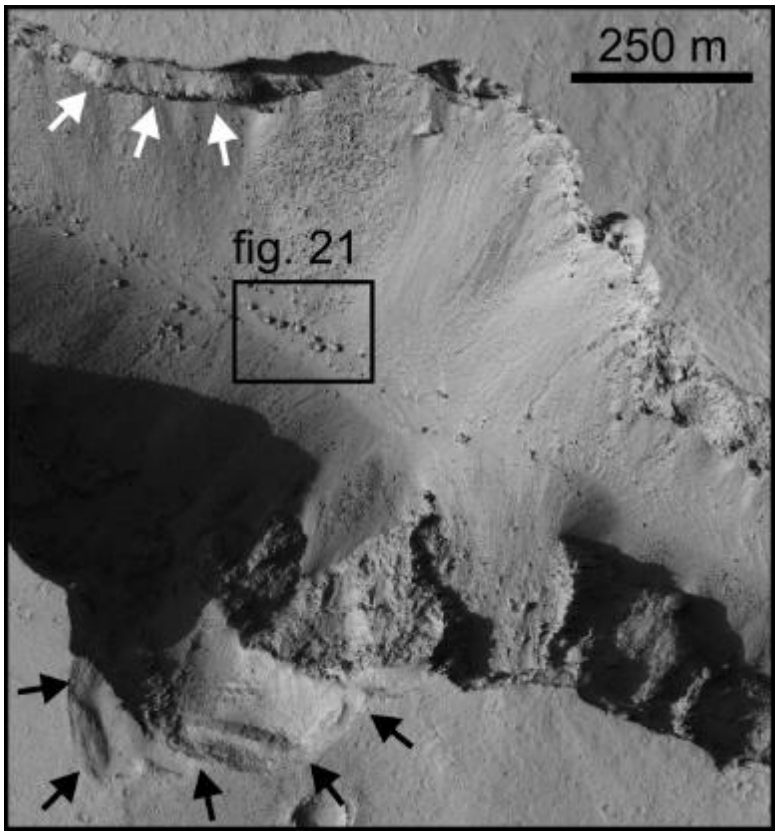

Figure 20. HiRISE observation ESP_037327_1885 (25 cm/pixel; north is up; see Fig. 19 for context) showing a bowl-shaped area in the Nested Depression Fossa widening through mass wasting. A resistant layer near the surface (white arrows) creates vertical walls along the fossa edge. Mass wasting from the fossa walls has resulted in boulder accumulations on the fossa floor (Fig. 21), as well as a slump-like wall collapse indicated by black arrows.

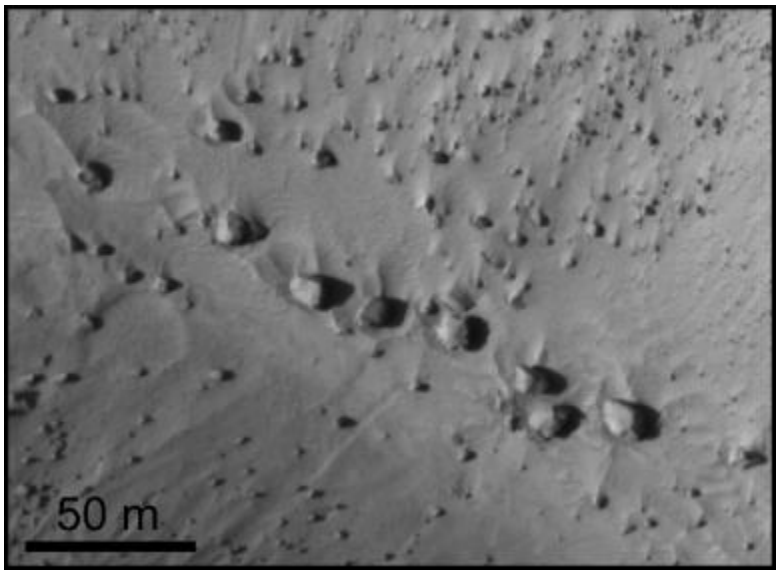

Figure 21. HiRISE observation ESP_037327_1885 (25 cm/pixel; north is up; see Fig. 20 for context) showing boulders on the fossa floor with maximum diameters of ~15 m.

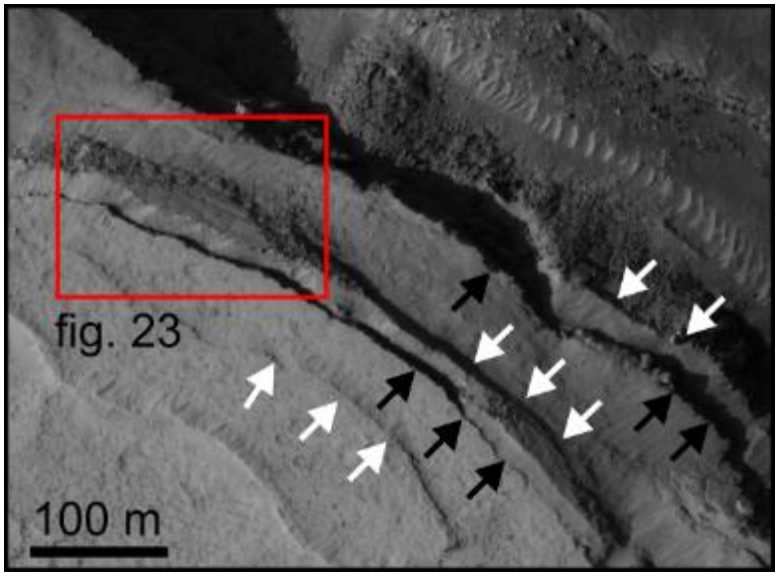

Figure 22. HiRISE observation ESP_037327_1885 (25 cm/pixel; north is up; see Fig. 19 for context), showing a stair-step edge along the Nested Depression Fossa, comprising at least seven terraces and escarpments. Arrows indicate the boundaries of terraces that step progressively lower in elevation toward the fossa floor. Location of Fig. 23 shown by red box, indicating a sloping surface that connects two terrace levels.

sloping surfaces are also evident (Figs. 22 and 23). For example, an approximately 207 m long by 28 m wide surface is indicated with arrows in Fig. 23 and shows the extent of a slab of material that is tilted down toward the fossa interior, forming a ramp between two terraces with different elevations. White arrows indicate a continuous fracture that defines the upper extent of the slab where it slopes abruptly away from the upper terrace (Fig. 23). Black arrows at the base of the slab highlight a more irregular but still somewhat linear lower boundary. The upper surface of the sloping slab shows an interconnected network of ~15 m wide, four- to six-sided polygons that appear to have raised centers.

Sloping surfaces are found elsewhere along the Nested Depression Fossa (NDF), but differ from the inclined slab shown in Fig. 23. For example, Fig. 24 shows the rounded terminations of two elongate, trough-like depressions located south of the NDF's southern edge. These depressions are defined by the blue and pink units in Fig. 19. A subtle sloping surface descends from near the outer boundary of the pink unit toward the fossa edge (box 1 in Fig. 24). At least three topographic surfaces (s1, s2, and s3) are defined by nested troughs within the second elongate depression in Fig. 25. Surface s2 sits lower than regional surface s1, and encloses a lower, central trough (surface s3) that is mantled by dust and transverse dune forms. The boundary between surfaces s2 and s3 differs in character between the northern and southern boundaries of the central s3 trough. The southern trough margin is defined by a convex-upward, monoclinal surface that descends from the pink (s2) to the lower blue (s3) unit in Figs. 19 and 25 and is characterized by a series of parallel and overlapping fractures that are discontinuous, with maximum lengths of up to 300 m and maximum apertures of ~5 m (box 1 in Fig. 25). In contrast, the northern trough margin is defined by a single, 10 m wide fracture that is continuous along the length of the trough margin over a distance of 600 m (white arrows in Fig. 25). In contrast to the fractured margins of the s3 trough, the edges of the pink (s2) depression are gently curved in map

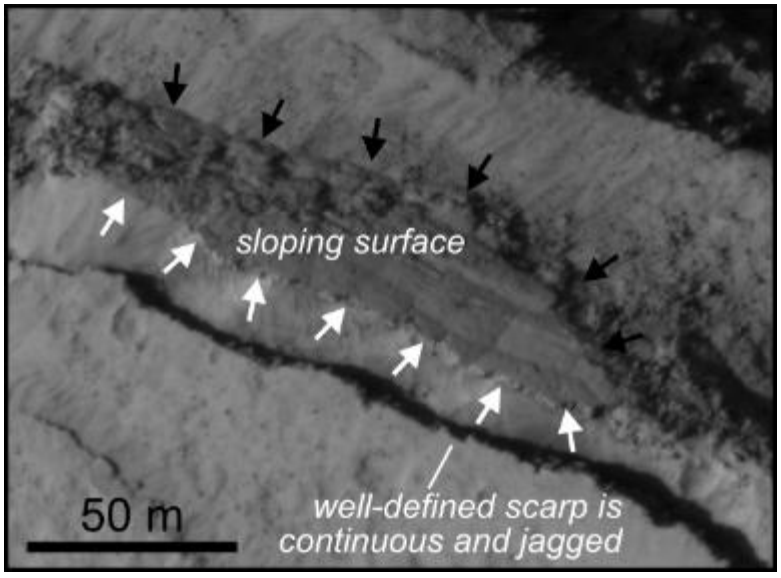

Figure 23. HiRISE observation ESP_037327_1885 (25 cm/pixel; north is up; see Fig. 22 for context). A sloping surface connects two terraces with different elevations. The upper termination of the sloping surface (white arrows) is linear and continuous, whereas the lower termination is irregular and blocky (black arrows). The sloping surface is free of fine dust cover and shows four- to six-sided, raised polygons on the surface.

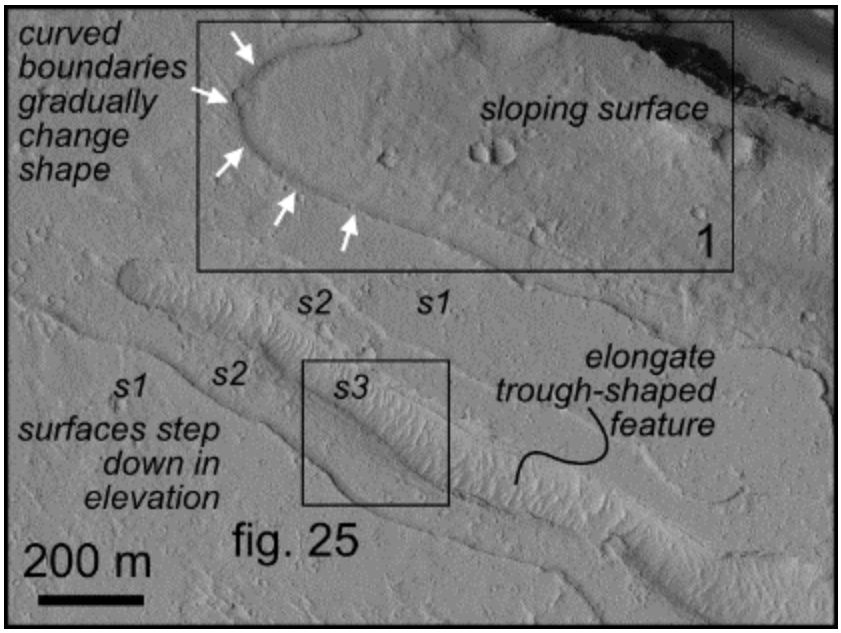

Figure 24. HiRISE observation ESP_037327_1885 (25 cm/pixel; north is up, see Fig. 19 for context), showing elongate, depressed surfaces south of the Nested Depression Fossa (NDF). One surface slopes toward the fossa edge (box 1) away from an arcuate outer boundary, indicated by white arrows, between the depressed surface and the regional surface (s1). A second, elongate trough located ~800 m south of the NDF southern edge comprises surface s2 (pink unit in Fig. 19) that encloses an even lower central trough (a nested depression) defined by surface s3 (blue unit in Fig. 19). The boundary between surfaces s2 and s3 includes a curved, sloping surface (black box labeled Fig. 25).

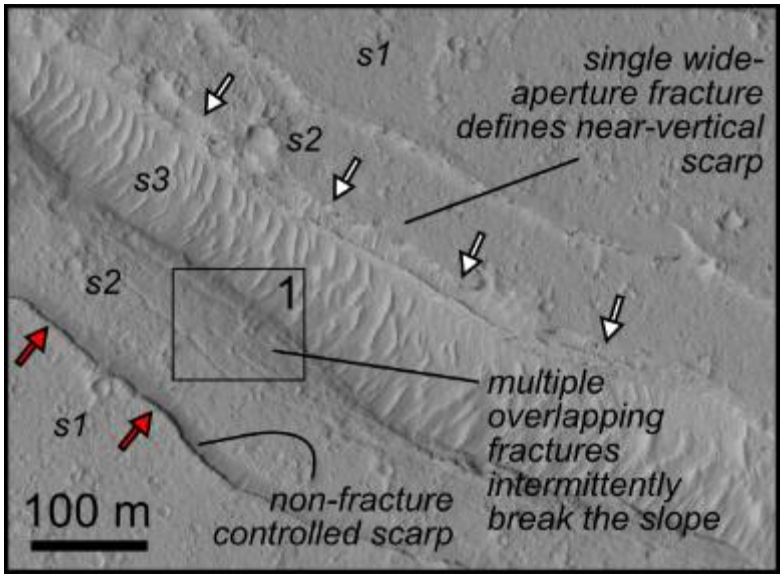

Figure 25. HiRISE observation ESP_037327_1885 (25 cm/pixel; north is up; see Fig. 24 for context). A NW-SE oriented, elongate depression (where surface s2 sits lower than regional surface s1) forms a nested depression that contains a central trough (surface s3) that is mantled in dust and sculptured into transverse dune forms. A curved, sloping surface between s2 and s3 (box 1) is dissected by discontinuous (up to 300 m long), narrow (~5 m wide), overlapping fractures. The northern edge of the central s3 trough is defined by a continuous (600 m long), ~20 m wide fracture indicated by white arrows. This fracture exhibits a left step toward its southeastern end (between the two right most white arrows). Red arrows identify an abrupt scarp between upper surface s1 and depressed surface s2.

view and define a vertical escarpment that is not obviously fracture controlled (red arrows in Fig. 25).

Topographically subdued surfaces that are orthogonal to the strike of the fossa walls (Fig. 26) demonstrate multiple levels/terraces that step down toward the fossa interior. This topographically depressed surface has a subtle, somewhat discontinuous boundary (between s1 and s2 in Fig. 26) that is curvilinear. This boundary fades with distance away from the fossa, as the surface s2 gradually merges with surface s1 at the most distal part of the depressed protrusion, with no clear boundary between them. Due to the lack of pronounced shadows, photoclinometry is not a useful tool to determine the relative elevations of s1, s2, and s3. A lower depressed surface (s3) is contained within s2 and extends ~400 m away from the fossa with a width of ~188 m. Where this lower surface intersects the fossa wall, an amphitheater shaped erosional scarp edge has developed, similar to the bowl-shaped collapse feature in Fig. 20.

The boundary between depressed surface Q (pink unit in Fig. 19) and the regional surface R is shown again in more detail in Fig. 27 and shows many similarities to the curvilinear boundary between s1 and s2 in Fig. 26. The boundary of the s2 surface is curvilinear to locally arcuate, varying along its length from near-vertical escarpments (black arrows) to gradual sloping surfaces (Fig. 27). In one location, the s2 boundary is defined by a curvilinear ridge with a 10 m wide arcuate fracture at its apex (white arrows in Fig. 27). The inset image in Fig. 27 shows that the curvilinear ridge transitions into a ramp that appears to slope upwards from surface s2 to s1. The upper surface of s2 is relatively smooth, with broad undulations that are 300-400 m wide.

Farther away from the NDF, downslope from the southern boundary of the s2 surface in Fig. 27, the surface geomorphology is defined by flow units that appear to be emplaced as constructional deposits (Figs. 17 and 28). Six approximately north-south oriented lobes exhibit smooth surface textures and fairly consistent widths (~100 m).

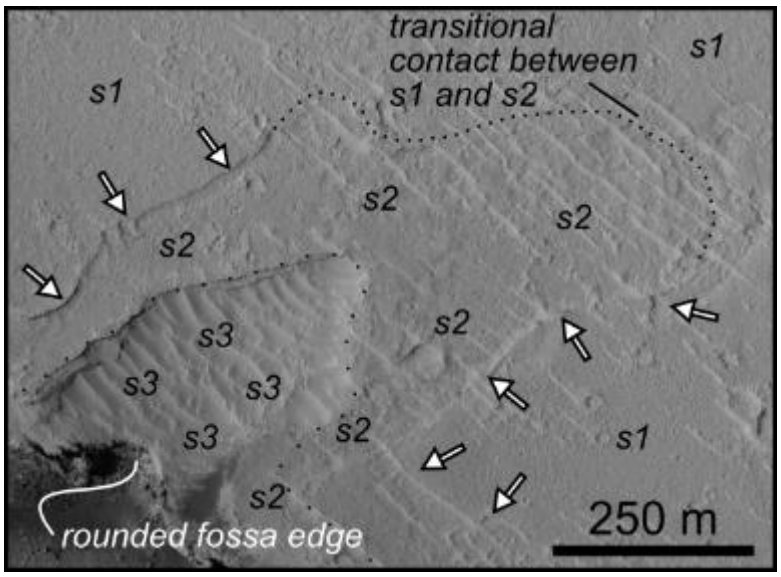

Figure 26. HiRISE observation ESP_037327_1885 (25 cm/pixel; north is up; see Fig. 19 for context), showing protrusions oriented orthogonally to the fossa walls that exhibit multiple levels and step progressively lower into the fossa. Dune forms within the lower depression (s3) confirm its subdued elevation relative to surfaces s2 and s1. The boundary between s1 and s2 is distinct closer to the fossa edge (white arrows) but is subtler further away (dotted line).

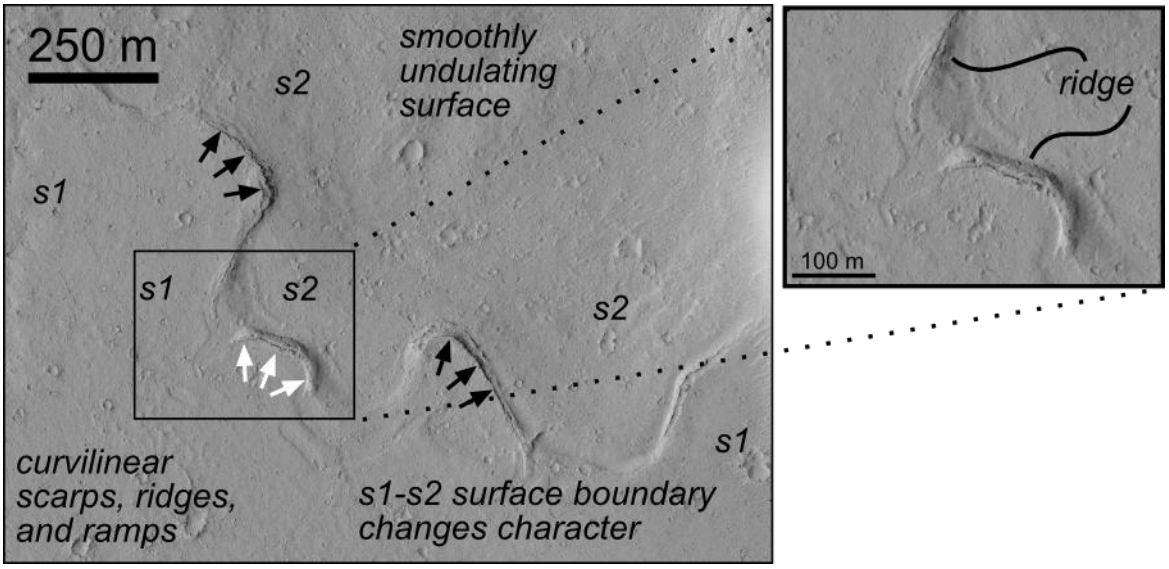

Figure 27. HiRISE observation ESP_037327_1885 (25 cm/pixel; north is up; see Fig. 19 for context). Curvilinear scarps (black arrows) define portions of the boundary between surface s2 (pink unit in Figure 19) and s1; elsewhere, the boundary is gently sloping. In one location, the boundary is defined by a narrow ridge (white arrows and inset image) with a fracture along its crest.

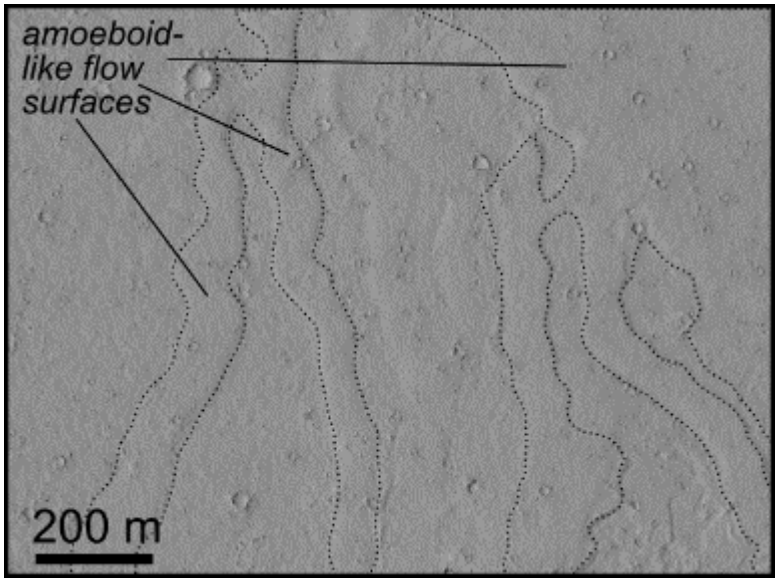

Figure 28. HiRISE observation ESP_037327_1885 (25 cm/pixel; north is up; see Fig. 17 for context), showing amoeboid flows that have a long axis oriented parallel to the downslope direction (~N-S; see Fig. 18 for topographic profile), away from the fossa. The width of each flow is on average 100 m.

The regional topography (Fig. 18) indicates that these lobes may have flowed downslope away from the NDF, and define part of the regional surface R or s1 in Figs. 17, 19, 24, 25, 26, and 27.

6.1.2. Interpretations

The Bathtub Ring Depression (BRD; Fig. 7) and Nested Depression (NDF; Fig. 17) fossae exhibit similar morphological attributes that may indicate a common formation mechanism. Both sites contain a fossa that crosscuts a smooth, depressed surface that is topographically flat. The perimeter of each depressed surface mimics the shape of the edges of the central fossa that it encompasses at a distance of several hundreds of meters to more than a kilometer from the fossa edge. This perimeter is manifested variably as near vertical scarps with a jagged outline (Figs. 11, 13, 24, 25, 26, and 27), a gently sloping transition (Figs. 26 and 27), a dipping slab (Fig. 14 and 23), or a linear ridge (Figs. 13 and 27).

The observation that the depressed surfaces that surround both the BRDF and the NDF are crosscut by the fossae themselves implies that the fossae formed after the development of the depressed surfaces. At both the BRDF and the NDF, the depression edges mimic the edges of the enclosed fossae (Figs. 9 and 19). These depressions appear as elongate troughs with smooth edges and rounded ends that define a “bowl” shape and their formation is likely related to underlying magmatic dikes, as described below. This likely explains why the edges of the depressions are parallel to the edges of the fossae that ultimately break the surface of the depressions.

We hypothesize that the sequence of events at the BRDF and NDF began with the creation of an elongate depression at the surface above underlying dikes, but with a surface width that extends beyond the dike margins by up to several dike widths (Fig. 29A). The surfaces likely represent subsidence above the dike in response to volume loss, ostensibly the result of heat from the dike melting ground ice. Head et al. (2003) also suggest ground

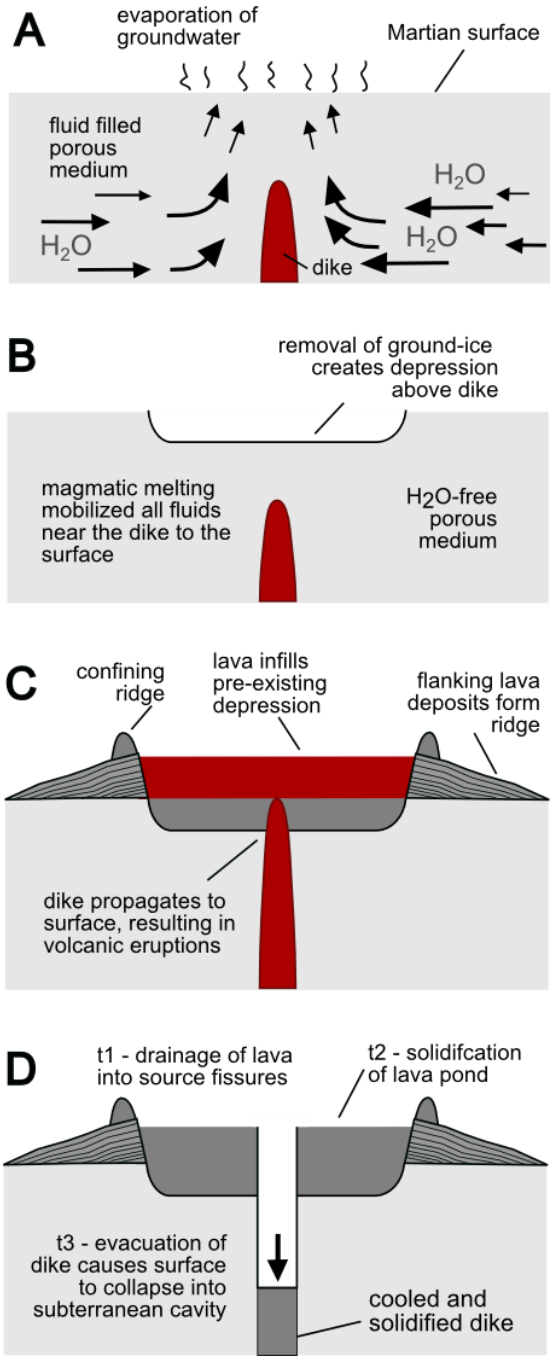

Figure 29. Proposed formation model for category 1 features (BRDF and NDF) consists of four stages labelled A, B, C, and D. Magmatic dikes are proposed to have subsided after eruption of copious lavas, resulting in surface collapse into a subterranean cavity in the final stage of formation (D). In stage A, a magmatic dike intrudes into an ice-rich, permeable substrate. Volume loss results from the evaporation of volatiles that were magmatically heated in stage B. As the dike intersects the surface, eruptions occur, forming a lava lake that locally overspills forming a confining ridge in stage C. Finally, in stage D, the lava lake cools, solidifies, and drains into a subsurface evacuated dike cavity.

ice removal as a mechanism to create depressions along the Cerberus Fossae, attributing magmatic dikes as the responsible heat source. The sharp edges of the subsiding areas likely reflect that collapse happened along the vertical cooling cracks within the lavas that define the Athabasca Plains prior to the formation of the Cerberus Fossae (Fig. 29B). In some places, the edges of the collapse are more gradual. Regardless, once the elongate depressions were formed, lava that ultimately erupted from the dikes filled in these depressions, forming lava lakes (Fig. 29C) that oriented both orthogonally (Figs. 19, 26) and parallel to the fossae (Figs. 19 and 24). Orthogonal and parallel lava lakes similar to those at the NDF and BRDF exhibit a morphology unique among terrestrial and other Martian systems, possibly making their formative process unique to the Cerberus Fossae, Mars.

The elongate depression that parallels the NDF and is about 800 m to its south resembles the depressed surface that encompasses the BRDF, but contains a second nested depression (Figs. 17, 19, 24, and 25) that provides important insights into the progressive development of the fossae. The nested trough within this elongate depression has edges defined by parallel and overlapping fractures that crosscut the original depressed surface, indicating that the central, nested trough represents a relatively later stage of fossa formation, but one that predates the creation of a wide, deep fissure. The fractured edges of the nested trough contrast with the sharp, near-vertical scarps that define the outer boundaries of the elongate depressions around the central fossae. We interpret the central, nested trough to be structurally controlled. A fault may underlie the monoclinal surface, with parallel and overlapping fractures along the monoclinal crest (Fig. 25). Analogous monoclines are interpreted to have formed above upward-propagating normal faults in lavas in Iceland (e.g., Grant and Kattenhorn, 2004). Normal faults are common above subsurface dikes (Rubin, 1992); therefore, the nested trough in Fig. 25 may reflect a small-scale graben feature above an underlying dike that began to dissect the surface of the pre-existing elongate depression. Alternatively, the nested trough may mark the intersection of the dike

itself with the surface, with later evacuation forming a central fissure (fossa). Evidence for the latter is provided by the nature of the depressed surfaces alongside the fossae, which show clear evidence of having been filled with lava that erupted from the underlying dikes (Fig. 9 and 11).

We interpret the ridges and scarps along the periphery of the depressed surfaces to result from drained lava lakes. Lava lakes on Earth are observed to have 5-8 m tall, narrow, and near-vertical levees confining a lava pond a few hundred meters across. One example is the 17-21 February 1992 eruption of Kilauea, Hawaii (Heliker et al., 1998). The levees were composed of small overflows emplaced as the lava pond level gradually increased during a series of small surges. Similar near vent constructs are observed on the Burfells lava flow in Iceland (Keszthelyi et al., 2004). The changing character of the peripheries of these lava lakes likely reflects the combined effects of the formation process of the original elongate depressions that formed above underlying dikes that were filled with lava and the effect of lava lake infill and later drainage. For example, the discontinuous scarp in Fig. 26 may have resulted from lava spillovers that breached the periphery of the lava lake, permitting the flow of lava downslope away from the fossa. Similar breakouts have been described for other leveed lava ponds along the Cerberus Fossae (Keszthelyi et al., 2008).

Lava flows may have travelled southwards from the breakout site along the NDF (Fig. 28). Similar subtly defined flows are shown along the BRDF (Fig. 15). In both examples, MOLA topography demonstrates the surfaces are sloping away from the associated fossae, possibly suggesting they originated from the fossae. However, there lacks evidence that directly correlates these flows with the associated fossae source. The flow surfaces are texturally muted, lacking albedo variation that may suggest disrupted a'a' or ropy pahoehoe. The morphology of the flow surfaces consists of slightly raised surfaces with a lobe-like morphology that are consistent with inflationary flows (Keszthelyi et al., 2000, 2008). The scale of the flows on the flanking surfaces of the BRDF and NDF are also similar to many

terrestrial lava flows (e.g., Keszthelyi and Pieri, 1993; Mattox et al., 1993; Whitehead and Stephenson, 1998; Keszthelyi et al., 2000). The flows are 100s of meters across and several kilometers long, oriented with their long axis parallel to the steepest slope (perpendicular to the orientation of the fossae). Lava flow inflation is a process that results in the lifting of a solidified crust due to continued injection of molten rock into the interior of the flow (Walker, 1991; Hon et al., 1994). Inflation can form in any type of lava flow, but is most common in pahoehoe sheet flows (e.g., Self et al., 1998). The close proximity and downslope direction of the flows relative to a possible source (the fossae), along with flow characteristics and dimensions that are similar to pahoehoe and inflationary lava flows on Earth, suggests that the deposits in Figs. 15 and 28 are volcanic. We infer that the deposits were emplaced due to local spill over from the lava lake contained within the depressions that now surround the fossa.

Alternatively, the flow deposits in Figs. 15 and 28 could be of sedimentary origin, produced by lahars. However, we consider this less likely given their consistent raised flow surfaces and lack of chaotic flow textures or cuspate morphologies that we later demonstrate to be associated with the emplacement of lahars adjacent to the fossae (see section 6.3.2. Crater Fossa).

The exposed upper surfaces of the depressed areas alongside the BRDF and NDF provide additional evidence for the presence of lavas within these depressions. The polygonal textures on these surfaces (Figs. 12, 13, and 23) are characteristic of cooled lava flows (e.g., Fig. 16). A range of polygonal textures is reported on volcanic channel surfaces in Athabasca Valles (e.g., Jaeger et al., 2007, 2010). Where the depressed surface around the BRDF is crosscut by the fossa (Fig. 12), the polygonal surface forms a topographic dome, interpreted here to have formed as a result of lava inflation on the surface of a lava pond. Gas build up beneath the surface of lava ponds has been reported within the

Halemaumau crater, Hawaii (Rowland and Munro, 1993), and a similar process may have resulted in the relative uplift of the dome on Mars.

Some of the variability along the boundaries of the depressed areas surrounding both the BRDF and the NDF, such as near vertical scarps and partially collapsed and sloping surfaces (Figs. 14 and 23) may also be related to draining lava lakes. For example, in Fig. 14, lava along the edges of the lava pond may have hardened against the edges of the mesa that separates the overlapping fossae. When the lava within the lava pond retreated into the associated fossae or drained through the boundary of the lava lake and down the regional slope, some portions of the edge of the lava lake remained as vertical cliffs, whereas in other portions the edge of the hardened lava layer slumped down to produce the ramps observed in Figs. 14 and 23.

Taylor et al. (2013) suggest that the fossae that crosscut the surfaces that surround the BRDF and NDF formed as a result of normal faulting. However, additional formation mechanisms may have contributed to fossae formation, such as the evacuation of subsurface magmatic dikes. The wide, deep fissure created by the 10th Century Eldgjá eruption in Iceland bears a striking resemblance to the Cerberus Fossae. Eldgjá is an eruptive fissure remnant (an evacuated fissure; 600 m wide and 270 m deep) caused by lava draining back into the fissure to a level below the fissure rim at the conclusion of the eruption. The Eldgjá event was the most voluminous fissure eruption in recorded history, erupting approximately 19 km^3 of basalt lavas from a ~60 km long fissure system.

Given that BRDF and NDF reside along a ~100 km long fossae that apparently sourced large volumes of lava that characterize the near-fissure morphology and the regional topography, it is not unreasonable that a high magma production rate (analogous to Iceland's Eastern Volcanic Zone (EVZ), where Eldgjá erupted) resulted in a surface manifestation of fissures at Cerberus similar to that of the EVZ. Building on this inference, Pendleton et al. (2013) compare the widths and depths of a ~500 km long array of subparallel fossa at

Cerberus Fossae and find a width to depth ratio of 2 to 3:1 (R^2=0.8225). These values were calculated using MOLA point data that fall within the fossa and geometric data estimated from aerial imagery. A consistent ratio across the fossae implies that a similar formation mechanism may be responsible for their formation. In comparison, normal fault systems that comprise graben on both Earth and Mars have greater width to depth ratios. Icelandic normal fault systems have width to depth ratios of ~125:1 (Tentler and Mazzoli, 2005) and other Martian rift systems have ratios of ~10:1 (Wilson and Head, 2002). The width to depth ratio of Eldgjá, however, is has a smaller width to depth ratio of ~2:1 that is consistent with the results of Pendleton et al. (2013) for the Cerberus Fossae. Thus, instead of forming as normal faults, the possibility exists that the fossae represent magmatic dikes that evacuated at the surface in a manner similar to the EVZ.

An evacuated dike model can also explain the creation of near-vertical fossa walls with stratigraphic layers exposed that are variably eroded. If a magmatic dike evacuated the BRDF and NDF, near-vertical walls would be an expected result from the upward propagation of the magmatic dikes. The steep fossa walls show terraces that appear eroded in a similar style in which the Columbia River flood basalts in the northwestern United States (e.g., Reidel, 1998) and the Deccan Traps in India (e.g., Jerram and Widdowson, 2005) have eroded over time. Additionally, mass wasting processes have also facilitated the collapse of the near vertical fossa walls and appears to be a dominant control on their geometry rather than structurally controlled fossa walls by normal faults as suggested by Taylor et al. (2013).

6.2. Category 2: Fossae flanked by irregular, orthogonal, or trough-like depressions

Two field sites are described in this category (locations in Fig. 6) that share similar characteristics despite being separated by 515 km. We refer to the field sites as the Terraced Depression Fossa and the Orthogonal Protrusion Fossa, respectively. Similar characteristics include cuspate and trough-shaped, amphitheater headed depressions or erosional

protrusions adjacent to the fossa walls. Multiple inset terraces within these depressions exhibit a range of surface morphologies. Descriptions comprise three parts: (1) topographic characterization, (2) evidence for modification in close proximity to the fossae, and (3) flow deposits on the flanks of the fossae.

6.2.1. Terraced Depression Fossa

6.2.1.1. Observations

The Terraced Depression Fossa (TDF; Fig. 30), located along a ~100 km long fossa in the eastern extension of the Cerberus Fossae (Fig. 5), and is a WNW-ESE oriented fissure that spans from 7.51°N, 167.93° E to 7.48°N, 168.06° E. The ~100 m wide fossa is flanked by a 15-20 m high topographic ridge (Fig. 31) with outer slopes of 0.86° to the north and 0.72° to the south of the fossa. The depth of the fossa demonstrated by MOLA is up to 24 m (Fig. 31); however, photoclinometry suggests a maximum relief of ~50 m. The vertical walls of the TDF comprise of a series of staggered, en echelon fractures (Figs. 30 and 32). Similar to other locations at Cerberus Fossae, resistant layers of rock where the fossa intersects the surface promote vertical cliff formation along the fossa walls and result in large, angular blocks that have fallen into the interior of the fossa (Figs. 32 and 33).

The context image for the TDF (Fig. 30) shows lobate flows directed away from the central fissure to both the north (Fig. 34) and the south (Fig. 30). The lobate snouts of the flows indicate the downslope direction to be perpendicular to the fossa. Flows emplaced on the north flank show multiple, superposing flows with digitate lobes at their terminations (Fig. 34B). The flows are constructional and their emplacement appears to be a primary control on the local topography adjacent to the fossa. The central fossa appears to have sourced the flows. Although distinct eruptive locations are not identifiable in Fig. 30, the fossa is flanked by a rough-textured depression that locally widens the fissure at a level slightly below the

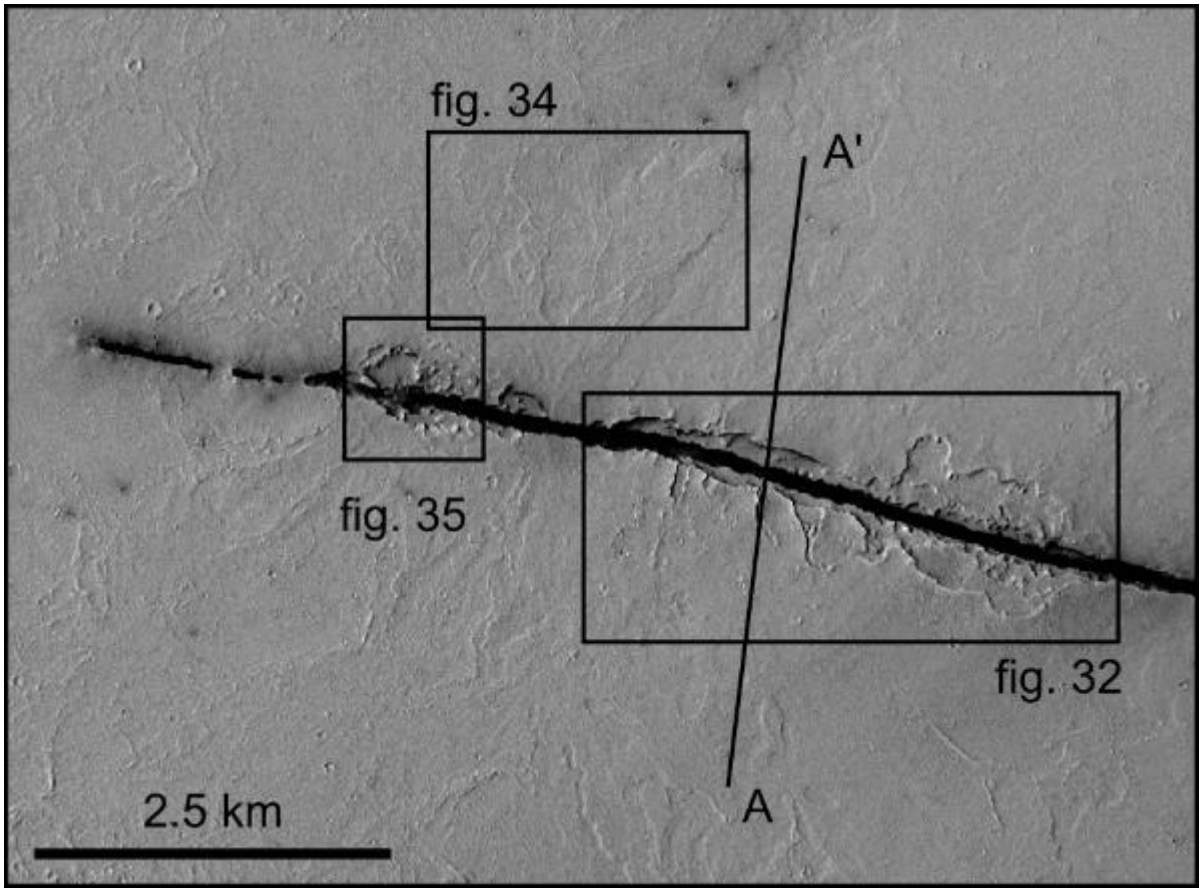

Figure 30. CTX image D17_033872_1877_XN_07N192W (5 m/pixel; north is up; see Fig. 5 for context) with center point 7.500°N, 167.990° E. A central fissure, referred to as the Terraced Depression Fossa, exhibits rough textured, flanking depressions with irregular boundaries (boxes labeled Figs. 34 and 35) and adjacent lobate flows (Fig. 32A, B) that are directed away from the fossa to both the north and south. See Fig. 31 for topographic profile A-A'.

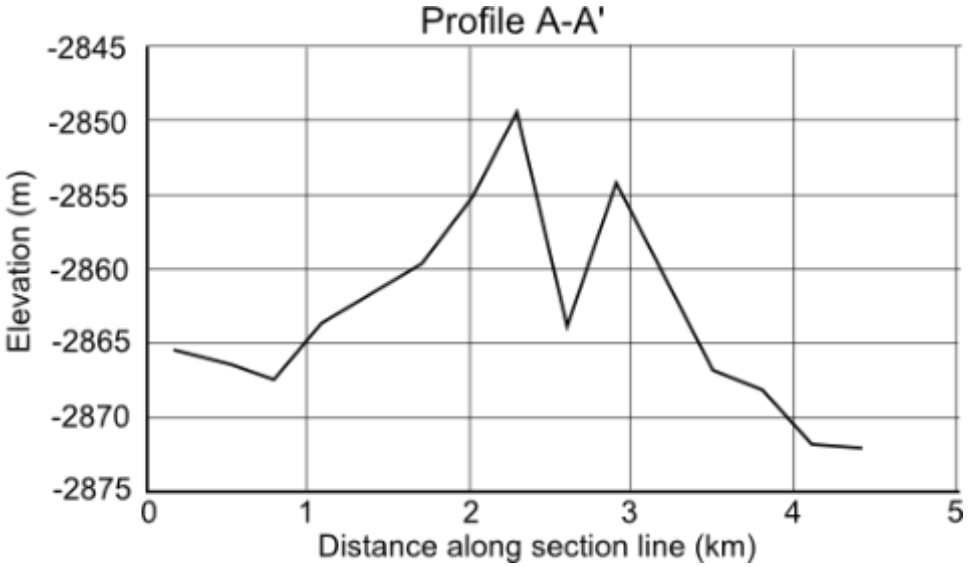

Figure 31. MOLA PEDR derived elevation data (orbit 11175) along profile A-A’ in Fig. 30. The fossa is flanked by a 15-20 m high topographic rise with outer slopes of less than 1°.

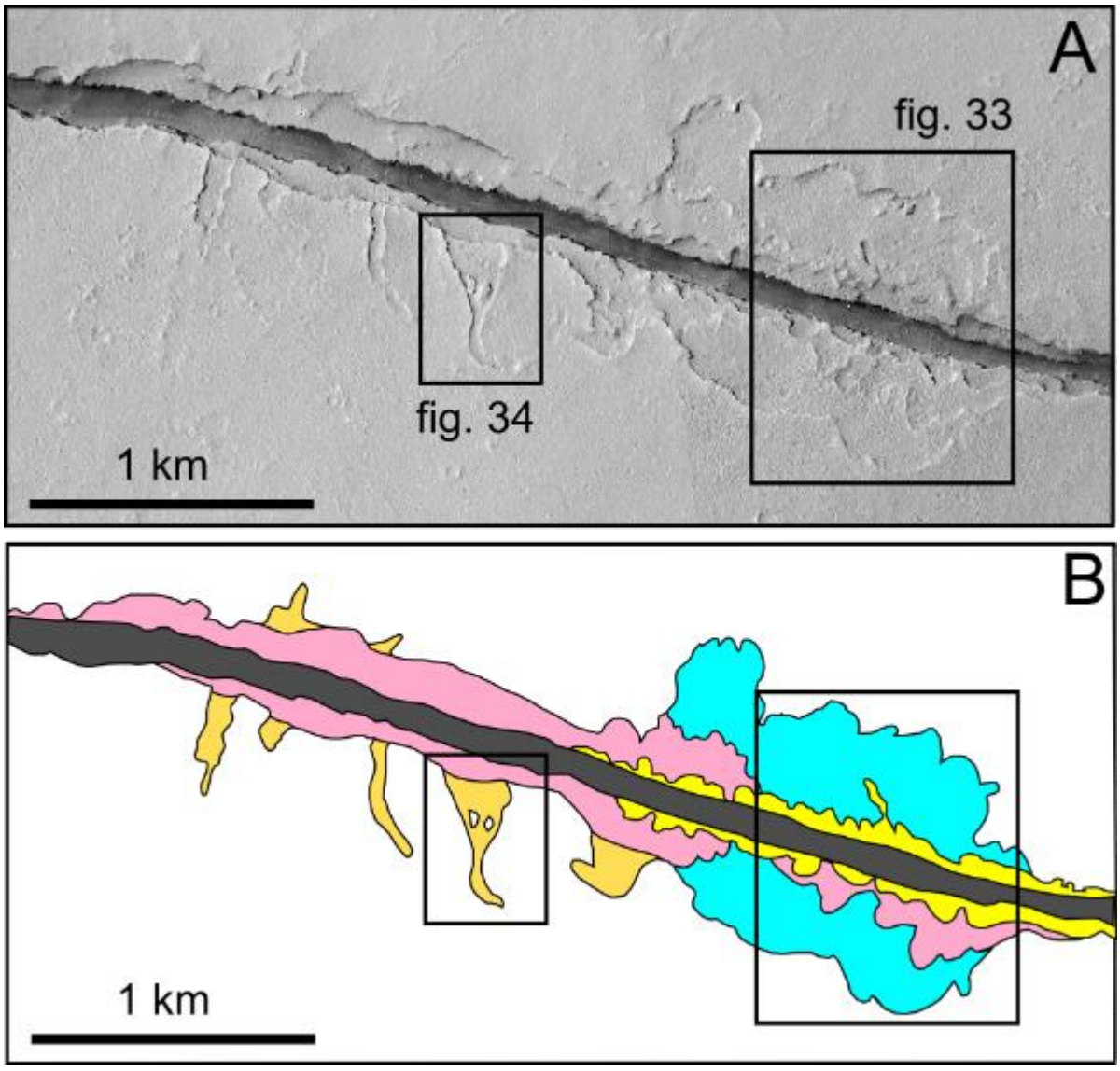

Figure 32. (A) Composite of HiRISE images PSP_008014_1875 (25 cm/pixel) and ESP_033872_1875 (25 cm/pixel) showing the Terraced Depression Fossa. See Fig. 30 for regional context. Locations of Figs. 33 and 34 are shown by boxes. (B) Simplified geologic map showing multiple terraces that step progressively lower in elevation toward the fossa interior. The fossa (dark grey) crosscuts the pink and yellow mapped surfaces. The orthogonal trough-forming orange surface is the topographically highest terrace that sits below the regional surface. It is crosscut by the pink surface, which cuts into the blue surface on both the north and south sides of the fossa. The yellow surface is the terrace with the lowest elevation, but stands higher than the fossa floor.

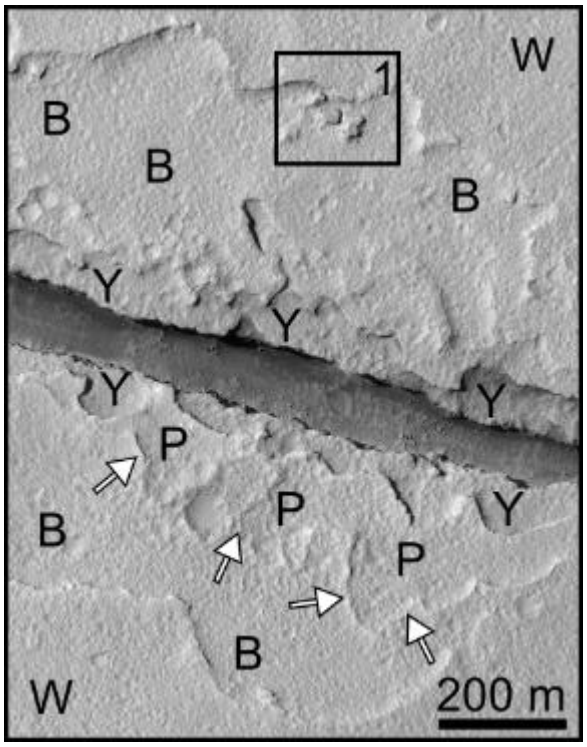

Figure 33. HiRISE image PSP_008014_1875 (25 cm/pixel) showing mapped terraces from Fig. 32, with letters denoting unit color (W = white; B = blue; P = pink; Y = yellow). Vertical scarps separate each mapped terrace. Arrows indicate a partially formed scarp that separates lower terrace P from higher terrace B. Box 1 identifies localized mesas of unit W surrounded by terrace B. Correlation of surfaces B and Y on opposing sides of the fossa is based upon similarity in morphological expression and inferred relative topographic elevation.

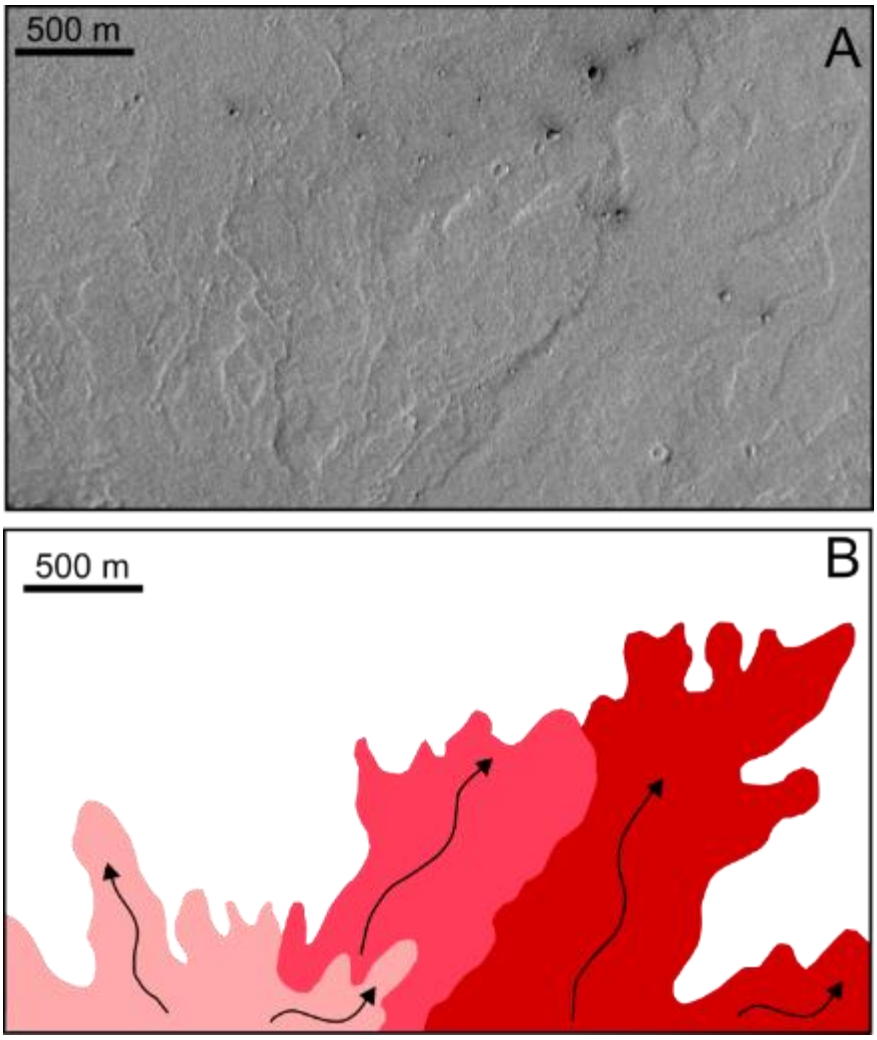

Figure 34. (A) CTX image D17_033872_1877_XN_07N192W (5 m/pixel; north is up; see Fig. 30 for context) showing surface textures and flow morphology to the north of the TDF. (B) Simplified geologic map showing three superposed lobate flows in red, pink, and light pink (oldest to youngest). Each flow has digitate flow margins. Arrows indicate the inferred flow directions.

regional slope in the general vicinity from where the flows emanate (Fig. 35). The presence of additional, relatively older lobate flows to either side of the fossa suggests that the entire length of the fossa acted as a source to the various lobate-flows emplaced on its flanks (Fig. 30), which can be traced from their termini to the fossa edges, where the flows are truncated.

In some cases, the deposits on the flanking slopes can be traced back to a location along the fossa that has a prominent depression bordering it (Fig. 30 and 35). The depression appears to cut the surrounding lobate flow surface and is also truncated by the WNW-ESE oriented fossa. The step-wise decrease in elevation along the mapped terraces to the interior of the fossa are possibly indicative of resistant layers at different stratigraphic depths, similar to the Nested Depression Fossa in Fig. 22. The fossa-facing scarp of each terrace (mapped in blue, pink, and yellow in Fig. 32B) is sinuous, in contrast to fossa walls that maintain consistent orientations along the length of a fossa, interpreted to be controlled by fracture segments. The uppermost terrace (blue in Fig. 32B) shows a semi-circular boundary that forms broad U-shapes that have widths between 200 and 800 m. The boundary between the pink and blue and the yellow and pink surfaces replicates the semi-circular boundary of the upper blue unit, but at a smaller scale (between 50 and 100 m).

The stratigraphic level of the terraces (Fig. 33) is evident on both sides of the fossa, with uppermost surface W (composed of the lobate units), followed by depressed terraces B, P, and then Y at the lowest level. All but terrace P are identifiable on both sides of the fossa, with similar morphological characteristics and inferred surface elevation. The boundary between surfaces P and B to the south of the fossa is subtly exposed (white arrows in Fig. 33) and is similar in form to the boundary between surfaces B and W. The escarpments that define each of the terrace boundaries are similarly near vertical and show accumulations of 3-5 m diameter boulders on the fossa floor below. The stepwise descent onto lower, narrower terraces in closer proximity to the fossa walls indicates that lower terraces cut higher ones. Remnants of existing surfaces may be isolated during the incision process,

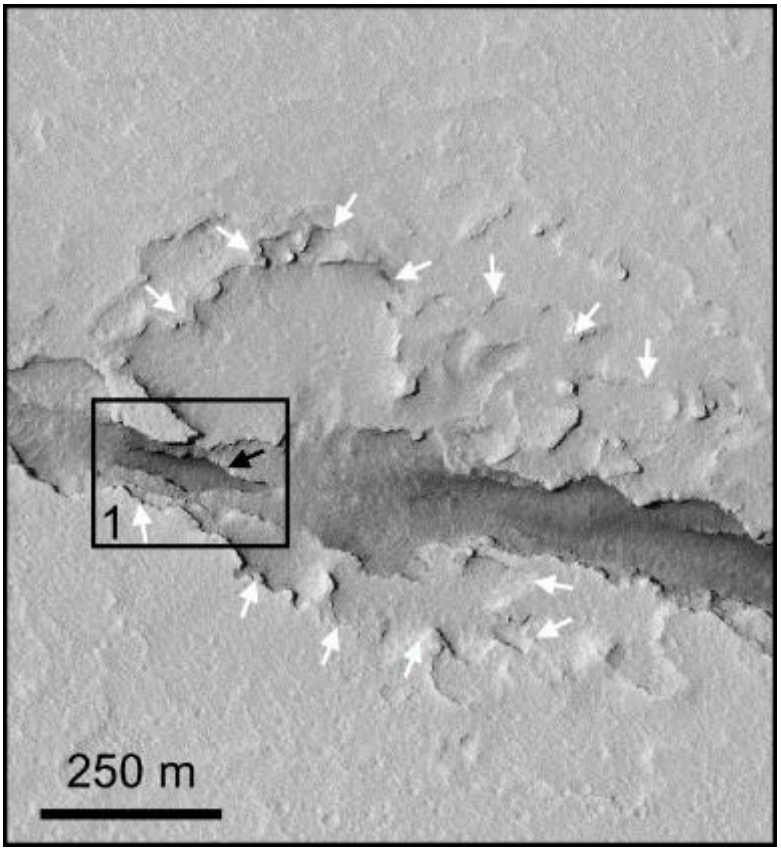

Figure 35. HiRISE image PSP_008014_1875 (25 cm/pixel) showing a cavity with an irregular sharp boundary (white arrows) located at the western portion of the Terraced Depression Fossa (Fig. 30). The character of the cavity mimics some of the shapes observed on the more pronounced terraced depression (Fig. 32). This feature is topographically higher than the lobate flows shown in Fig. 34. Box labelled 1 shows a portion the inner-most portion of the Cerberus Fossa.

such as the isolated mesas of surface W (box 1 in Fig. 33) that stand above the relatively flat floor of surrounding terrace B, located 20 to 50 meters away from the boundary between surfaces B and W.

Similar mesa-like landforms occur within a trough-like feature located on the southern side of the fossa, ~1 km to the west (surface O in Fig. 36; orange unit in Fig. 32). These elongate and angular mesas have near-vertical walls and a flat upper surface that is inferred to be a remnant of surrounding surface W. This trough is one of at least seven similar features that are oriented almost perpendicular to the walls of the fossa. Surface O appears pitted, resembling all other terrace surfaces (Figs. 33 and 36) as well as the fossa-adjacent lobate flow surfaces (Figs. 30 and 34). Crosscutting relationships between the surfaces in Fig. 36 show that surface O incises into uppermost surface W, whereas lowermost surface P crosscuts both surfaces O and W. The truncation of terrace P by the fossa may be a crosscutting relationship if the fossa is the youngest feature to have developed. The jagged scarp separating each terrace is different from the more linear, fracture-dominated edges of the fossa. The scarp that separates surfaces O and W is measured by photoclinometry to be around 10 meters high along most of the length of the trough. Surface O appears to stand higher than surface B (blue unit in Fig. 32) further to the east; however, surface B extends outward from the fossa beyond the furthermost extent of unit O, indicating that incision by unit B may have removed unit O in those more easterly locations.

6.2.1.2. Interpretations

Lobate deposits on the flanks of the terraced depression imply a flow direction away from the fossa (TDF) to the both the north and south (Figs. 30 and 34). The lobate flows are superposed and compounded to create a constructional topographic high along the margin of the fossa (Fig. 31), similar to fissure eruptions on Earth. The lobate deposits are crosscut at

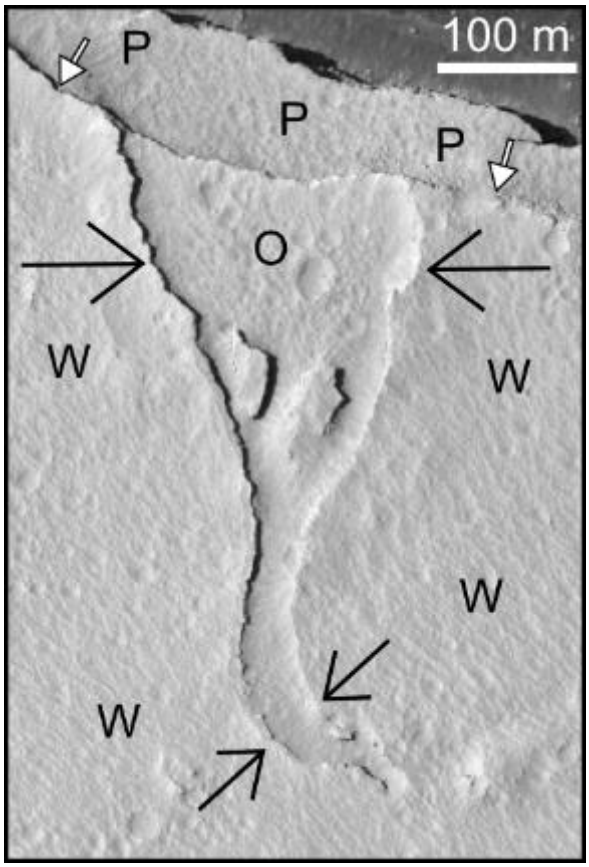

Figure 36. HiRISE image ESP_033872_1875 (25 cm/pixel; see Fig. 31 for context) showing a ~40 m wide trough (in the south, smaller black arrows) that opens into a ~225 m wide valley (in the north, larger black arrows) with increasing proximity to the fossa, where it is truncated by terrace P (white arrows). Mapped surfaces are shown with letters to denote corresponding color in Fig. 31 (W = white; P = pink; O = orange).

their upslope end and truncate against the near-vertical walls of the fossa (Fig. 30) as well as the terraced depression (Fig. 32).

We interpret the lobate deposits to be lava flows that erupted from a linear fissure in the location of the central fossa. These flows were emplaced prior to the more recent event that created the fossa itself, whether through subsidence above a dike due to graben development (Rubin and Pollard, 1988) or collapse of a highly fractured zone of rock into a subsurface magma conduit (Mastin and Pollard, 1988). Furthermore, the truncation of these lobate flows by the terraced depression alongside the fossa suggests that the process that created the terraced depression occurred after the lobate flows were emplaced on the flanks. The terraced depression scarps are truncated by the fossa wall, indicating that the formation of the fossa occurred after the development of the terraced depressions. Hence, fossa formation (i.e., the development of the deep fissure) was the most recent event.

One potential scenario is that the terraced depression formed synchronously with the emplacement of the lobate flows on the fossa margins from collapsed lava ponds. Perched lava ponds form at the surface above magmatic conduits and are commonly associated with both channels and spatter cones (Greeley, 1977; Blackburn et al., 1976). At the terraced depression along the TDF, however, there lacks evidence for lava channels sourced from the fossa and directed downslope, such as we interpret south of the Nested Depression Fossa in Fig. 30. We also do not observe spatter cones or ramparts along the edge of the fossa, which are commonly observed in close spatial association with eruptive centers (low shields) on Mars (Hauber et al., 2009) and more specifically, lava ponds (Blackburn et al., 1976).

An additional, possibly defining characteristic of lava ponds is that they exhibit relatively flat topography (Neukum et al., 2005). Lava ponds may exhibit terracing (such as the Olympus Mons or Tharsis Montes summit depressions) caused by withdrawal of magma and subsequent collapse that produces nearly vertical scarps that define each terrace (Neukum et al., 2005). However, the diameter (i.e., width) of the terraces at the summit of the

larger shield volcanoes on Mars (hundreds of kilometers) are far greater than the terraced depressions in Fig. 33 (hundreds of meters). If the terraces that comprise the terraced depression resulted from distinct stages of magma withdrawal in the subsurface, as would be needed to create the observed morphologies; the sequence of events would require multiple episodes of near instantaneous depressurization of magma. Such events would cause magma withdrawal beneath the frozen lava pond surface that would cause collapse and formation of fractures at the surface. However, no such fractures are observed along the terrace boundaries. Instead, we see cuspate, scalloped, and resistant stratigraphic layers along the edges of the depressed terrace surfaces that are inset into each other. Therefore, we do not favor a lava pond model for the formation of the terraced depression.

We instead hypothesize that the terraced depression surfaces formed as a result of subsurface aqueous flow and associated erosion. A cavity located on the western end of the Terraced Depression Fossae also exhibits morphological characteristics that are reflective of phreatomagmatic cavities seen along the Great Rift of the Snake River Plain. A close up of the cavity in Fig. 35 shows an irregular boundary with multiple terraces that might have formed after a phreatomagmatic event. While we speculate on the point of phreatomagmatism, other positive relief structures are not observed, such as an identifiable source vent, to diagnose its formation with more accuracy.

The uppermost and oldest terrace (based on the assertion that deeper surfaces incised into higher surfaces) is unit O (Fig. 33), which displays troughs oriented perpendicular to the fossa walls. High-standing pinnacles within the confines of the trough (Fig. 36) are elongate and resemble streamlined forms that develop as a result of megaflooding elsewhere along the Cerberus Fossae (Burr et al., 2002a,b); however, their angular shape contrasts with the smooth boundaries typical of the upstream end of streamlined islands. Mesas that stand abandoned within the stratigraphically highest terrace B (box 1 of Fig. 33) are also angular with flat upper surfaces and are located immediately

adjacent to the northern edge of the terrace. We interpret these pinnacles and mesas to have formed as a result of subaqueous flow that preferentially eroded the material surrounding them.

A process that could be responsible for this inferred erosion is groundwater sapping (Laity and Malin, 1985), caused by seepage and subsequent runoff that is generated at a landscape irregularity, such as a topographic depression, or due to differences in the hydrological properties of the soil (Marra et al., 2014). Groundwater sapping is an erosional process that can create features with unique characteristics (Laity and Malin, 1985). One of the most pronounced landforms that may result are amphitheater-headed valleys (Kochel and Piper, 1986; Howard and McLane, 1988; Dunne, 1980, 1990). Tapered terminations, and a relatively smooth, concave-up profile of theatre-headed valleys is also characteristic of groundwater seepage features (Laity and Malin, 1985). Lamb et al. (2006) show that similar amphitheater morphologies can form as a result of waterfall erosion by overland flow of competent bedrock; however, the stratigraphic layers within the NDF imply a resistant, volcanic lithology that was likely resistant to erosion. Regardless, both groundwater sapping (Kochel and Piper, 1986; Howard and McLane, 1988; Dunne, 1980, 1990) and overland flow (Lamb et al., 2006) imply the flow of liquid water, either in the subsurface or at the surface.

Accordingly, we interpret the trough-like form (surface O in Fig. 36), the width of which narrows away from the fossa, as being the result of a flowing fluid in the subsurface, perhaps combined with groundwater seepage. Near-vertical scarps separating surface O and W are jagged, and do not appear to be controlled by fracture pathways parallel to the associated fossa, implying a non-structural process for the development of the terraces. The shape of the trough and all others defined by surface O implies that this fluid flowed toward the fossa, from no more than ~500 m away. The topography of the constructional lava ridge that flanks the fossa peaks at this same approximate distance from the fossa (Fig. 31), implying that the subsurface fluid flow may have followed the fossa-facing inward slope of

these earlier formed topographic ridges. The groundwater flow slowly eroded the regional surface (W in Fig. 36) to form surface O as the fluid traveled along stratigraphic layers towards the interior of the fossa. The tapering form of the trough implies progressive incising of the lobate deposits adjacent to the fossa, headward and away from the wall of the fossa in a perpendicular direction, similar to the formation of groundwater seepage features observed on both Earth (Laity and Malin, 1985; Kochel and Piper, 1986; Schumm et al., 1995) and Mars (Goldspiel and Squyres, 2000; Howard, 1988). Similar morphological forms have been replicated experimentally to have formed as a result of groundwater seepage (Marra et al., 2014).

We hypothesize that different stages of groundwater seepage at different times created the terraced appearance of the depression (Figs. 32, 33, and 36). After surface O incised into surface W, surface B crosscut both surfaces O and W, presumably in response to groundwater seepage from a deeper stratigraphic level. Groundwater sapping at a deeper level implies a correspondingly deeper depression at the surface to serve as an outlet for the groundwater. This may imply that the fossa was in an early stage of development that involved the progressive deepening of a linear depression while the successive terraces developed, providing a sink into which groundwater flow was directed. Similarly, terraces formed successively at the levels of surfaces P and Y, incising into the higher terraces. Terrace formation ultimately ceased as the fossa developed to its current depth through a structurally-controlled process that left en echelon fractures exposed along the near-vertical fossa walls.

6.2.2. Orthogonal Protrusion Fossa

6.2.2.1. Observations

Sinuous troughs are associated with a linear, 18.3 km-long fossa, centered at 8.429° N, 159.184° E, and is referred to here as the Orthogonal Protrusion Fossa (OPF; Fig. 37). The fossa is up to 580 m wide, with an average width of ~150 m. The fossa crosscuts two different units: a Late Amazonian volcanic unit (lAv) and a Hesperian to Noachian transition unit (HNt) (Tanaka et al., 2014). The fossa width is greatest in the HNt unit, but decreases within the IAv volcanic unit. In the HNt unit, the slopes along the edges of the fossa have produced large volumes of talus material that moved migrated downward, causing geomorphic widening of the fossa. In contrast, the fossa crosscutting the volcanic unit has near-vertical walls with little to no talus material below them, reflecting structural control on fossa width. The difference in fossa width indicates a higher mechanical strength of the volcanic unit, whereas the HNt unit is more likely a loosely consolidated granular material that responded to being crosscut by fractures with mass wasting of sediment into the fossa interior. Where the fossa crosscuts the volcanic unit, it achieves a depth of up to 70 m in the MOLA PEDR dataset (profile D-D’ in Fig. 38).

Topographic profiles drawn perpendicular to the fossa (Fig. 38) reveal a topographic rise that extends along the length of the fossa (labeled as fossa rise, FR), analogous to the topographic ridge observed along the Terraced Depression Fossa (Fig. 31). In profile D-D’ the fossa rise is less pronounced relative to the vertical relief within the HNt unit, which is composed of multiple mesas and channels (MDCH). Based on the topographic profiles, the fossa appears to be located within a saddle between two inward dipping regional slopes; however, these slopes are only on the order of 0.05° and likely reflect an uneven regional surface of constructional lavas. The maximum slope of the fossa rise is 0.42° (the south

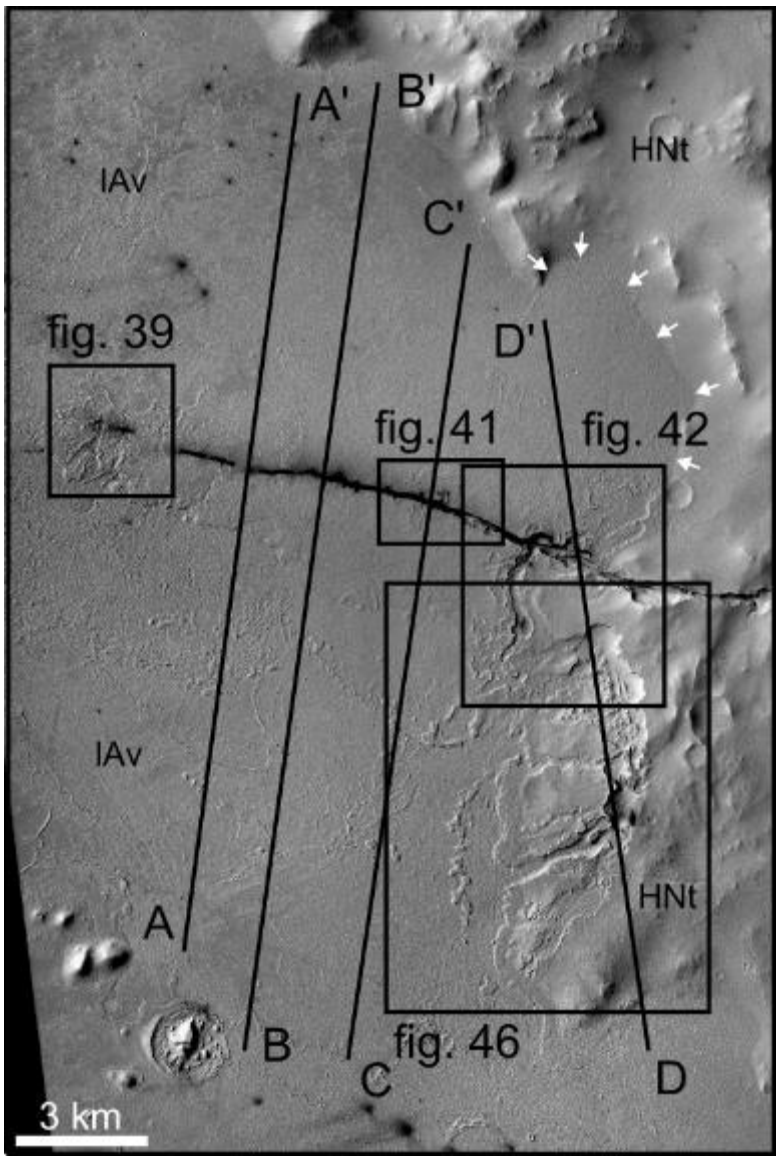

Figure 37. CTX image G19_025710_1884_XN_08N200W (5 m/pixel; north is up; see Fig. 5 for context), centered at 8.429° N, 159.184° E. Regional view of the Orthogonal Protrusion Fossa (OPF). Modified surfaces adjacent to the fossa include channels (Fig. 46), orthogonal protrusions (Figs. 41 and 42), and terraces that step progressively lower in elevation (Fig. 42) toward the fossa interior. A topographically higher terrain from which pronounced channels emanate and feed into the surrounding, lower-lying plains is observed close to the fossa (see Fig. 46 for details). See Fig. 35 for topographic profiles A-A', B-B', C-C', and D-D'.

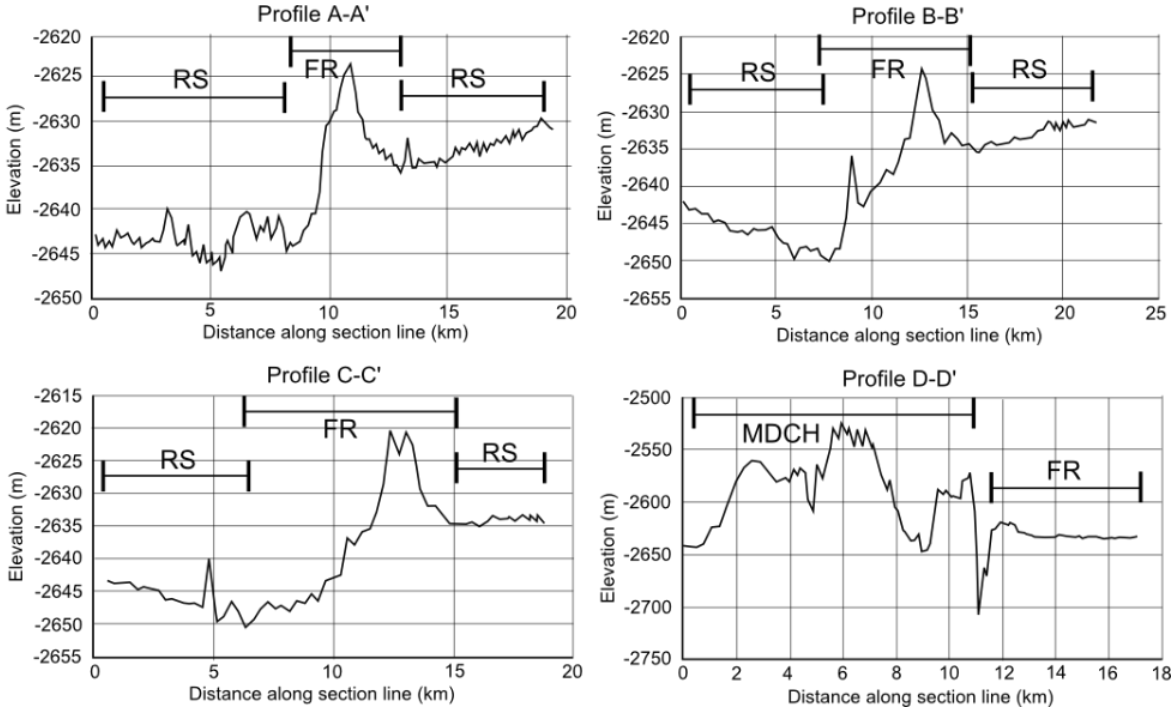

Figure 38. Topographic profiles generated from MOLA PEDR point data along profile lines as shown in Fig. 37. Profile lines and corresponding MOLA orbits are as follows: A-A' (orbit: 10999 and 12068), B-B' (orbit: 16344), C-C' (orbit: 11414), and D-D' (orbit: 16904). Profiles A-A', B-B', and C-C' show a topographic ridge that corresponds to the fossa in Fig. 37. Profile D-D' crosses the Noachian-Hesperian transition unit of Tanaka et al. (2014) and exhibits a total relief of ~160 m, whereas the other three profiles show a maximum relief of 30 m across a Late Amazonian volcanic unit. The OPF is visible in profile D-D' but was not resolved in the other profiles due to its small width compared to the spacing of MOLA PEDR data points. FR: fossae rise; RS: regional slope; and MDCH: mesas and channels.

facing slope between 8 and 11 km in profile A-A') and the minimum slope of the fossa rise is 0.24° (the south facing slope between 6 and 13 km in profile C-C').

Topographic slopes on the sides of the fossa appear to be controlled by eruptive deposits on the fossa flanks. Figure 39 shows an example vent on the western end of the fossa that sourced fluid from two elliptical pits that each have dimensions of ~315 m x 100 m. A somewhat anastomosing network of channels appears to emanate from the elliptical pits (white arrows in Fig. 39). Channel widths close to the pit source are between 75 and 115 m, but widen to between 150 and 400 m at their termination 1.3 to 1.5 km downslope. The channels appear to incise into the deposits adjacent to the pits and form topographic lows relative to their surroundings. Lobate ridged deposits <1 km north of the channel source pits (Fig. 39) form outer boundaries to surfaces that have a polygonal texture (Fig. 40) that lacks dust cover and appears topographically flat. Based on its close proximity and outward directed lobate shape of its enclosing ridges, we infer the polygonal deposit to be sourced from the associated pit directly to the south.

Evidence for eruptive sites are not restricted to the western end of the fossa. In the vicinity of Fig. 41 (see Fig. 37 for regional context), lobate flows with steep flow margins (black arrows) appear to be sourced from the fossa. Topographic profile C-C' demonstrates the downslope direction to be toward the north (Fig. 38). Incising into the deposit are two protrusions that are oriented approximately orthogonal to the fossa (white arrows in Fig. 41), and resemble the orange unit along the Terraced Depression Fossa (Fig. 32). These protrusions extend no more than 200 m perpendicular to the fossa wall and appear to have removed material from the fossa edge. At their intersection with the fossa wall, the protrusions are ~100 m wide.

A slightly larger protrusion on the north side of the fossa (blue in Fig. 42 and enlarged in Fig. 43) has a width at its intersection with the fossa of 300 m and continues for 400 m away from the fossa. The protrusion curves eastward away from the fossa and tapers

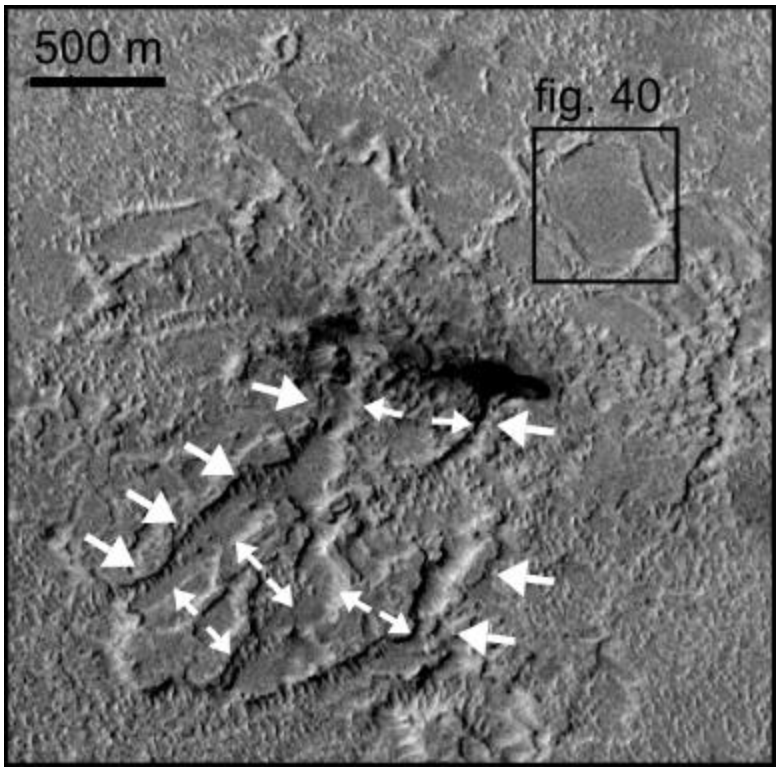

Figure 39. CTX image G19_025710_1884_XN_08N200W (5 m/pixel; north is up; see Fig. 37 for context). Pits at the western end of the OPF are the source of channels (white arrows) that appear to direct flow southward. Lobate ridges north of the pits bound a surface with a polygonal morphological character (Fig. 40).

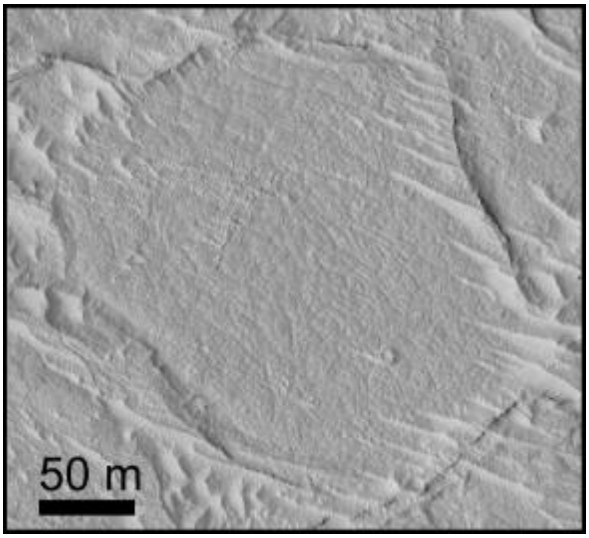

Figure 40. HiRISE image ESP_038092_1885 (25 cm/pixel; north is up; see Fig. 39 for context) showing a ridged feature that encloses a surface with a polygonal texture. The domed polygons are delineated based on dark albedo lines that form a network around the polygons.

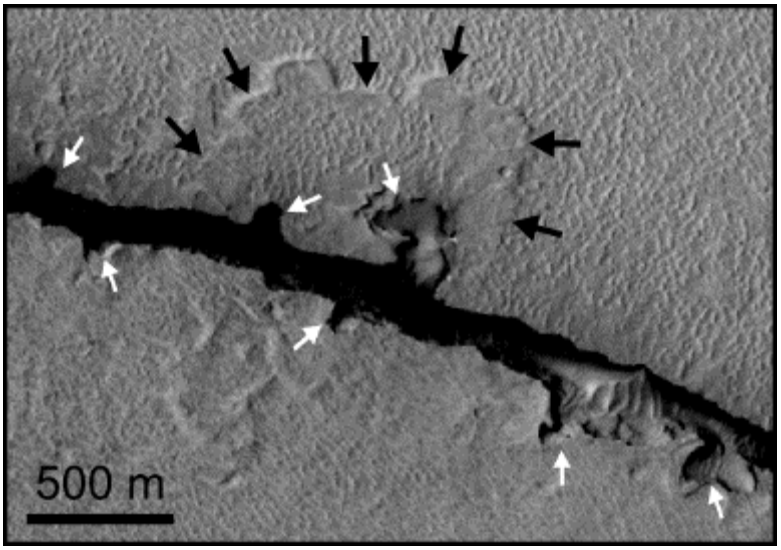

Figure 41. CTX image G19_025710_1884_XN_08N200W (5 m/pixel; north is up; see Fig. 37 for context). Protrusions extend perpendicularly away from the fossa (white arrows) and occur on both fossa walls. The protrusions appear to incise the material that comprises the surface around the fossa. Black arrows delineate a lobate deposit that extends up to 700 m from the fossa wall and is incised by at least two protrusions.

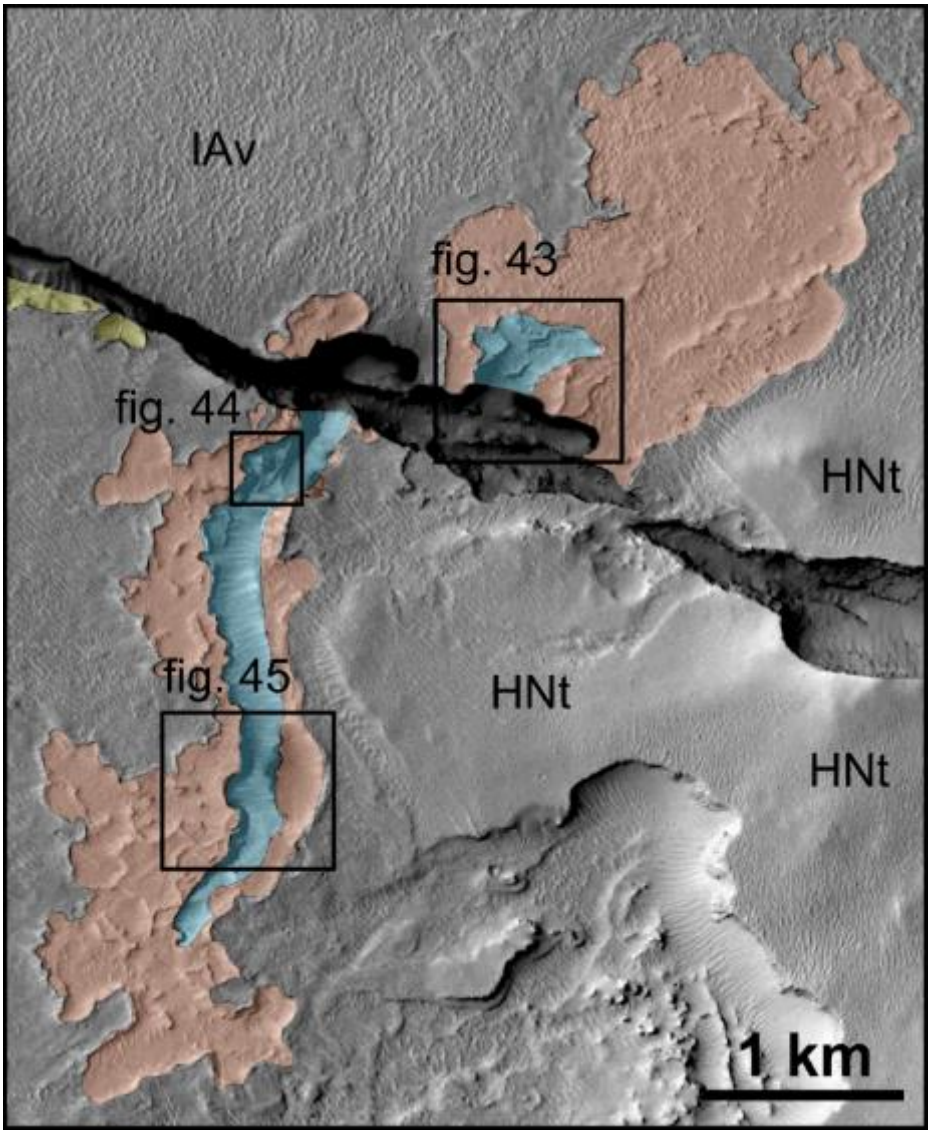

Figure 42. CTX image G19_025710_1884_XN_08N200W (5 m/pixel; north is up; see Fig. 37 for context), showing the region where the Channeled Depression Fossa intersects the Hesperian Noachian transition unit (HNt; Tanaka et al., 2014). Channel-like depressions and protrusions (blue) extend both north and south of the fossa, and incise an enclosing terraced surface (orange). The orange surface appears to be topographically lower than the surrounding regional surface.

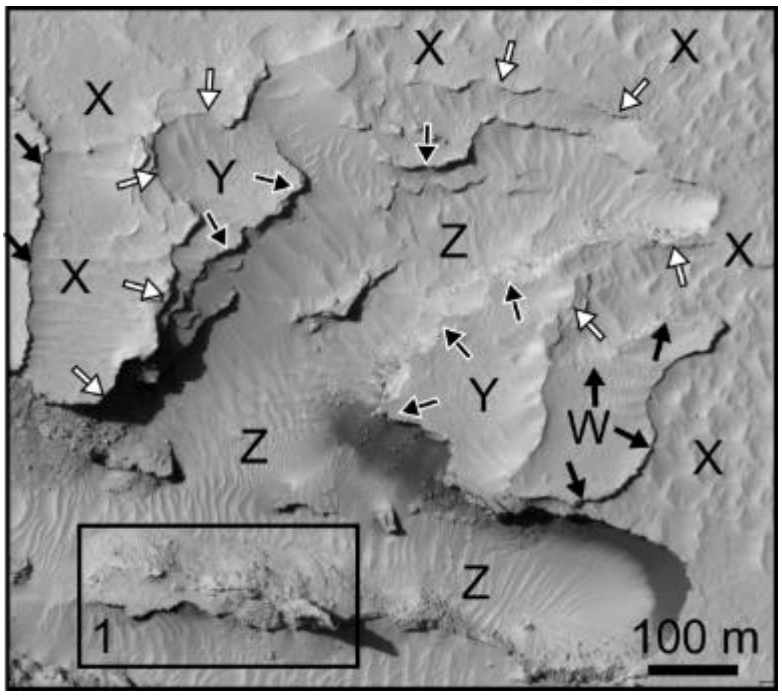

Figure 43. HiRISE image ESP_025710_1885 (25 cm/pixel; north is up; see Fig. 42 for context). Multiple terraced surfaces occur adjacent to a large protrusion (mapped in blue in Fig. 42) that extends out from the fossa and incises into a surrounding surface (orange in Fig. 42). The protrusion creates a ramp from the fossa floor up to the top of surface X. In stratigraphic order from highest to lowest, the terraces are W, X, Y, and Z. Box 1 shows an elongate ridge within the fossa that rises above the fossa floor. The E-W elongation of the ridge is parallel to the orientation of the fossa.

towards its distal end (Fig. 43). Another similar, but larger, morphological feature extends to the south of the fossa (blue in Fig. 44 and enlarged in Fig. 45). Although this larger protrusion extends ~2.8 km to the south of the fossa, its width at the intersection with the fossa is only 200 m. Both protrusions in Fig. 42 are surrounded by a terraced surface (orange in Fig. 42) that exhibits similar characteristics, differing only in scale and degree of complexity.

We identify at least four terraced surfaces adjacent to the protrusion in Fig. 43, labeled W, X, Y, and Z. These terraces appear analogous to those observed along the Terraced Depression Fossa (Fig. 33). Surface W sits at the topographically and stratigraphically highest level, while surface Z is a dune-covered ramp that extends from the floor of the fossa up along the protrusion. Between surface Z and surface X are numerous mechanically resistant stratigraphic layers that are all crosscut by surface Z. The edges of surface X and surface Y are jagged and lack fractures along the edges of their near-vertical escarpments. A ~25 m wide elongate ridge rises above surface Z along the floor of the fossa (box 1 in Fig. 43), a rare occurrence within the Cerberus Fossae.

The larger, southward-directed channel-like protrusion in Fig. 42 is sinuous along its 2.8 km length. As with the northward protrusion, a series of terraced surfaces (W, X, Y, and Z) make up the boundaries of the protrusion (Fig. 44). Surface W is topographically highest, followed by X, Y, and then Z, which acts as the fossa floor but crosscuts and merges with surface Y. The jagged outline of each surface (especially surface X) is near-vertical and likely experienced mass wasting, contributing to the retreat of the surfaces. Fractures are not present along the edges of the terrace cliffs, implying a predominantly geomorphic, not structural, mechanism for cliff development. Surface Y encloses an isolated pinnacle (Fig. 44), which has been progressively eroded by mass wasting, evidenced by boulders scattered around its base.

Similar terraces (X, Y, and Z) are observed along the walls of the valley-like protrusion further away from the fossa (Fig. 45). Surface Z is the same surface as in Fig. 44

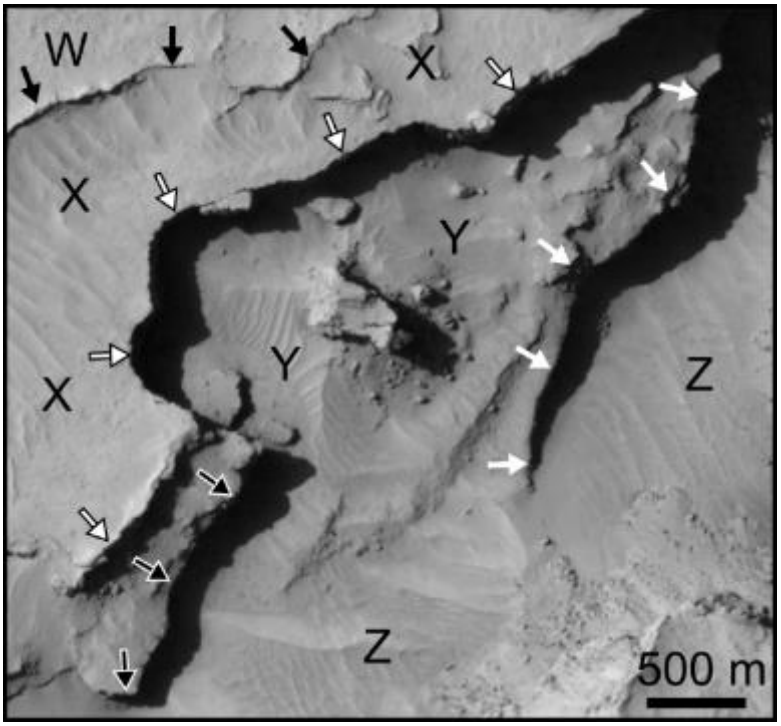

Figure 44. HiRISE image ESP_025710_1885 (25 cm/pixel; north is up; see Fig. 42 for context) showing terraces that are at different elevations. The amount of relief appears to be greatest between surfaces Y and Z (white arrows) and least between W and X (black arrows). More than two terraces step down from surfaces X to Y (black and white outlined arrows). Surface Y contains tall standing pinnacle with boulders at the base of its eastern side. The pinnacle is likely a remnant of surface X.

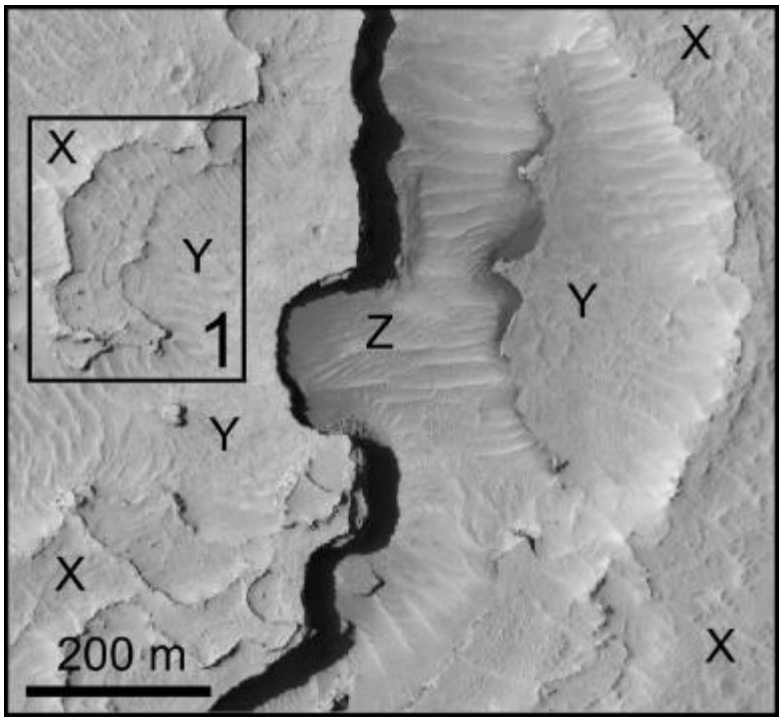

Figure 45. HiRISE image ESP_025710_1885 (25 cm/pixel; north is up; see Fig. 42 for context) showing terraced surfaces at three different elevations (X, Y, and Z). These surfaces do not correspond directly with those in Figs. 43 and 44. Channel Z incises into all other surfaces. The irregular, vertical escarpments between each terrace lack any obvious fractures. Box 1 shows a series of resistant layers that gradually stepping down in elevation from surface X to surface Y.

and crosscuts surface Y. The near-vertical boundary between these surfaces is irregular, displaying cuspate and scalloped indentations. A series of resistant, parallel stratigraphic layers are exposed between surfaces X and Y (box 1 in Fig. 45), forming a series of steps that define the downward progression in elevation from X to Y.

6.2.2.2. Interpretations

The Orthogonal Protrusion Fossa exhibits surface features adjacent to the fossa that could have been formed as a result of groundwater seepage. Trough-like protrusions oriented orthogonally to the fossa crosscut lobate deposits that were apparently sourced from the fossa (Fig. 41) and which have polygonal surfaces, lobate flow fronts, and channels consistent with lava flows (Figs. 39-41). Some of the protrusions form continuous, dune-covered surfaces that ramp upward from the floor of the fossa (Fig. 41 and 42). We interpret that groundwater sapping occurred to variable degrees, eroding into the rock surrounding the fissure to a distance of between 100 m and ~3 km.

In a similar manner to the surfaces on the Terraced Depression Fossa, multiple inset terraces step lower in elevation toward the fossa interior. We interpret surface Z to crosscut surfaces Y and X (Fig. 43). Since surface Z is continuous with the floor of the fossa and crosscuts the fossa wall, we infer that surface Z formed either during or after fossa formation. The multiple terrace edges in Fig. 43 show that a similar process that created ramp Z may have also created surface Y, allowing it to incise into surface X, and allowing surface X to incise into surface W. The boundary of each surface has a similar character, with near-vertical scarps, and an irregular and curvilinear boundary that we interpret to be formed as a result of a subsurface fluid flow controlled by topography (Fig. 43). The boundaries of each surface do not appear fractured on their surfaces and lack identifiable lava coating textures. As with the other orthogonal protrusions, the creation of these terraced surfaces is consistent with being the result of groundwater seepage. In this scenario, we hypothesize that residual

heat from the magmatic dike that created the associated fossa mobilized water to create a depression that grew outwards, away from the fossa.

The sinuous trough located south of the fossa (blue in Fig. 42) physically connects with the base of the fossa (similar to the connection of surface Z to the fossa floor in Fig. 43). The near-vertical and scalloped nature of the edge of the trough does not resemble the more continuous boundaries produced by aqueous channels (Burr et al., 2002a,b), lahars (Pedersen, 2013), or lava channels (e.g., Leverington, 2011). Instead, we propose that the protrusion also developed as a result of groundwater seepage. In this scenario, water eroding the rocks adjacent to the fossa flowed towards the fossa interior, rather than away, producing a channel surface that has a greatest depth at its intersection with the fossa, and with a higher elevation at its southern end. The orange unit in Fig. 42 demonstrates that the protrusion incised a surface that has a cuspate morphology and resistant layers have crown-like fractures that step progressively lower in elevation towards surface Z in Fig. 45. Surfaces X and Y reflects seepage and erosion from different stratigraphic levels that resulted in a tiered set of surfaces.

6.3. Category 3: Fossae flanked by channel-carved valleys

Valleys and channel-like forms associated with the Cerberus Fossae have been identified in two locations, and here we report on their morphologies, morphometries, topographic signature, and provide evidence supportive of a fluid-flow hypothesis for their formation. We describe a feature we refer to as Valleys in the Hesperian and Noachian transition unit and the Crater Fossa. While the Crater Fossa is associated with a Cerberus fossa, the Valleys in the Hesperian and Noachian transition unit show no apparent fossa source. Descriptions include a topographic analysis and geomorphic assessments to ascertain the volcanic, tectonic, and fluvial history of the landforms.

6.3.1. Valleys in the Hesperian-Noachian transition unit

6.3.1.1. Observations

Geomorphic modification of older geologic units cut by the Cerberus Fossae is not necessarily restricted to the immediate vicinity of the fossae themselves. One such example is series of valleys between 1-10 km south of the Orthogonal Protrusion Fossa, within the Hesperian-Noachian transition unit (HNt in Tanaka et al., 2014) centered at 8.352° N, 159.237° E (Fig. 46). The site is not spatially associated with the WNW-ESE oriented fossa. Instead, its extent is controlled by an approximately N-S trending feature, including a prominent elongate pit (labeled P in Fig. 46B) that appears to have played a role in mobilizing large quantities of HNt material through a series of channels with slopes that range from 2.6° to 3.4°. The channels (pink in Fig. 46B) crosscut unit md (the HNt unit of Tanaka et al., 2014) and are directed downslope toward the west. A total of seven channels emanate from the higher portion of the slope. The channels are consistently ~2 km in length, but vary in their widths from 125 m to ~650 m, with individual channels expressing a range of widths along their courses.

Toporaphic profiles drawn parallel to the approximately N-S trending feature within the HNt unit and adjacent lava plain to the west show a maximum relief of up to 130 m from their sources along D-D' down to the lowest elevation surface that profile A-A' crosses (Figs. 46 and 47). The topographically highest point occurs at the N-S oriented elliptical pit (P in Fig. 46B and enlarged in Fig. 48). Surface elevations decrease in every direction away from the pit. The pit has dimensions of 560 m by 300 m forms a bowl-shaped depression. The western side of the pit shows three parallel, narrow channels (black box in Fig. 48 with arrows indicating flow away from the pit). The boundary of the elliptical pit is either missing or obscured by dunes on its northern side, possibily indicating that a fluid breached the boundary and flowed northward, down the ~2.4° slope.

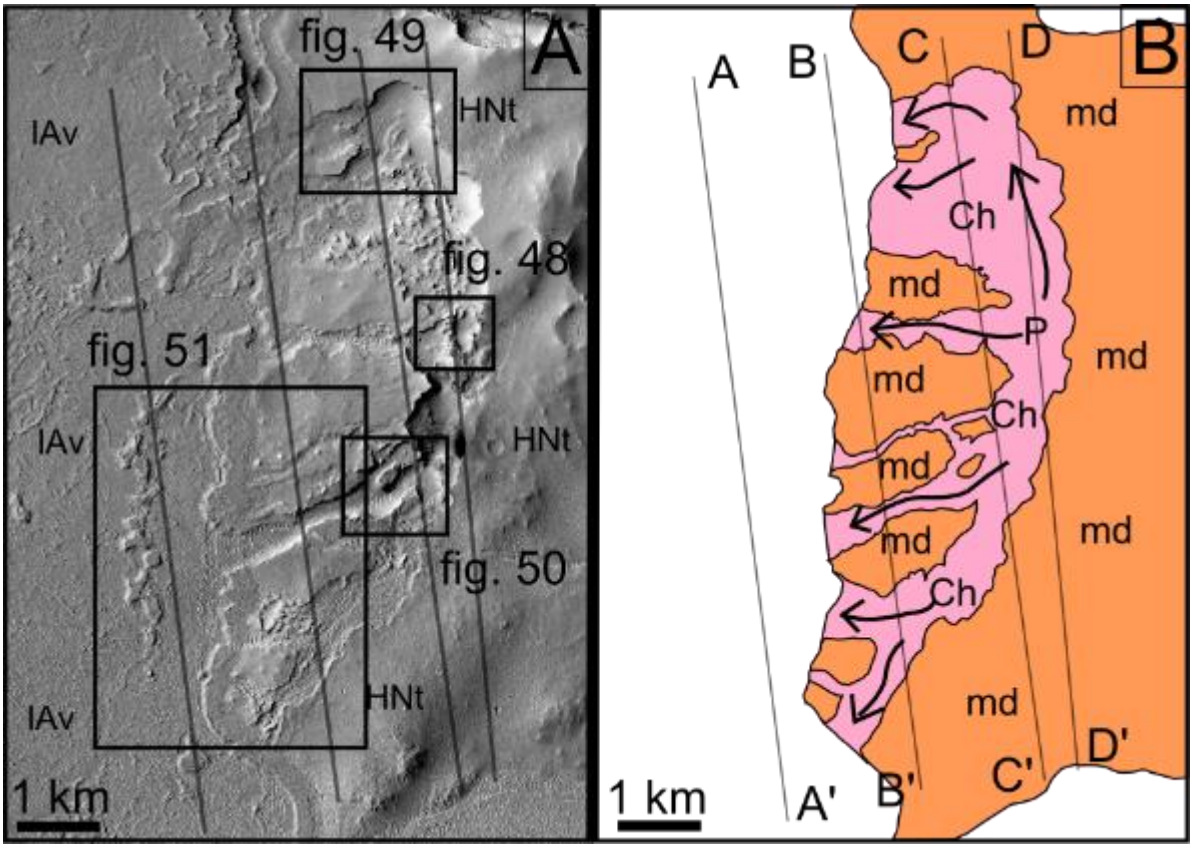

Figure 46. (A) CTX image G19_025710_1884_XN_08N200W (5 m/pixel; north is up; see Fig. 34 for context) with center point 8.352° N, 159.237° E. (B) Simplified geological map. Pink is a channelled surface (Ch) and orange is the mound-like surface (md) mapped as the Hesperian-Noachian transition unit (HNt) by Tanaka et al. (2014). Topographic data corresponding to profiles A-A', B-B', C-C', and D-D' are shown in Fig. 47.

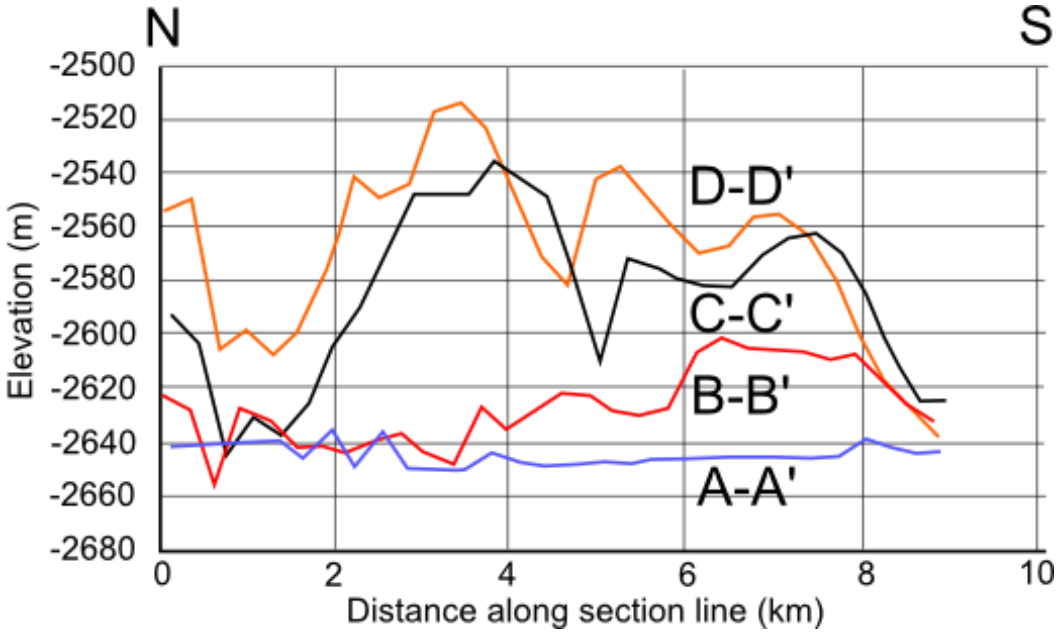

Figure 47. Profile lines extracted from MOLA PEDR data along the Hesperian-Noachian transition unit boundary with the adjacent lava plains, south of the Orthogonal Protrusion Fossa (see Fig. 46 for location of profile lines). There is a maximum relief of ~130 meters along the channels, from the top of D-D' to the bottom of A-A'. Profile lines and corresponding MOLA orbits are as follows: A-A' (orbit: 14590); B-B' (orbit: 14917); C-C' (orbit: 16904); and D-D' (orbit 19732).

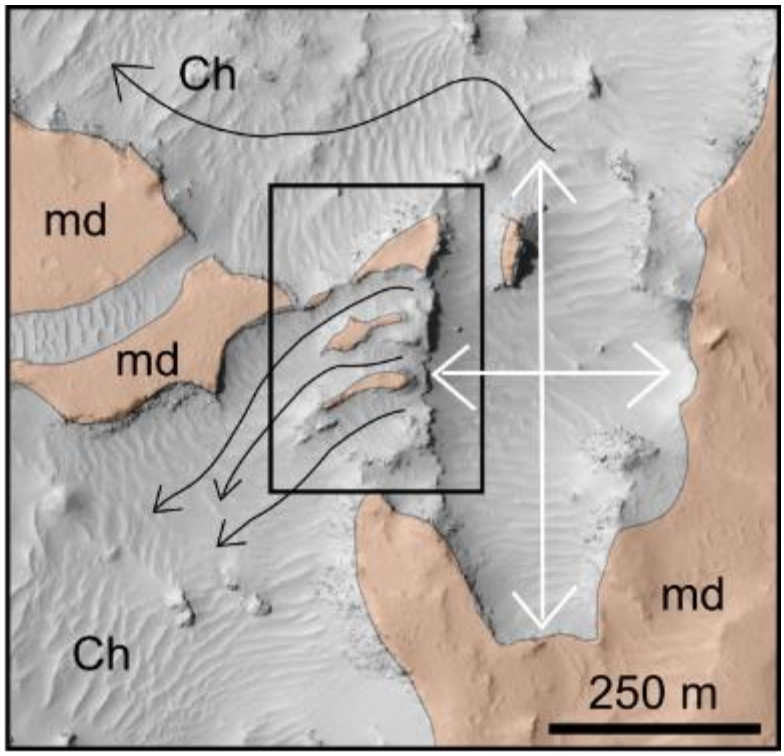

Figure 48. HiRISE image ESP_025710_1885 (25 cm/pixel; north is up; see Fig. 46 for context) showing the long and short axes (white arrows) of the elliptical pit that appears to have sourced channels (Ch) that lead away from it. Black arrows indicate inferred flow directions based on slopes. Surface md represents the Hesperian-Noachian unit (HNt) mapped by Tanaka et al. (2014).

Approximately 2.6 km north of the pit, the channeled surface (pink unit in Fig. 46B) is characterized by mounds and angular, blocky material that produce topographic variability across the surface (Fig. 49). The channeled surface has an abrupt boundary with the md unit (steep scarps indicated by black arrows in Fig. 49) from which material appears to have been shed onto the channel surface. This boundary is heavily scalloped and has a relief of up to 43 m above the channel floor (box 1 in Fig. 49). An isolated mesa of unit md surrounded by the channeled surface (box 2 in Fig. 49) is elongate in a direction parallel to the downslope direction within the channel, potentially reflecting bifurcation of a flowing material around the resistant obstacle (long black arrows in Fig. 49).

Another example of an isolated, elongate mesa within a bifurcating channel is shown in Fig. 50. The downslope end of this channel appears to crosscut a surface layer (ccd in Fig. 51) that was deposited along the edge of the md unit (i.e., along the edge of the volcanic plains to the west of the Hesperian-Noachian transition unit in Fig. 46). Unit ccd is ~500 m wide and appears to have a steep, abrupt boundary with unit ssm along its western edge (Fig. 51). Unit ccd noticeably embays the other channels where they exit onto the lava plains, indicating that these channels were not active after the deposition of unit ccd (i.e., only one channel in Fig. 51 postdated and crosscut unit ccd). The morphology and topography of these surfaces suggest that material flowed down the youngest channel and onto surface ssm, further eroding unit ccd. The surfaces of the Ch and ssm units appear texturally muted and dust covered (Fig. 51) revealing little to none of the original textural characteristics of unit ssm.

6.3.1.2. Interpretations

The erosion of the Hesperian-Noachian transition unit (Hnt) by channels (Fig. 46) indicates that the Cerberus Fossae magmatic system affected beyond the immediate vicinity of the deep fossae themselves. The cuspate and alcove-like depressions along the eastern

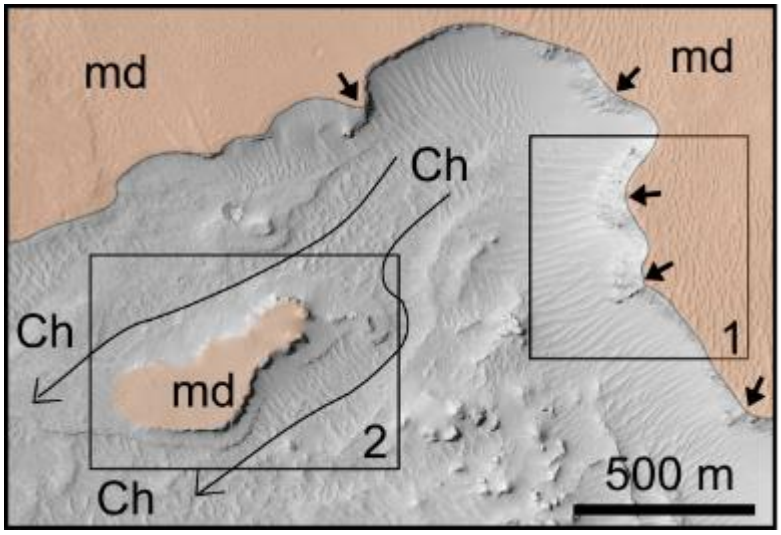

Figure 49. HiRISE image ESP_025710_1885 (25 cm/pixel; north is up; see Fig. 46 for context). In box 1, black arrows point to a break in slope that is scalloped with resistant upper layers and a dust coated lower surface. Box 2 shows a high-standing, resistant obstacle around which flow of material may have occurred. Surfaces labelled md correspond to the HNt unit mapped by Tanaka et al. (2014) and the unit Ch is the channeled surface.

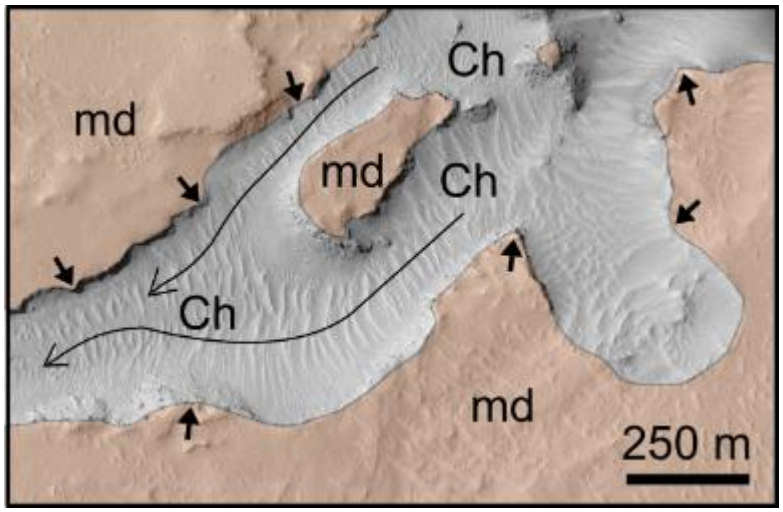

Figure 50. HiRISE image ESP_025710_1885 (25 cm/pixel; north is up; see Fig. 46 for context). Channel edges (short black arrows) appear angular and jagged. Longer arrows indicate the downslope inferred flow direction. Two channels appear to merge after passing around an elongate island of md that separates two valleys.

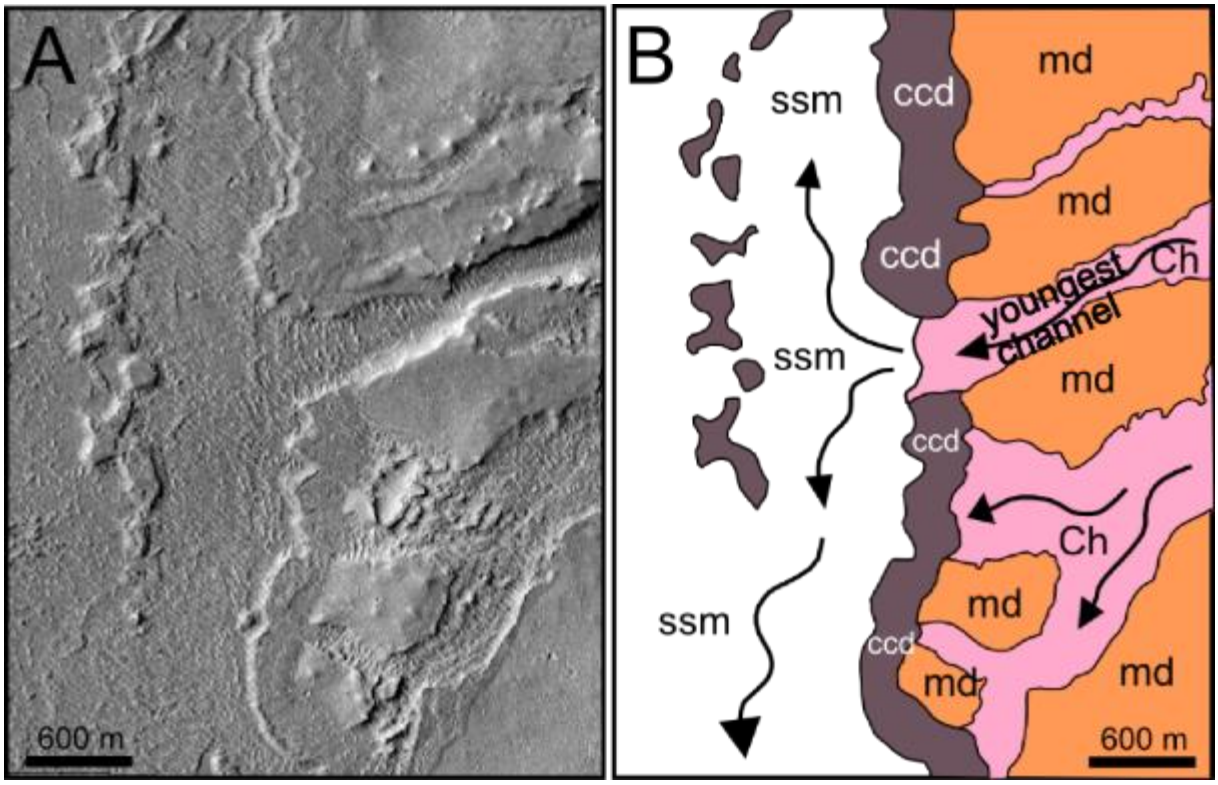

Figure 51. (A) CTX image G19_025710_1884_XN_08N200W (5 m/pixel; north is up; see Fig. 46 for context). (B) Simplified geologic map of (A) showing relationships between units Ch, md, ccd, and ssm. The channel labelled “youngest channel” appears to have been the most recently formed channel and crosscuts unit ccd. Topographic data indicate that surface ssm is relatively flat (see profile A-A’ in Fig. 44).

side of the depression (pink unit Ch in Fig. 46) and their association with collapsed blocks of irregular size and shape are somewhat consistent with the formation mechanisms that lead to chaos terrain. The presence of channelized forms within the HNt may indicate that water played a role in their formation. At the site, up to seven channels are identified that each have a downslope direction to the east, some of which show elongate, potentially eroded, resistant barriers around which a fluid flowed. The highly scalloped boundaries along each of the channels that contributes to the great variation in their width is likely caused by the collapse of loose debris from the HNt unit.

The erosive channels appear to trace back to an elongate, N-S trending pit that exhibits resistant ridges on its western side around which fluid may have flowed (Fig. 48). These ridges are angular and depart from the more rounded nature of streamlined erosional landforms that characterize outflow channels (e.g., Burr et al., 2002a, b). The elliptical pit is similar in morphology to pits that lie upstream of channels and their associated deposits that flowed away from a wrinkle ridge near the Cerberus Fossae, as identified by Thomas (2012). The elliptical nature of the pit is also similar to volcanic vents identified in the Cerberus Fossae region (Hauber et al., 2009; Keszthelyi et al., 2008). Therefore, we infer a magmatic/volcanic origin for the pit in Fig. 45, despite an absence of characteristic lava textures and landforms, such as digitate flow margins, platy-ridged textures, pahoehoe, or a'a (Keszthelyi et al., 2004).

Based on the morphology of the channels that emanated from the pit location at the topographically highest point, combined with their erosive capability, the channels themselves likely do not reflect a volcanic process. The characteristic morphology of the channels is not sinuous at low amplitudes like most lava channels identified on Mars (e.g., Leverington, 2011). Therefore, we propose that the elliptical pit is the result of magmatic intrusion into a loose regolith that contained ground ice that subsequently melted, producing sediment-water flows that carved the numerous channels. The HNt unit is composed of

impact ejecta and loose debris (Tanaka et al., 2014) that could have been incorporated into a flowing aqueous fluid, readily producing a mass. Collapse of the pit may have resulted from fracturing of the surface layers in response to magmatic intrusion below. The intrusion process destabilized the HNt deposits, resulting in the steep, scalloped character of the eastern margin of the boundary between units Ch and md in Fig. 46. Collapse along the walls of the channels provided additional input of loose debris into the aqueous flow that was subsequently deposited downstream onto surface ssm (Fig. 51).

Crosscutting relationships in Fig. 51B demonstrate that there were multiple stages of channel formation and deposition. Most of the channels abruptly terminate at unit ccd, which was thus deposited after the channels formed. However, one of the channels crosscuts unit ccd and appears to have deposited surface ssm, which lacks textural complexity or any obvious lava flow characteristics (possibly the result of dust cover). Based on the topography of surface ssm (Fig. 47), the sediment-water mixture likely flowed to the north along the western boundary of unit ccd (Fig. 51). The abrupt western edge of ccd, combined with the flat bench-like nature of the ccd surface where it abuts the Hesperian-Noachian transition unit (HNt or md) strongly suggests that ccd is the remnant of an inflated sheet lava flow that deflated and collapsed along the steep, western edge of ccd. This lava flow can be traced back to the fossa to the north, implying that it erupted from the Cerberus Fossae. The collapse of the inflated lava flow created a depression into which the youngest channel in Fig. 51 could deposit material. The combination of crosscutting relationships indicate that the ccd lavas were erupting from the Cerberus Fossae after some of the Ch channels in the HNt unit developed (Fig. 51), blocking their downslope ends. At least one channel continued to be active after the emplacement of the ccd lava. Hence, the magmatic activity at the elliptical pit at the source location of the channels broadly overlaps in time with the intrusion of magma along the Cerberus Fossae. The geomorphic modification of HNt out to distances of ~10 km from the fossae is thus likely to be related to the same magmatic event, implying that

interactions between magma and ground ice were not restricted to the immediate vicinity of the fossae themselves. In the case of the region shown in Fig. 46, an isolated intrusion of magma occurred ~4 km south of the fossa along a N-S trend, perhaps indicating less control of regional stresses on intrusion mechanics within the poorly consolidated HNt unit. Similar irregularities in dike geometries have been noted within poorly consolidated hyaloclastic ridges along the plate boundary in southwest Iceland (personal communication, Simon Kattenhorn, 2015).

6.3.2. Crater Fossa

6.3.2.1. Observations

The name Crater Fossa is applied to a relatively small (~50 km long, 550 m wide) fossa at the southern extent of the Cerberus Fossae (Figs. 2 and 3) that crosscuts the southeastern corner of an impact crater (Fig. 52; center point 7.095° N, 161.803° E). The fossa is comprised of two fossa segments that are 5 km and 7 km long, respectively, with approximately the same width (~550 m). Each fossa segment has a circular pit at one of its ends (with diameters of 285 m and 360 m, respectively) that are approximately half as wide as the neighboring fossa. In general, the Crater Fossa has similar geometric characteristics to other Cerberus fossae. The interior of the fossa has near-vertical walls and talus slopes composed of fine-grained material atop which boulders that calved off of fossa walls reside (see Fig. 20 for a similar example).

Lobate flow deposits are visible adjacent to, and associated with, the Crater Fossa. In one example, a flow that appears to have emanated from a circular pit flowed to the north (black arrows in Fig. 53). The flow has lobate margins and a constructional appearance, although a lack of topographic data over this flow hinders accurate flow height calculation. Another example of a deposit adjacent to the fossa is shown in box 1 of Fig. 53.

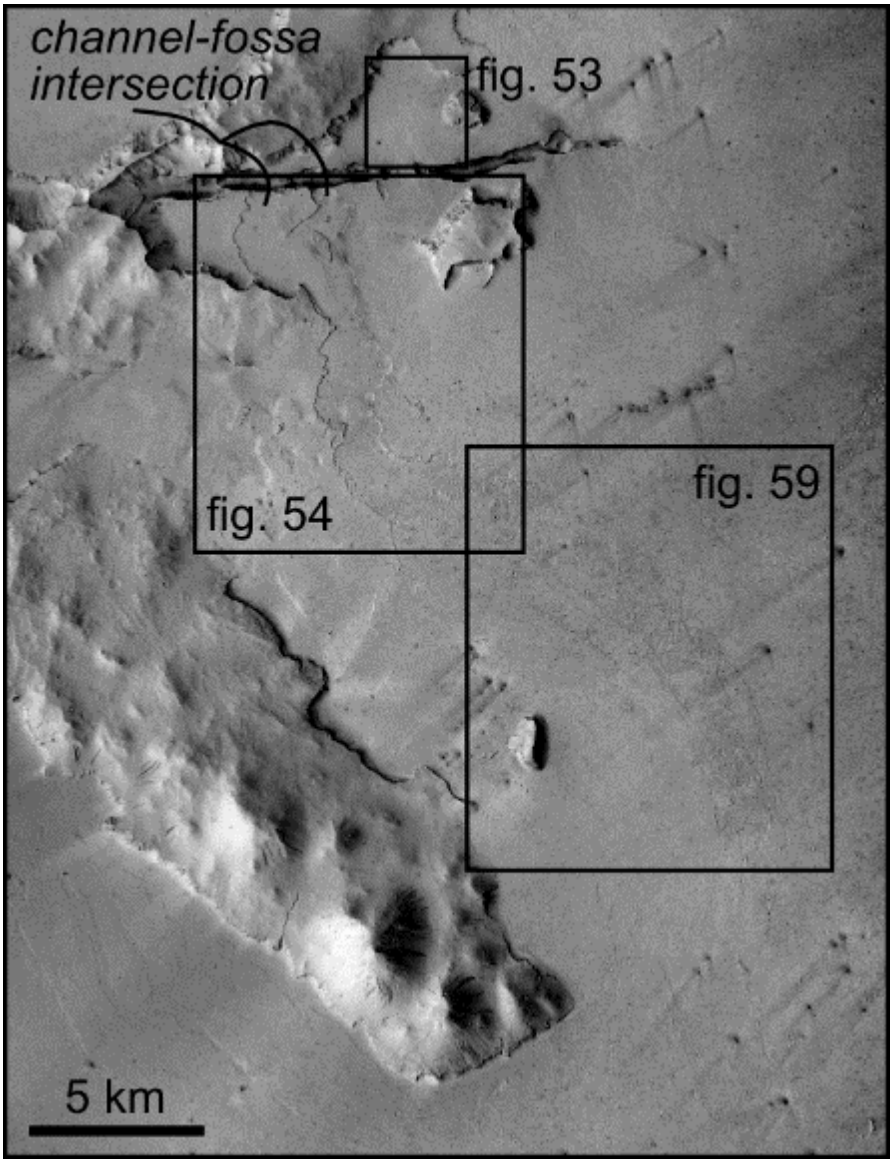

Figure 52. CTX image G14_023600_1871_XN_07N198W (5 m/pixel; north is up; see Fig. 5 for context; centered at 6.942° N, 161.838° E) shows the eastern end of the ~50 km long Crater Fossa where it cuts through the southeastern edge of a crater margin. The intersection of a prominent channel with the fossa is indicated along its southern margin. Portions of the channel are indicated with boxes for Figs. 54 and 59. The box for Fig. 50 marks the location of a lobate flow deposit north of the fossa.

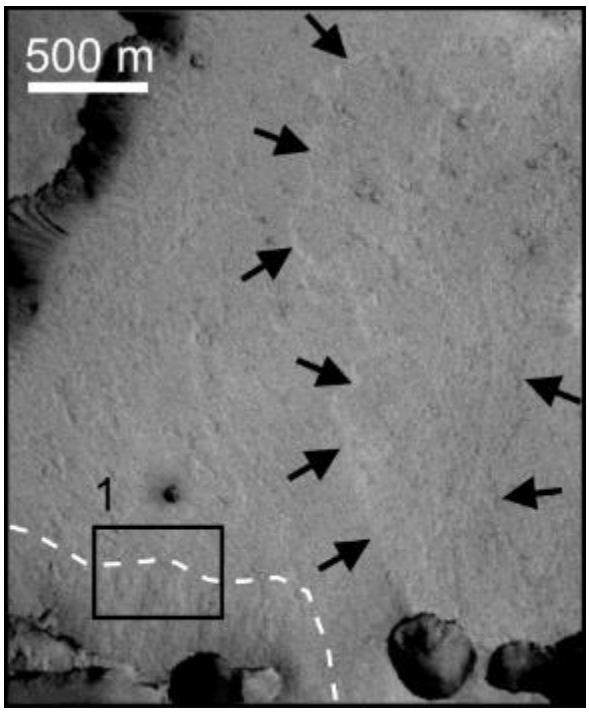

Figure 53. CTX image G14_023600_1871_XN_07N198W (5 m/pixel; north is up; see Fig. 52 for context) shows lobate flows (black arrows) that extend northward away from a pit along the Crater Fossa, and a subtle ridged deposit adjacent to the fossa walls (outlined in white). The surface texture varies across the area of box 1; south of the white line is a ridged deposit, whereas north of the dashed line is a smooth deposit.

The surface texture south of the white dashed line shows alternating high and low albedo bands related to low ridges oriented N-S in the image, perpendicular to the fossa walls out to a distance of ~500 m from the fossa. In contrast, the area north of the white dashed line lacks ridges and appears to be a smooth flow that embayed the ridged unit along the edge of the fossa. The ridged deposits appear constructional and create a topographic ramp leading up toward a ~15 m high ridge that is present along both edges of the fossa, verified by MOLA PEDR data, similar to examples described previously (Figs. 7, 17, 30, and 37).

The most prominent geomorphic feature associated with the Crater Fossa is a channel-like form that abuts the eastern end of the fossa and extends south and then east for ~24 km (Figs. 52 and 54). The feature is distinctly bimodal in its geomorphic texture, exhibiting a transition in morphological expression at a distance of ~10.7 km south of the channel-fossa intersection from a smooth, texturally muted surface with a high surface albedo and cuspate erosional scarp boundaries (Fig. 51) to a depositional surface that has a large variability in surface albedo and which defines patchy zones of rough material (Fig. 56).

Topographic profiles (Fig. 52) were extracted from a CTX DTM covering the erosional portion of channel-like feature. The channel intersects the fossa at two locations and appears to bifurcate around a mesa that has is angular in planview, tapered toward its southern tip, and which appears as a topographic high between the two channel surfaces labeled Ch in Profile A-A' (Fig. 52). The term "bifurcate" is here used to refer to the bidirectional nature of the channel-like form and does not necessarily imply a directionality of fluid flow.

The topographic profiles also reveal the presence of two levee-like ridges (labeled R in Fig. 55) that form topographic highs that follow the north-south length of the boundary between the pink and white surfaces in Fig. 54B. In profile A-A' the ridge has a maximum relief of ~20 m. The lowest channel elevation (-3400 m) and maximum channel depth (60 m) occurs in the valley that occurs at a distance of ~2.5 km along section line A-A'; however, this deepening of the channel appears to reflect a superposed erosional effect close to the

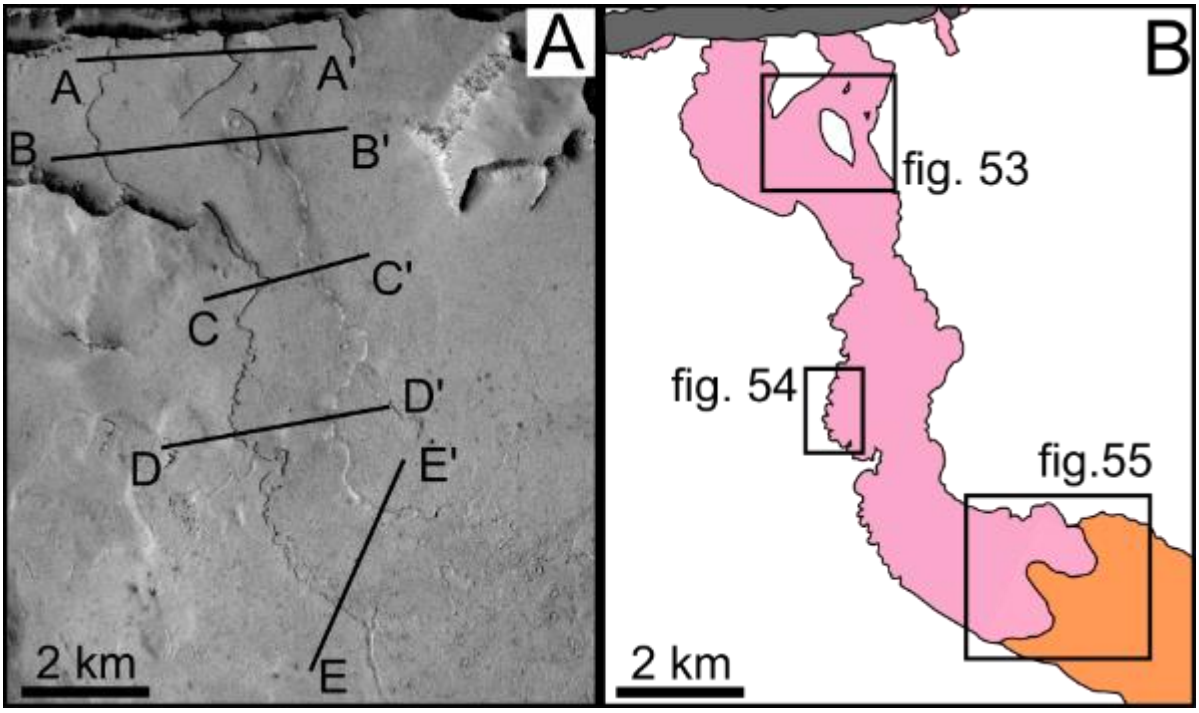

Figure 54. (A) CTX image G14_023600_1871_XN_07N198W (5 m/pixel; north is up; see Fig. 52 for context) with profile lines A-A', B-B', C-C', D-D' and E-E' as shown in Fig. 55. (B) Simplified geologic map of (A) showing the fissure in dark grey, the channel-like form in pink, a depositional unit beyond the morphological transition in orange, and the surrounding surface in white. Locations of detailed images shown by black boxes.

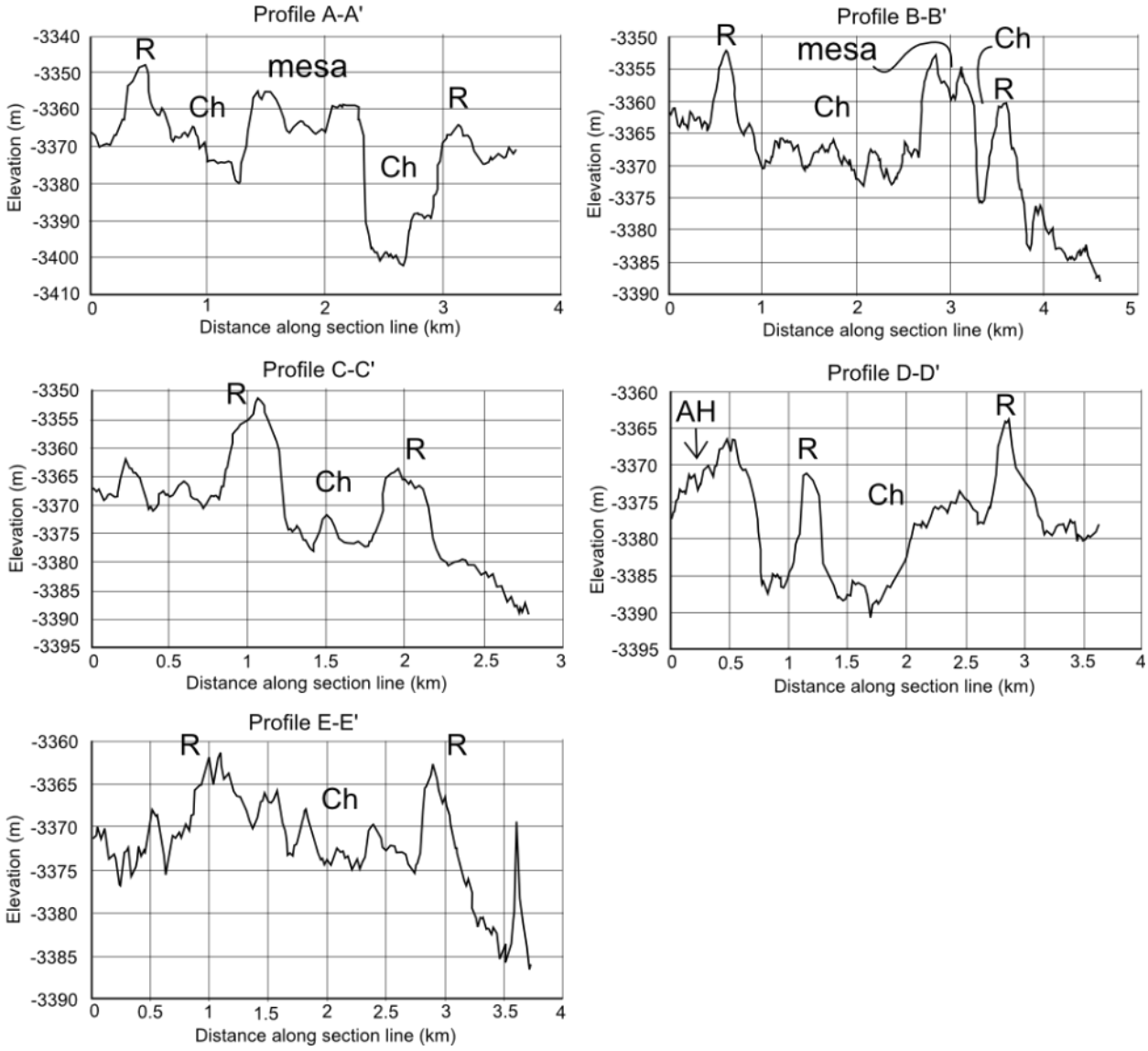

Figure 55. Topographic data extracted from a CTX DTM (courtesy of Devon Burr) created for this portion of the Crater Fossa. Profiles A-A, B-B', C-C', D-D', and E-E' correspond to section lines in Fig. 54. Ridges are present along the edges of the channel (~10-20 m high) in each of the profiles and are indicated by the letter R. The channel surface, as mapped in Fig. 54B, is indicated by Ch. Profiles A-A' and B-B' both include topographic highs (labeled mesas; see Fig. 54) separating two branches of a channel. An anomalous ~20 m high occurs along the western (left) side of profile D-D' (labelled AH), which can be correlated in regional images to a natural variation in the surface elevation of the surrounding lava plains.

fossa edge, similar to that observed along other fossa described in this study. The adjacent channel in profile A-A' is only 30 m deep and stands ~20 m higher than the 60-m-deep channel.

At the location of profile B-B', 1.45 km south of profile A-A', the two channels present in A-A' have converged and then again bifurcated around a streamlined form (labeled mesa along B-B' in Fig. 55 and enlarged in Fig. 56). Topographic data along profile B-B' reveal two topographic lows (channels) bounded by ridges on both sides (labeled R) that exhibit heights of between 12 and 15 m relative the channel floor. Although the channel and adjacent topographic highs in B-B' appear to be superposed on a regional slope from west to east, the gradual decrease in regional elevation is only ~25 m over a distance of 4.6 km, implying a regional slope of only 0.3° upon which the channels have been superposed, likely representing the topographic variability of the surrounding lava plains.

In plan view, the edges of the channel where intersected by profile B-B' are defined by jagged scarps (black arrows in Fig. 56) that lack fractures along their edges. The high-standing channel inliers (mesas) also have abrupt, vertical edges. The largest of these mesas (1 km by 0.4 km; double-headed arrows in Fig. 56) has a streamlined form with the long axis oriented NW-SE. The morphometry of the feature is similar to those described by Burr et al. (2002a, b), which have a rounded "upstream" end that tapers downstream. The two smaller inliers on the channel floor (200 m by 40 m; boxes 1 and 2 in Fig. 56) also stand higher than the surrounding surface. They are elongate in the N-S direction and are angular in plan view with near-vertical scarps bounding their flat surfaces.

The scarps that form the edges of the channel are near-vertical to overhanging. The oblique look angle of the HiRISE observation shows that a resistant carapace of rock overlies finer grained material that preferentially eroded and promoted undercutting. The scarp boundary of the channel also displays increasing roughness with increasing distance from the fossa along the length of the channel (Fig. 54). This increasing irregularity is caused by

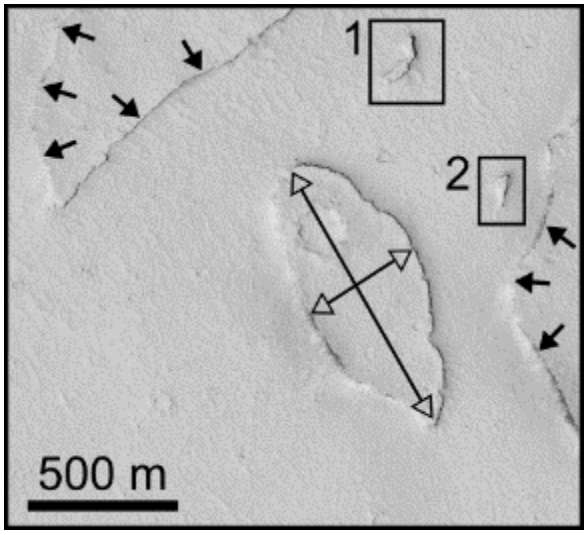

Figure 56. HiRISE image ESP_023310_1870 (25 cm/pixel; north is up; see Fig. 54B for context) shows mesa-like topographic highs that form inliers on the channel floor. The larger streamlined form in the center of the image has a long axis oriented NW-SE (double-headed arrows). Smaller inliers identified by boxes 1 and 2 appear to have upper surfaces at about the same elevation as the larger mesa and have similar near-vertical scarps along their edges. Small black arrows point to the jagged boundaries of the channel.

the presence of multiple cuspate erosional alcoves along the channel margins with increasing distance from the fossa (e.g., compare Figs. 56 and 57). These cuspate indentations along the channel boundary (arrows in Fig. 57) are 100-200 m long and are consistently concave toward the channel.

Profiles C-C', D-D', and E-E' (Figs. 54 and 55) continue to show a levee-like ridge along the margins of the channel. This ridge is consistently 10-20 m high and bounds the channel floor as it drops ~20 m in elevation between profiles B-B' and D-D' (-3370 m to -3390 m over a distance of ~4.6 km, giving a channel slope of 0.25°). The channel floor increases ~15 m in elevation between D-D' and E-E' (-3390 m to -3375 m), coinciding with a change in the morphological character of the channel surface (Figs. 54 and 58).

The morphology of the channel surface, is in general, texturally muted and lacks platy and roughened textures characteristic of lava flows (e.g., Keszthelyi et al., 2004, 2008). Closer to the morphologic transition of the channel, however, at a distance of ~10.7 km from the fossa, the surface has subtle lineations oriented approximately transverse to the channel boundaries (Fig. 58). The black dashed line in Fig. 58 encloses the texturally variable channel surface, which contrasts with the adjacent surface with smoother albedo variations that appears to have topographic undulations caused by the presence of impact craters and small, infrequently spaced ridges.

Extending farther south and east of the morphological transition in Fig. 58, the channel form changes to a positive topographic surface with a flow-like geometry (partially delineated by the dashed lines in Fig. 59) that exhibits a rough surface texture that is disrupted and patchy, contrasting greatly with the channel form from which it is seemingly derived. Topographic profiles drawn transversely across the flow demonstrate that it is constructional, with a flow height of 10 to 15 meters (i.e., similar to the increase in channel height between profiles D-D' and E-E'). The regional topography in the vicinity of the flow in Fig. 59 has slopes that are greatest towards the SSE (i.e., in the direction of the long axis of

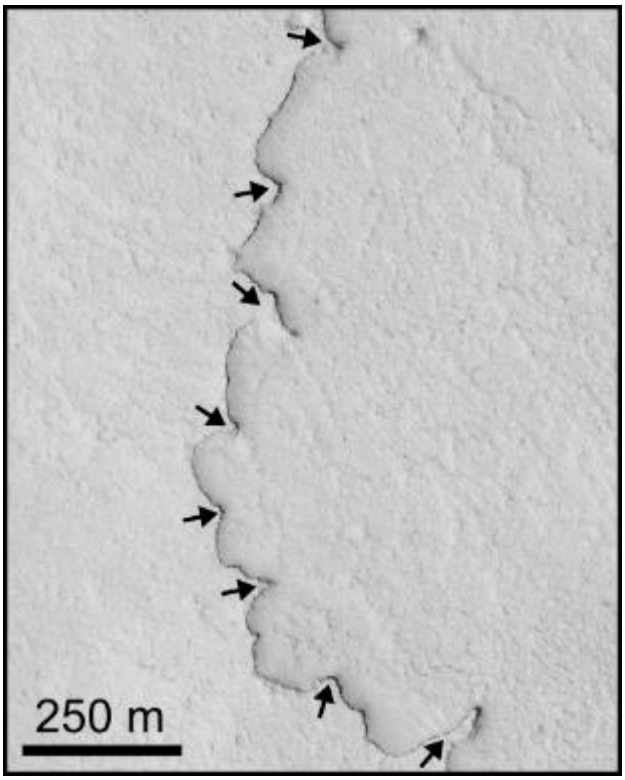

Figure 57. HiRISE image ESP_023310_1870 (25 cm/pixel; north is up; see Fig. 54B for context) showing cusps that define the scalloped boundary of the channel (black arrows). Profile D-D' (Fig. 55) crosses the region shown in this image and reveals a 15 m high ridge along the cuspate boundary.

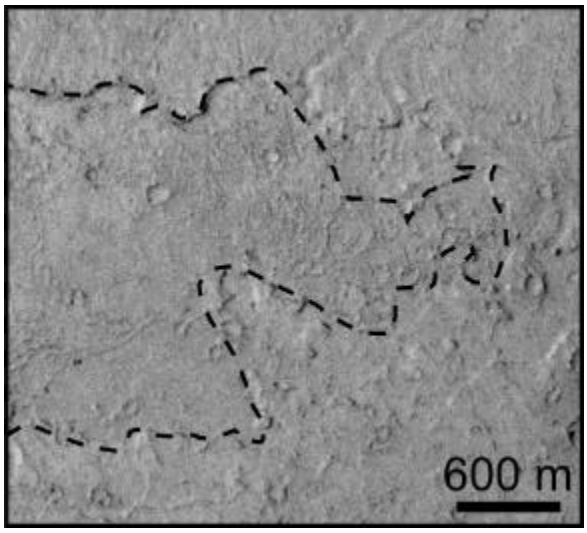

Figure 58. CTX image G14_023600_1871_XN_07N198W (5 m/pixel; north is up; see Fig. 54B for context) showing the southwestern boundary of the channel-like form in Fig. 54. The termination of the channel is outlined by the dashed line. Small, closely-spaced ridges on the interior of the dashed polygon are oriented transverse to the channel axis and differentiate the channel from the adjacent surface materials, which appear texturally smoother with undulations caused by impact craters and small, infrequently spaced ridges.

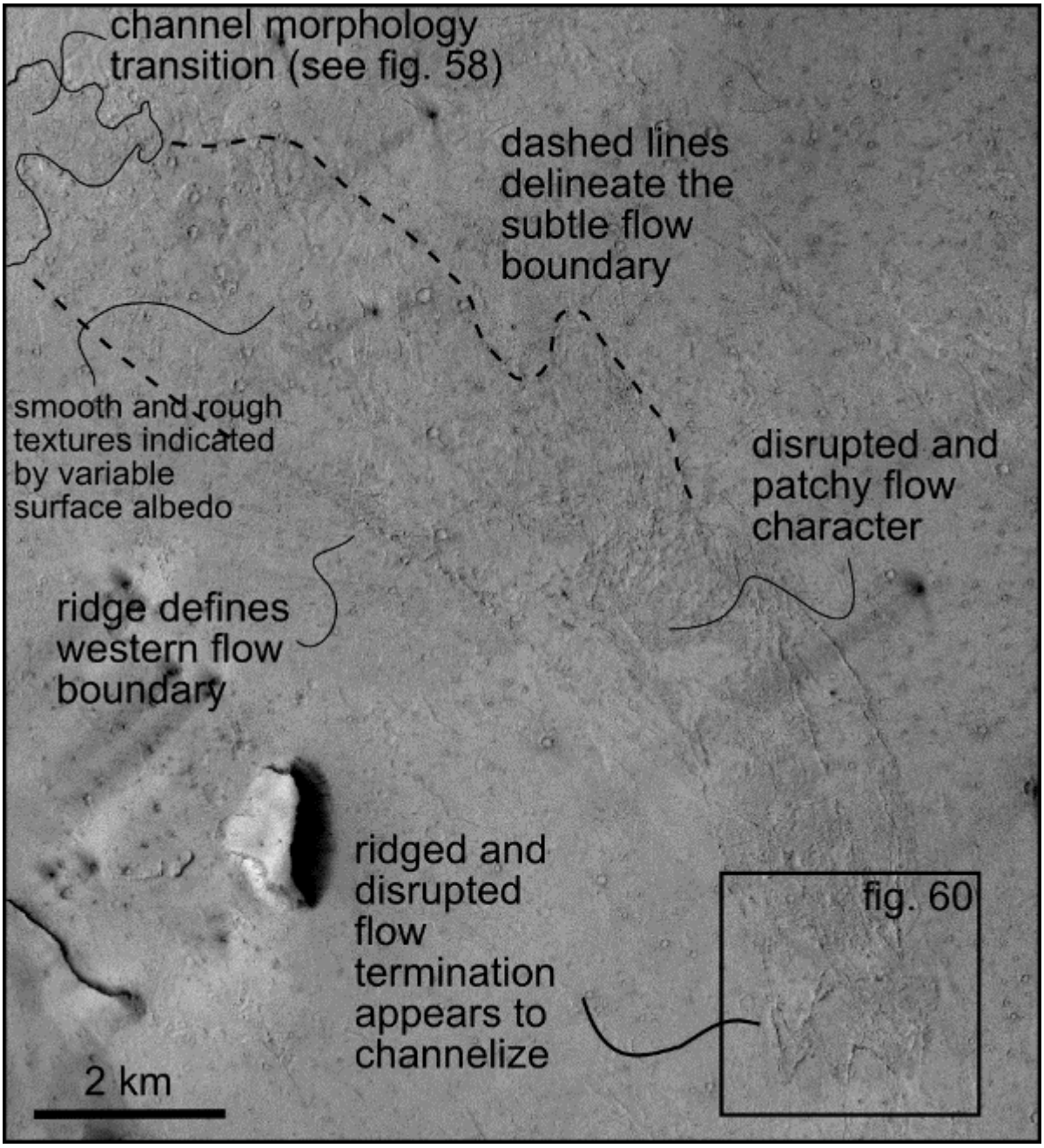

Figure 59. CTX image G14_023600_1871_XN_07N198W (5 m/pixel; north is up; see Fig. 52 for context) demonstrates a constructional deposit that is located downstream from the channel shown in Fig. 54. The deposit has a ridged and textured surface (between the black dashed lines, which outline a portion of the deposit), contrasting with the texturally smooth surrounding region. The deposit is elongate toward the SSE and splits into three distinctive lobes with sharp ends at its downstream end (box and Fig. 60).

the constructional flow feature), with a slope of the flow surface of 0.15° based on MOLA PEDR data (27 m elevation drop over 10.1 km length of the flow surface from NW flow character transition to the SE flow termination in Fig. 59).

The textures present at the end of the flow are characteristic of the majority of the flow surface (Figs. 59 and 60), with numerous low albedo ridges separated by high albedo patches, producing a disrupted appearance to the flow top. The flow has well-defined flow margins against the surrounding surface (dashed lines in Fig. 59) and splits into three separate lobes at its terminus (Fig. 60). These lobes have angular, chevron-like ends in plan view, dissimilar to both the rounded and lobate flow margins of the deposits north of the Crater Fossa (Fig. 53) as well as the digitate boundaries of the deposits along the Terraced Depression Fossa (Fig. 34).

6.3.2.2. Interpretations

The Crater Fossa resembles other fossae in this study in that it exhibits evidence of eruptive deposits along its margins. Lobate deposits sourced from a circular pit along the fossa extend 3 km northward (Fig. 53). Digitate boundaries along the lobate flow are similar to those observed on the flanks of low shields on Mars that are generally interpreted to have a basaltic lava composition (e.g., Jaeger et al., 2010; Hauber et al., 2009; Leverington, 2004; Richardson et al., 2013; Bleacher et al., 2007).

Thus, we interpret the flows that emanate from the circular pit to be effusive volcanism. Subsequent to the emplacement of the northward-directed lava flow, the pit formed as a result of collapse of the surface into a cavity created by retreating magma. Similar collapse mechanisms have been inferred for the formation of pit craters along fracture propagation paths on Kilauea, Hawaii (Okubo and Martel, 1998), which may represent a terrestrial analog for the processes that occurred at the Cerberus Fossae.

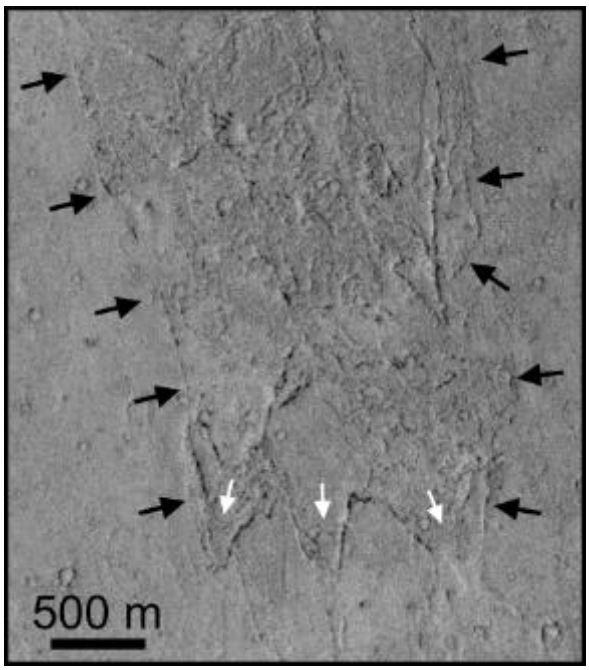

Figure 60. CTX image G14_023600_1871_XN_07N198W (5 m/pixel; north is up; see Fig. 59 for context) covering the termination of the rough-textured flow deposit associated with the channel system that emanates from the Crater Fossa. The boundary of the flow is demarcated by black arrows. White arrows indicate the inferred flow direction and the channelization of the flow into three distinct lobes with sharp downstream terminations.

The ridged deposit that flanks the fossa (box 1 in Fig. 53) has a relief of ~15 m and slopes away from the fossa wall, which crosscuts the ridge. We interpret these ridged deposits to have been constructed during the initial formation of the fossa during effusive eruptive processes along a fissure that formed the precursor to the fossa. The summit craters of volcanic vents on Mars are commonly attributed to formation by collapse above a dike or magmatic conduit whereby the emplacement of flows is followed by a pressure drop and magma retreat into its subsurface reservoir (e.g., Mège et al., 2003; Hauber et al., 2009). The fractures that facilitate the collapse above a magmatic conduit can manifest as normal faults (e.g., Hauber et al., 2009), or, more simply, result from collapse due to a heavily fractured zone above the dike tip associated with intrusion (e.g., Mastin and Pollard, 1988). Hence, as with other fossae in this study, we infer that the Crater Fossa resulted from collapse above a magmatic dike. Based on the presence of lava flows adjacent and to the north of the fossa, we also infer that the magmatic dike was able to reach the surface and erupt, after which the surface collapsed into a void caused by magma retreat.

The channel feature that extends south and east from the eastern portion of the Crater Fossa exhibits a range of characteristics along its ~24 km length (Fig. 52). From its intersection with the fossa, the channel appears to have incised into the substrate for a distance of 10.7 km (Fig. 54), at which point the morphology of the channel abruptly transitions into a constructional deposit (Fig. 59). Investigation of the first 10.7 km reveals that the channel may not have significantly incised into the preexisting regional surface, but was instead constructed onto this surface (Fig. 54 and 55) as a channelized flow that ultimately evacuated its channels and left behind flanking ridges or levees that had originally constrained the flow within the channel. Topographic profiles obtained from a CTX DTM demonstrate the presence of 10-20 m high ridges that slope away from the near-vertical scarps that face the interior of each side of the channel (Fig. 55). The elevation of the channel surface is not significantly different from the surrounding surface. Within the channel,

isolated mesas rise above the channel surface (Fig. 56) and imply that the material around them was preferentially removed by the flow of material through the channel.

The tops of the jagged boundaries on opposite sides of the channel (Fig. 56) are approximately aligned along the regional slope (Fig. 55), suggesting that the surfaces were once physically connected and that the material between them was removed. The eroded mesas within the channel (Fig. 56) likely consist of materials that resisted physical degradation during flow through the channel. An impact crater located at the north end of the elongate mesa in Fig. 56 may have created a locally indurated surface that was resistant to erosion, similar to teardrop shaped islands identified in the Athabasca Valles channel by Burr et al. (2002a, b) that also have an impact crater adjacent to a rounded end of the channel inlier. Burr et al. (2002a, b) inferred a connection between the Athabasca streamlined forms and those in the Channeled Scablands of Washington, USA, indicating a similar aqueous formation mechanism. Accordingly, we also hypothesize that a fluid travelled through the channel (either on the surface or within the shallow subsurface), although its composition was not necessarily water, as has been inferred for Athabasca Valles.

The morphology of the channel boundaries (Fig. 57) is jagged with near-vertical scarps that exhibit cusps, such that the boundaries do not appear sinuous at low amplitudes and long wavelengths like those reported for aqueous megaflooding (e.g., Burr et al., 2002a, b) or lava channels (Leverington, 2004, 2011). The irregularity in morphology of the scarp and the lack of any obvious lava textures on the surface of the channel may imply that a fluid other than water or lava may be responsible for the shape of the channel boundary. We therefore interpret that the indented, cuspate morphology of the channel scarps (Fig. 57), which are eroded into a flanking ridge along the channel margins, was the result of a process other than the effusion of lava flows from the Crater Fossa, as occurred adjacent to, and north of, the fossa. The consistency in morphology of the scarp may indicate that the

lithology of the material that constructed the ridges alongside channel may be easily degraded into an irregular, indented, and cuspate morphology.

We hypothesize that magmatic heat from dike intrusion beneath the Crater Fossa melted ice-rich surface materials, promoting the formation of mass flows that subsequently excavated the channel in Fig. 54. The ridges may represent ice-rich sedimentary deposits that were emplaced as the margins of the mass froze. The marginal deposits may have frozen and evaporated during emplacement due to the low atmospheric pressure and cold Martian conditions, similar to the model proposed for Elysium-Utopia lahars proposed by Pedersen (2013). The ice-rich sedimentary source was likely the crater that is crosscut by a fossa in the northwestern region of Fig. 52. Craters on Mars are very commonly surrounded preserved ejecta blankets. This unconsolidated material is likely to be very porous and may act as a reservoir for ice storage. Dike intrusion promoted melting of this ice, resulting in the mobilization of sediment. The model we present for the formation of mass flows at Crater Fossa is very similar to the sequence of events at other locations in Cerberus Fossae, such as the Valleys in the Hesperian-Noachian transition unit (Fig. 46).

The lithology of the ridges along the channel margins (Fig. 54) that resulted from mass flow through the channel would be more easily erodible than lava. Ice that remained in the ridged deposits after their emplacement may have modified the channel margins and promoted the formation of its irregular, indented, and cuspate morphology (Fig. 57). Similar landforms have been described adjacent to, and immediately south of, the Cerberus Fossae in the region that sourced the megafloods that carved Athabasca Valles (e.g., Fig. 3 of Balme and Gallagher, 2009). A periglacial environment proposed for the formation of a series of cuspate niches and indented surfaces that define sub-circular alcoves similar in morphology to the features we describe along the channel margins south of the Crater Fossa (Fig. 57), suggesting a similar underlying formation process. Balme and Gallagher (2009) support their interpretation of the indented cuspate niches with additional geomorphological evidence that

supports aqueous flow at the surface, including branching valleys, polygonal terrain interpreted to be caused by freeze-thaw processes and cone-mound landforms that suggest formation by pingo genesis.

Balme and Gallagher (2009) propose retrogressive thaw slumping as the process that created the indented niches. Retrogressive thaw slump (RTS) landforms occur in permafrost regions on Earth and are diagnostic of degrading permafrost (Harris, 1981). Three main elements comprise RTS landforms (Lantuit and Pollard, 2008): (1) a steep headwall incised into the active layer (such as the ice-rich layer that experiences seasonal melt), (2) a headscarp which retreats by ablation of permafrost, and (3) the slump floor, which consists of mudflow and debris flow deposits that remain as the permafrost ablates. While the formation process that resulted in the polygonal surfaces and cone mound landforms are disputed (Page, 2010; Jaeger et al., 2007; Burr et al., 2005; Balme et al., 2012), the morphological similarity of indented cuspate niches to terrestrial analogs in degrading permafrost environments that form in response to combined sub-surface and overland flow implies a similar process occurred south of the Athabasca Valles megaflood source along the Cerberus Fossae. Therefore, we propose that the cuspate scarps that delineate the boundary of the channel south of the Crater Fossa (Fig. 57) may also have resulted from the degradation of permafrost and represent a Martian analog to terrestrial RTS landforms. The topographic ridges along the boundaries of the channel may be degraded as a result of its ice content that caused slumping and ablation of permafrost, causing the retreat of the cuspate features headward, perpendicular (E-W) to the inferred down-channel (N-S) direction.

Farther downslope from the part of the channel that shows evidence for retrogressive thaw slumping and fluid flow through and out of the channel, the channel transitions into a different, constructional surface morphology (Fig. 59). The northwest edge of this flow deposit corresponds to the end of the channel where it displays a cuspate flow boundary

(Fig. 58). The surface is comprised of a disrupted and patchy character that exhibits rough and smooth surface textures indicated by surface albedo patterns (Fig. 59). The flow appears somewhat similar to a platy ridged lava flow, in which a plate of ridged material is separated by a lower-lying smooth surface that connects slabs that drifted apart during lava flow emplacement (Keszthelyi et al., 2004). Disparities exist in comparisons between a platy-ridged lava texture and the flow in Fig. 59, however, such as the lack of plates that can discernibly fit back together as “jigsaw” puzzle pieces. The channelization of the flow into three distinct and angular lobes at the southwest termination of the flow deposit is also at odds with a purely volcanic hypothesis. Lavas typically exhibit smooth lobate characteristics at their flow terminations, as they do north of Crater Fossa (Fig. 53; Greeley, 1981). This departure from an expected volcanic flow morphology suggests that a different type of fluid may have flowed through the channel southward from the Crater Fossa, resulting in construction of the flow deposit in Fig. 59.

Gulick (1998) predicted that groundwater mobilized by magmatic heating that reaches the near-surface environment can contribute to the geomorphic modification of that surface. Depending on the local hydrologic and lithologic conditions, surface water may re-enter the groundwater system in regions where infiltration is sufficiently high. Alternatively, if atmospheric temperature and pressure were not favorable to fluid flow, groundwater would initially start to boil and evaporate but then freeze due to the heat liberating process of evaporation. The possibility then exists that an insulating ice layer may form beneath which subsequent outflows of hydrothermal water may move as ice covered rivers (Wallace and Sagan, 1979; Carr, 1983; Brakenridge et al., 1985). We assert that the mass flow sourced from the crater-fossa intersection (Fig. 52) transported a large amount of material (sourced from the crater rim) that was subsequently deposited at the southeastward end of the channel (Fig. 59).

MOLA topographic data suggests that the flow has a thickness that ranges from 10 to 20 m. The constructional nature of the deposit is consistent with the thickness of the levee-like ridges present along the edges of the channel further upstream. We propose that the flow in Fig. 59 experienced plastic deformation of its upper surface, producing ridges and a disrupted texture due to the freezing of the mass flow surface that contained sediment and water. As the flow froze in place, gravitational forces imposed on the ice-sediment mixture created internal and lateral ridges, as well as causing the downstream end of the flow to advance as three independent lobes (Fig. 60). We propose that the mass flow that was deposited at the downstream end of the channel (Fig. 59) was originally sourced from the region closer to the Crater Fossa, and that the channel itself was the result of the mobilization of a mass flow or an ice-rich sediment mixture through the channel system, developing lateral levees during the process. Remnants of a similar flow material may have existed within the channel closer to the fossa, but its flow surface has since degraded as a result of periglacial processes similar to retrogressive thaw slumps (Balme and Gallagher, 2009).

6.4. Summary of observations and interpretations

The observations presented in this study depict a more complex evolutionary sequence of events for the formation of the Cerberus Fossae than has previously been acknowledged. The focus on geomorphic modification in this work indicates that landscape modification was an integral part of fossa formation and should not be considered separately from models that focus only on structural or volcanic processes. We have identified topographically subdued surfaces (depressions, canyons, or channels) adjacent to the fossae that each exhibit unique morphological expressions and can be attributed to specific formation mechanisms. Six field sites have been described in detail that are grouped into three categories based on geomorphic expression: (1) elongate depressions with smooth

surfaces and simple boundaries, (2) terraced, cuspate, and trough-shaped depressions, and (3) channel-carved valleys that appear to have developed as a result of a flowing fluid. The underlying association of these three categories with fossae processes links them genetically; however, the uniqueness of each implies that either separate processes are occurring at each site, or, alternatively, that the disparity in physical appearance is caused by the location where the features develop, the lithologies that they crosscut, and the stage of evolution of the fossa with which they are associated.

We consider surface collapse by mass wasting, mass flows, groundwater flow/sapping, periglacial processes, and lava flows as possible formation mechanisms that created the morphologies adjacent to the fossae. Nonetheless, observations at the six study sites suggest that the entire range of features can be accounted for by one unifying formation model that incorporates several different processes occurring in close association. At each site, we demonstrate that the existence of a fossa and the close association of adjacent lava flow deposits that imply the existence of a magmatic dike. Because magmatic dikes are known to produce depressions above them by normal faulting (Rubin and Pollard, 1988) or collapse within a zone of fractured rock above the tip of a subsurface dike (Mastin and Pollard, 1988), we infer that one or both of these two processes created the fossae. The Hesperian-Noachian unit channel example (Fig. 46) is the only site that is not associated directly with a fossa, but still shows evidence that magmatic intrusion led to its development, with crosscutting relationships indicating that this intrusion was broadly coeval with the Cerberus Fossae volcanic period.

The type of fluid varied between the investigated sites. Some appear to have involved primarily lavas that infilled earlier-formed depressions above subsurface dikes (e.g., the Bathtub Ring Depression Fossa and the Nested Depression Fossa; Figs. 7 and 17). Others appear to have sourced not only lava, but also water that created an erosional channel and deposited an ice-rich flow that was subsequently degraded by periglacial processes (Crater

Fossa; Fig. 52). At the Terraced Depression Fossa (Fig. 30), lobate flow units that were directed away from the flanks of the fossa (Fig. 34) imply early volcanic effusive and depositional processes, followed by incision of these flows by subsurface groundwater flow toward the fossa that resulted in headward erosion and the development of cuspate and trough-shaped depressions alongside the fossa (Figs. 33, 35, and 36). Multiple episodes of groundwater flow resulted in the progressive development of these depressions and the creation of multiple terraces (Fig. 32) within a multi-layered lava sequence that facilitated groundwater flow through a dense fracture network. Drainage likely occurred in toward a developing fossa that progressively widened and deepened, exposing progressively deeper lava flows that became the dominant groundwater flow outlets and terrace formers. The fossa ultimately crosscut the depressions, forming abandoned “hanging valleys” along the fossa walls and implying the final stage of development of the fossa is younger than the terrace-forming events related to groundwater flow.

In contrast, we find evidence at the Orthogonal Protrusion Fossa (Fig. 37) for amphitheater-headed depressions or erosional protrusions into the fossa walls that range in size and scale, are oriented perpendicular to the fossa, and crosscut the fossa walls, indicating they postdate fossa formation (Figs. 41-43). The floors of the protrusions rise gradually from the floor of the fossa, forming ramps up to the uppermost surface (Fig. 43). The protrusions crosscut multiple layers (Figs. 44 and 44) and we interpret the development of stacked terraces as being the result of multiple episodes of subsurface fluid flow, similar to the terraces created by groundwater sapping along the walls of the Terraced Depression Fossa (Fig. 30). Because the protrusions at the Orthogonal Protrusion Fossa crosscut the fossa margins, we infer that groundwater flow occurred either during or after the formation of the fossa. The protrusions also crosscut volcanic deposits on the fossa flanks (Fig. 41), implying that groundwater modified the fossa after volcanism emplaced the deposits that constructed the ridge along the fossa margins (Figs. 37 and 38).

Our interpretations of the observed landforms in the six study sites demonstrate that fossa formation, volcanism, and aqueous flow occurred together in space and time. We show features along the edges of the fossa that are suggestive of aqueous modification by groundwater seepage and flow. Groundwater seepage is proposed here to have incised into the deposits on the flanks of the fossa. Elsewhere, we see evidence that the elongate troughs crosscut by the Bathtub Ring Depression Fossae (BRDF) and Nested Depression Fossae (NDF) likely formed due to melting of ground ice by heat from an underlying dike, and subsequent volume reduction and surface collapse. Following the formation of an elongate depression that mimicked the shape of the underlying dike geometry, lava erupted into the depression forming linear lava lakes that were subsequently crosscut during an episode of surface collapse into an evacuated dike cavity that formed the fossae. The presence of channels within the Hesperian-Noachian transition unit and its association with magmatic intrusions (Fig. 46) imply that magmatic heating of volatiles contained within a loose or granular deposit may have resulted in mass flows. Ambiguous crosscutting relationships between channels and volcanic units sourced from a nearby fossa indicate that multiple flow events carved the channels in the Hesperian-Noachian transition unit.

7. Discussion

7.1. Sequence of events at Cerberus Fossae

Previous studies identified a sequence of events at Cerberus Fossae that included three stages: (1) aqueous megafloods were sourced from the fossae and incised Athabasca, Marte, and Grjotá Valles; (2) volcanic eruptions along the fossae emplaced lavas that superposed fluvially-carved surfaces; and (3) the formation of the Cerberus Fossae fissures that crosscut both megaflood channels and lava surfaces, postdating their eruptions (Burr et al., 2002a,b; Plescia, 2003; Berman and Hartmann, 2002). Head et al. (2003) suggested that following stage 3, the fossae were modified by mass wasting processes associated with late-stage cryospheric melting. This model implies that some component of fossae formation was aided by groundwater flow generated by magma-driven hydrothermal systems and that subsurface groundwater flow occurred after volcanic eruption. Assuming that aqueous flow carved the hypothesized megaflood channels prior to volcanic eruption, water was necessarily mobilized to the surface prior to volcanic eruptions, whereas a portion of the water produced by magma-generated heat continued to reside in the subsurface adjacent to the fossae after volcanism. Although evidence for an aqueous megaflood cause for channel formation has been documented in great detail (Burr et al., 2002a,b; Burr and Parker, 2006), the case for groundwater flow along the Cerberus Fossae that postdates volcanic extrusion has not been verified with geomorphic evidence before now.

Our results demonstrate that subsurface aqueous flow along the Cerberus Fossae occurred after the emplacement of lava flows on the fossa flanks. Given that the Cerberus Fossae formed as a result of dike emplacement and based on the close association of the groundwater features with the fossae, we infer that groundwater flow was driven by magmatic heat prior to volcanism, but which continued after the extrusion of lava, presumably in response to a still-active magmatic system. This heat initially resulted in

elongate depressions at the surface above the intruding dikes in response to melting of ground ice, such as at the Bathtub Ring Depression Fossa (Fig. 7) and Nested Depression Fossa (Fig. 17). Subsequent volcanic eruptions infilled these depressions with lavas, forming elongate lava ponds that partially emptied during eventual breakouts. Although megaflood channels have been identified elsewhere along the Cerberus Fossae that predated a period of major flood volcanism, no such channels (large or small) were observed in the six study sites described here, indicating that profuse water release as catastrophic overland flow was not a characteristic process along the entire Cerberus Fossae during its evolution. Nonetheless, the interpreted large lahar channel and associated deposit south of Crater Fossa likely formed at this stage of fossa evolution.

After volcanic activity ceased, active hydrothermal systems continued to modify the edges of the fossae. Groundwater flow after volcanic eruption is most clearly demonstrated at the Terraced Depression Fossa (Fig. 30) and the Orthogonal Protrusion Fossa (Fig. 37). Elsewhere along the fossae, such as at the Crater Fossa (Fig. 52) and within the Hesperian-Noachian transition unit immediately south of the Orthogonal Protrusion Fossa (Fig. 46), lahars and debris flows contributed to the modification of the landscape, driven by volcanic or magmatic activity. Magmatic intrusions at these locations likely created hydrothermal systems, likely through the melting of ground ice, which promoted the extrusion of water to the surface and resulted in geomorphic modification, including widening of the fossae.

The combined study sites described in this work indicate that a range of processes contributed to the formation of the Cerberus Fossae and the evolution of the adjacent landscape. A conceptual model of the sequence of events at the Cerberus Fossae is shown in Fig. 61 and expands on concepts introduced by Gulick (1998) and Head et al. (2003). In stage 1, magmatic heat provided by dike intrusion melts ground ice immediately above and adjacent to the dike, forming elongate depressions with smooth edges and setting up a subsurface hydrothermal system. Early groundwater sapping would start to create adjacent

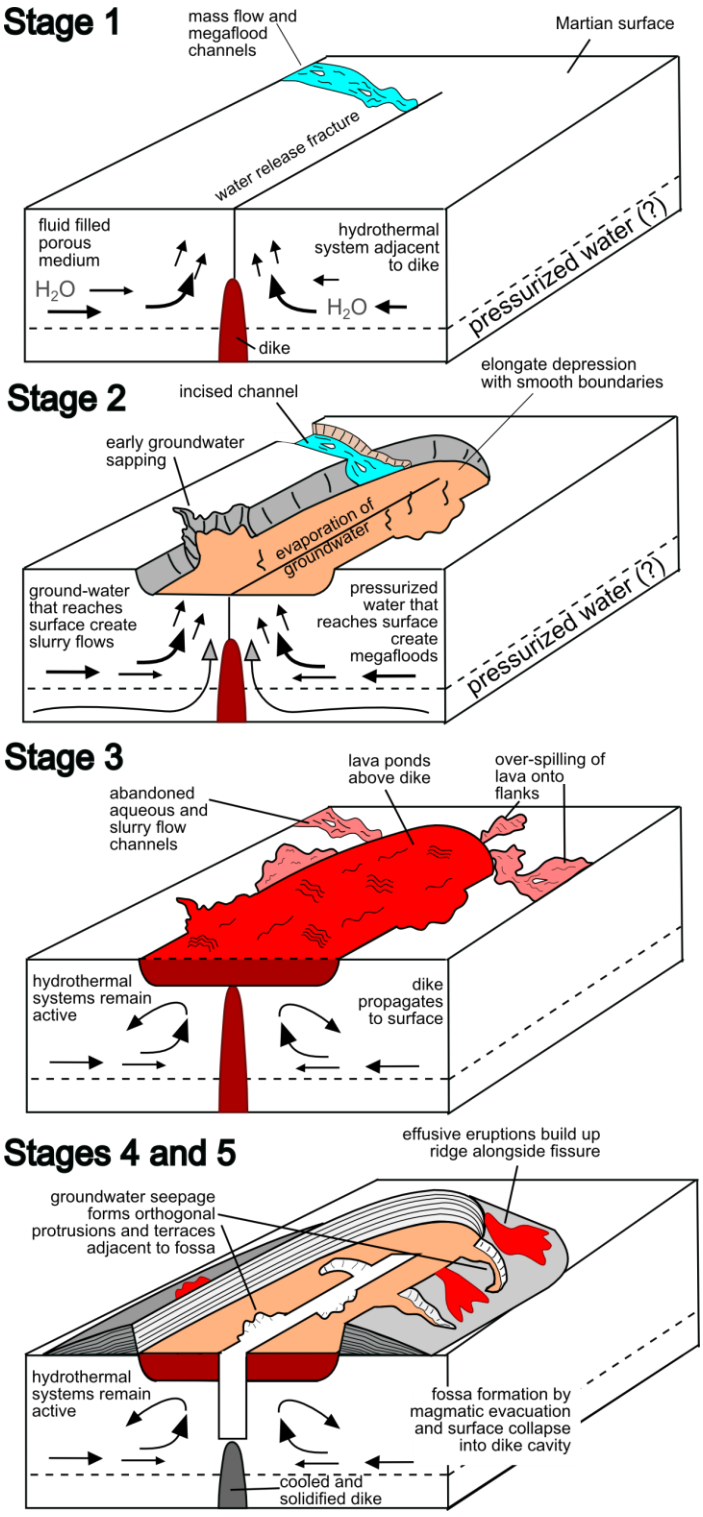

Figure 61. Proposed formation mechanism that accounts for the range of landforms at the Cerberus Fossae. All processes shown are reliant upon the presence of a subsurface magmatic dike and an ice-rich cryosphere that provided fluids mobilized in a hydrothermal system. This generalized model explains some of the interpreted processes and resultant landforms, but does not explain all landforms at Cerberus Fossae.

depressions or terraces with rough edges. During stage 2, water release forms the megaflood channels in some locations, but these are rare. The mechanism of this release remains unknown (Pendleton et al., 2013). Pressurized water effusion is one possibility, but issues remain regarding the instantaneous production of enough water for sustained overland flow under Martian conditions that extends far from the fossae (Leverington, 2011). Also, the creation of large lahar channels and deposits (such as the Crater Fossa) likely occur in stage 2. In stage 3, the dike reaches the surface, with continued effusive eruptions building a ridge alongside the narrow fissure eruption and creating lobate flows away from the fissure. In stages 4 and 5, the edges of the fossae are modified by the groundwater seepage that forms orthogonal protrusions and multiple terraces as the fissure widens. Stages 4 and 5 also shows the deepening and widening fossa progressively being modified by hydrothermal systems driven by the underlying magmatic system. Groundwater flow may contribute to the widening of the fossa as well as producing groundwater flow features such as sapping channels. Development of the fossa in stage 5 results in fossa walls that crosscut the fluvially carved channels, as well as earlier-formed terraces and lava flows deposited on the flanks of the fossa. Deepening of the fossa occurred through an unknown mechanism that may have involved vertical normal faults (e.g., Grant and Kattenhorn, 2004) or dike evacuation in response to a drop in magma pressure. The fossa deepening produced near-vertical walls. Terraces formed by groundwater sapping are crosscut by the fossa walls at the Terraced Depression Fossa (Fig. 32), indicating that a vigorous groundwater flow system was active prior to fossa formation. Nonetheless, groundwater sapping features can also crosscut fossae and their associated lavas, such as in the Orthogonal Protrusion Fossa (Fig. 41), implying that hydrothermal systems in these Martian fossae are long-lived.

7.2. Implications for the development of the Athabasca Valles source region

Pressurized groundwater release from a sub-cryospheric aquifer beneath the Cerberus Fossae is thought to have generated water floods that carved the Athabasca, Marte, and Grjotá Valles megaflood channels. The water may have been catastrophically discharged from the subsurface along dike-generated fractures that manifest as tension cracks or normal faults, although the viability of such a model remains unproven. An additional source of water may be due to melting of the cryosphere by dike intrusion. Craft and Lowell (2012) suggest that hydrothermal convection for a range of dike dimensions and crustal permeabilities could melt a 2-3 km thick permafrost layer or an equivalent volume of pure ice stored beneath the Martian surface over the lifetime of the dike. Circulation of groundwater adjacent to a dike could contribute to the total volume of water released to carve landforms. Hydrothermal systems that circulate groundwater may also saturate near-surface crustal rocks. If magmatic-driven hydrothermal systems were active at the Athabasca Valles source in response to melting of a thick permafrost layer, the fossa margins would likely initially form shallow depressions similar to those described in this study. The mechanism of water delivery to the surface as a geologically instantaneous large volume remains unclear.

7.3. Implications for the development of the Cerberus Fossae

NASA's InSight (Interior Exploration using Seismic Investigations, Geodesy and Heat Transport) is scheduled for launch in March 2016 and will record seismic activity on Mars over the mission's forecast 2-year lifespan. Potential sources of seismic activity include tectonic activity (Anderson et al., 2001), meteorite impacts (Teanby and Wookey, 2011; Davis, 1993), and the so-called "atmospheric hum," which is caused by the excitation of normal modes (Banerdt, 2010; Lognonné, 2009). Faulting is predictably the most reliable of these sources of observable seismic energy (Taylor et al., 2013) and the Cerberus Fossae is

a potential candidate for such activity given its young age and hypothesized development as normal fault graben (Vetterlein and Roberts, 2010). We raise the possibility, however, that the Cerberus Fossae formed through processes unrelated to faulting, such as the evacuation of a wide dike and subsequent modification of the fissure by groundwater flow. If a formation process other than normal faulting is responsible for the Cerberus Fossae, this would not only inform our understanding of the fundamental processes that led to fossae development in central Elysium Planitia, but also about the mechanisms that led to catastrophic water release and the feasibility of present-day tectonically generated seismicity in this location.

7.4. Insights into magma-surface interactions on Mars

Our results represent the first documentation of groundwater sapping caused by enhanced hydrothermal activity on Mars, which was only previously speculated upon (Gulick, 1998; Gulick and Baker, 1990). The tectonic sources of other megaflood channels may have also been modified by groundwater flow processes, such as the Elysium and Galaxias Fossae, which source Hrad Valles (e.g., Fuller and Head, 2002; Pedersen, 2013), and Memnonia Fossae, which sources Mangala Valles (Leask et al., 2007). The Cerberus Fossae are the youngest and best preserved among these; therefore, the groundwater flow features we describe here may be morphological analogs for the early stages of development of these other tectonic megaflood sources.

8. Conclusions

The study sites we document at Cerberus Fossae developed as a result of magmatic dike intrusions and subsequent hydrothermal activity. We document landforms adjacent to the fissures that are reflective of groundwater flow that was driven by magma-induced hydrothermal systems. The presence of groundwater erosional forms adjacent to the fossae requires a source for the liquid as well as a mechanism by which the volatiles were mobilized. Ground ice in a cryosphere contained near the surface is the most reasonable water source. Dike driven hydrothermal systems could have caused the circulation of heat and the production of fluids (cf. Head et al., 2003; Craft and Lowell, 2012). Alternatively, cracking of the cryosphere upon initial dike intrusion may have generated faults that penetrated a pressurized sub-cryospheric aquifer and mobilized groundwater to near-surface layers. The melting of ground ice by magmatic dikes likely resulted in the mobilization of fluids to the surface that were subsequently lost to the atmosphere, resulting in a relative volume loss in the crustal materials and the formation of depressions above the subsurface dikes. The morphology of depression surfaces is consistent with a volcanic interpretation and we infer that the fissures erupted lava into the depressions forming elongate lava lakes. As eruptive processes continued, lava flows were emplaced on the flanks of the fossa that were subsequently incised into by groundwater flow processes.

The formation of the Cerberus Fossae occurred through collapse processes that resulted from magmatic evacuation of underlying dikes, contradicting past hypotheses that they represent normal fault graben (e.g., Berman and Hartmann, 2002; Burr et al., 2002a, b; Taylor et al., 2013; Vetterlein and Roberts, 2010). The presence of groundwater erosion features crosscut by the fossae implies that the magmatic heat source melted ice and mobilized water prior to the fossae formation by either a tectonic or volcanic collapse process. The continued modification of the fossae by groundwater after their formation implies that residual heat from the dike intrusion that created the fossae permitted a long-

lived hydrothermal system. Alternatively, multiple dike injection events during and after the formation of the fossae may have maintained the active groundwater circulation system adjacent to the fossae. Given the young age of the Cerberus Fossae, our results imply that groundwater flow occurred in the very Late Amazonian. This result places the Cerberus Fossae as one of the most recent hydrothermally active sites on Mars, potentially making it a strong target for consideration of astrobiological potential and a habitable environment.

References

Anderson, R. C., James M. D., Golombek, M. P., Haldemann A. F. C., Franklin, B. J., Tanaka, K. L., Lias, J., Peer, B., 2001. Primary centers and secondary concentrations of tectonic activity through time in the western hemisphere of Mars. J. of Geophys. Res. 106, E9, 20563-20585. http://dx.doi.org/10.1029/2000JE001278.

Baker, V. R., Strom, R. G., Gulick, V. C., Kargel, J. S., Komatsu, G., Kale, V. S., 1991. Ancient oceans, ice sheets and the hydrological cycle on Mars. Nature 352, 589–594. http://dx.doi.org/10.1038/352589a0.

Baker, V. R., Carr, M. H., Gulick, V. C., Williams, C. R., Marley, M. S., 1992. Channels and valley networks. In: Mars, Ed: Kieffer, H. H., et al., 493–522, Univ. of Ariz. Press, Tucson.

Baker, V. R. (2001), Water and the Martian landscape, Nature, 412, 228–236. http://dx.doi.org/10.1038/35084172.

Balme, M. R., Gallagher, C. J., 2009. An equatorial periglacial landscape on Mars. Earth and Planetary Science Letters 285, 1-15. http://dx.doi.org/10.1016/j.epsl.2009.05.031.

Balme, M. R., Gallagher, C. J., Hauber, E., 2012. Morphological evidence for geologically young thaw of ice on Mars: A review of recent studies using high-resolution imaging data. Progress in Physical Geography 37, 3, 289-324. http://dx.doi.org/10.1177/0309133313477123.

Banerdt, B., 2010. Innovative approaches for seismic studies of Mars. American Geophysical Union, Abstract U41A-04, San Francisco, CA, USA.

Baross, J. A., Hoffman, S. E., 1985. Submarine hydrothermal vents and associated gradient environments as sites for the origin and evolution of life. Orig. Life 15, 327–345. http://dx.doi.org/10.1007/BF01808177.

Berman, D. C., Hartmann, W. K., 2002. Recent fluvial, volcanic, and tectonic activity on the Cerberus plains of Mars. Icarus 159, 1-17, http://dx.doi.org/10.1006/icar.2002.6920.

Blackburn, E.A., Wilson, L., and Sparks, R.S.J., 1976. Mechanisms and dynamics of Strombolian activity. Journal of the Geological Society of London 132, 429–440. http://dx.doi.org/10.1144/gsjgs.132.4.0429.

Bleacher, J. E., Greeley, R., Williams, D. A., Cave, S. R., Neukum, G., 2007. Trends in effusive style at the Tharsis Montes, Mars, and implications for the development of the Tharsis province. Journal of Geophysical Research-Planets 112, E09005. http://dx.doi.org/10.1029/2006JE002873.

Brakenridge, G. R., Newsom, H. E., Baker, V. R., 1985. Ancient hot springs on Mars: Origins and paleoenvironmental significance of small Martian valleys. Geology 13, 859-862. http://dx.doi.org/10.1130/0091-7613(1985)13<859:AHSOMO>2.0.CO;2.

Burr, D. M., Grier, J. A., McEwen, A. S., Keszthelyi, L. P., 2002a. Repeated aqueous flooding from the Cerberus Fossae: Evidence for very recently extant, deep groundwater on Mars. Icarus 159, 53-73. http://dx.doi.org/10.1006/icar.2002.6921.

Burr, D. M., McEwen, A. S., Sakimoto, S. E. H., 2002b. Recent aqueous floods from the Cerberus Fossae, Mars. Geophys. Res. Lett., 29(1). http://dx.doi.org/10.1029/2001gl013345. 041029_001.

Burr, D. M., Carling, P. A., Beyer, R. A., Lancaster, N., 2004. Flood-formed dunes in Athabasca Valles, Mars: morphology, modeling, and implications. Icarus 171, 68-83. http://dx.doi.org/10.1016/j.icarus.2004.04.013.

Burr D. A., Soare R. J., Tseung J., Emery J. P., 2005. Young (late Amazonian), near-surface, ground ice features near the equator, Athabasca Valles, Mars. Icarus 178, 56-73. http://dx.doi.org/10.1016/j.icarus.2005.04.012.

Carr, M. H., 1983. Stability of streams and lakes on Mars. Icarus 56, 476-495.

Carr, M. H., 1973. Volcanism on Mars. J. Geophys. Res. 78, 4049–4062. http://dx.doi.org/10.1029/JB078i020p04049.

Chapman, M. G., Tanaka, K. L., 2002. Related Magma–Ice Interactions: Possible Origins of Chasmata, Chaos, and Surface Materials in Xanthe, Margaritifer, and Meridiani Terrae, Mars. Icarus 2, 324-339. http://dx.doi.org/10.1006/icar.2001.6735.

Christiansen, E. H., Greeley, R., 1981. Mega-lahars in the Elysium region, mars. Planetary Science, vol. XII. Lunar and Planetary Institute, Houston, TX, USA, 138-140.

Christiansen, E. H., 1989. Lahars in the Elysium region of Mars. Geology 17, 3, 203-206. http://dx.doi.org/10.1130/0091-7613(1989)017<0203:LITERO>2.3.CO;2.

Christensen, P. R., Jakosky, B., Kieffer, H. H., Malin, M. C., McSween, H. Y., Nealson, K., Mehall, G. L., Silverman, S. H., Ferry, S., Caplinger, M., et al., 2004. The Thermal Emission Imaging System (THEMIS) for the Mars 2001 Odyssey Mission. Space Science Reviews 110(1-2), 85-130.

Coleman, N. M., 2003. Aqueous flows carved the outflow channels on Mars. J. Geophys. Res. 108, E5, 5039. http://dx.doi.org/10.1029/2002JE001940.

Craddock, R., Maxwell, T., 1993. Geomorphic evolution of the Martian highlands through ancient fluvial processes. J. Geophys. Res. 98, 3453–3468. http://dx.doi.org/10.1029/92JE02508.

Craft, K. L., Lowell, R. P., 2012. Boundary layer models of hydrothermal circulation on Mars and its relationship to geomorphic features. J. Geophys. Res. 117, E05006. http://dx.doi.org/10.1029/2012JE004049.

Davis, P. M., 1993. Meteoroid impacts as seismic sources on Mars. Icarus 105, 469-478. http://dx.doi.org/10.1006/icar.1993.1142.

Dundas, C. M., Keszthelyi, L. P., 2013. Modeling steam pressure under martian lava flows. Icarus 226. http://dx.doi.org/10.1016/j.icarus.2013.06.036.

Dunne, T., 1980. Formation and controls of channel networks. Progress in Physical Geography 4, 211-239.

Dunne, T., 1990. Hydrology, mechanics, and geomorphic implications of erosion by subsurface flow. Geol. Soc. America Special Paper 252, 1-28.

Elderfield, H., Schultz, A., 1996. Mid-ocean ridge hydrothermal fluxes and the chemical composition of the ocean. Annu. Rev. Earth Planet. Sci. 24, 191–224. http://dx.doi.org/10.1146/annurev.earth.24.1.191.

Fagents, S. A., Lanagan, P., Greeley, R., 2002. Rootless cones on Mars: A consequence of lava–ground ice interaction. In:Volcano–Ice Interaction on Earth and Mars, Eds: Smellie, J. L., Chapman, M. G., Geological Society, London, Special Publications, 202, 295–317. http://dx.doi.org/10.1144/GSL.SP.2002.202.01.15.

Fagents, S.A., Thordarson, T., 2007. Rootless volcanic cones in Iceland and on Mars. In: The Geology of Mars: Evidence from Earth-Based Analogs, Ed: Chapman, M., Cambridge University Press. http://dx.doi.org/10.1017/CBO9780511536014.007.

Fanale, F. P., 1976. Martian volatiles: Their degassing history and geochemical fate. Icarus 28, 179-202.

Fuller, E. R., Head, J. W., 2002. Amazonis Planitia: The role of geologically recent volcanism and sedimentation in the formation of the smoothest plains on Mars. J. Geophys. Res. 107(E10), 5081. http://dx.doi.org/10.1029/2002je001842.

Gasparini, P., Mantovani, M. S. M., 1984. Heat transfer in geothermal areas. In: Geophysics of Geothermal Areas: State of the Art and Future Development, Ed: Rapolla, A., Keller, G. V., 9-40, Co. Sch. of Mines Press, Golden, Colorado.

Goldspiel, J. M., Squyres, S. W., 2002. Groundwater sapping and valley formation on Mars. Icarus 148, 176-192.

Grant, J. V., Kattenhorn, S. A., 2004. Evolution of vertical faults at an extensional plate boundary, southwest Iceland. J. Struct. Geol. 26, 537-557. http://dx.doi.org/10.1016/j.jsg.2003.07.003.

Greeley, R., 1977. Volcanism of the Eastern Snake River Plain, Idaho. NASA Contract. Rep., CR-154621, 23-43.

Greeley, R., Spudis, P. D., 1981. Volcanism on Mars. Rev. Geophys., 19(1), 13-41. http://dx.doi.org/10.1029/RG019i001p00013.

Greeley, R., Guest, J. E., 1987. Geologic Map of the Eastern Equatorial Region of Mars, U.S. Geol. Surv. Misc. Invest. Ser. Map I-1802-B.

Greeley, R., Fagents, S.A., 2001. Icelandic pseudocraters as analogs to some volcanic cones on Mars. J. Geophys. Res. 106(E9), 20527–20546. http://dx.doi.org/10.1029/2000JE001378.

Gulick, V. C., 1993. Magmatic intrusions and hydrothermal systems: Implications for the formation of Martian fluvial valleys. PhD thesis, Univ. of Ariz., Tucson.

Gulick, V. C., Baker, V. R., 1993. Fluvial erosion on Mars: Implications for paleoclimatic change. 24th Lunar Planetary Science Conference proceedings, Abstr. #1295.

Gulick, V. C., Tyler, D., McKay, C. P., Haberle, R. M., 1997. Episodic ocean-induced CO2 pulses on Mars: Implications for fluvial valley formation. Icarus 130, 68–86. http://dx.doi.org/10.1006/icar.1997.5802.

Gulick, V. C., Baker, V. R., 1990. Origin and evolution of valleys on Martian volcanoes. J. Geophys. Res. 95(B9), 14325-14344. http://dx.doi.org/10.1029/JB095iB09p14325.

Gulick, V. C., 1998. Magmatic intrusions and a hydrothermal origin for fluvial valleys on Mars. J. Geophys. Res. 103(E3), 19365-19387. http://dx.doi.org/10.1029/98JE01321.

Hartmann, W. K., Neukum, G., 2001. Cratering chronology and the evolution of Mars. Space Sci. Rev. 96, 165-194.

Hamilton, C. W., Fagents, S. A., Wilson, L., 2010. Explosive lava–water interactions in Elysium Planitia, Mars: Geologic and thermodynamic constraints on the formation of the Tartarus Colles cone groups. J. Geophys. Res. 115, E09006. http://dx.doi.org/10.1029/2009JE003546.

Hamilton, C. W., Fagents, S. A., Thordarson, T., 2011. Lava–ground ice interactions in Elysium Planitia, Mars: Geomorphological and geospatial analysis of the Tartarus Colles cone groups. J. Geophys. Res. 116, E03004. http://dx.doi.org/10.1029/2010JE003657.

Hanna, J. C., Phillips, R. J., 2006. Tectonic pressurization of aquifers in the formation of Mangala Valles, Mars. J. Geophys. Res. 111, E03003, http://dx.doi.org/10.1029/2005JE002546.

Harris, C., 1981. Periglacial mass-wasting: a review of research. GeoAbstracts, Norwich.

Hauber, E., Bleacher, J., Gwinner, K., Williams, D., Greeley, R., 2009. The topography and morphology of low shields and associated landforms of plains volcanism in the Tharsis region of Mars. J. Volc. Geotherm. Res. 185, 69-95. http://dx.doi.org/10.1016/j.jvolgeores.2009.04.015.

Head, J. W., Wilson, L., Mitchell, K. L., 2003. Generation of recent massive water floods at Cerberus Fossae, Mars by dike emplacement, cryospheric cracking, and confined aquifer groundwater release. Geophys. Res. Lett. 30, 1577, http://dx.doi.org/10.1029/2003gl017135.

Hon, K., Kauahikaua, J., Denlinger, R., and Mackay, K., 1994. Emplacement and inflation of pahoehoe sheet flows; observations and measurements of active lava flows on Kilauea Volcano, Hawaii. Geological Society of America Bulletin, 106, 351–370, http://dx.doi.org/10.1130/0016-7606(1994)106<0351:EAIOPS>2.3.CO;2.

Howard, A. D., McLane, C. F., 1988. Erosion of cohesionless sediment by groundwater seepage. Water Res. Res. 24, 10, 1659-1674. http://dx.doi.org/10.1029/WR024i010p01659.

Jaeger, W. L., Keszthelyi, L. P., McEwen, A. S., Dundas, C. M., Russel, P. S., 2007. HiRISE observations of Athabasca Valles, Mars: A lava-draped channel system. Science 317, 1709–1711. http://dx.doi.org/10.1126/science.1143315.

Jaeger W. L., Keszthelyi L. P., Skinner J. A., Milazzo M. P., McEwen A. S., Titus T. N., Rosiek M. R., Galuszka D. M., Howington-Kraus E., Kirk R. L., et al. . 2010. Emplacement of the youngest flood lava on Mars: A short, turbulent story. Icarus 205, 230-243. http://dx.doi.org/10.1016/j.icarus.2009.09.011.

Jakosky, B. M., Phillips, R. J., 2001. Mars' volatile and climate history. Nature 412, 237–244. http://dx.doi.org/10.1038/35084184.

Jerram, D. A., Widdowson, M., 2005. The anatomy of Continental Flood Basalt Provinces: geological constraints on the processes and products of flood volcanism. Lithos 79, 385-405.

Keszthleyi, L. P., Pieri, D. C., 1993. Emplacement of the 75-km-long Carrizozo lava flow field, south-central New Mexico. J. Volc. Geotherm. Res. 59, 59-75.

Keszthelyi, L., McEwen, A. S., Thordarson, T., 2000. Terrestrial analogs and thermal models for Martian flood lavas. J. Geophys. Res. 105(E6), 15027-15049. http://dx.doi.org/10.1029/1999JE001191.

Keszthelyi, L., Thordarson, T., McEwen, A., Haack, H., Guilbaud, M. N., Self, S., Rossi, M.J., 2004. Icelandic analogs to Martian flood lavas. Geochem. Geophys. Geosyst. 5, Q11014. http://dx.doi.org/10.1029/2004GC000758.

Keszthelyi, L. P., Denlinger, R. P., O'Connell, D. R. H., Burr, D. M., 2007. Initial insights from 2.5D hydraulic modeling of floods in Athabasca Valles, Mars. Geophys. Res. Lett., 34, L21206. http://dx.doi.org/10.1029/2007GL031776.

Keszthelyi, L., Jaeger, W., McEwen, A., Tornabene, L., Beyer, R. A., Dundas, C., Milazzo, M. , 2008. High Resolution Imaging Science Experiment (HiRISE) Images of Volcanic Terrains from the First 6 Months of the Mars Reconnaissance Orbiter Primary Science Phase. J. Geophys. Res., 113, E04005. http://dx.doi.org/10.1029/2007JE002968.

Keszthelyi, L. P., Jaeger, W. L., Dundas, C. M., Martinez-Alonso, S., McEwen, A. S., Milazzo, M. P., 2010. Hydrovolcanic features on Mars: Preliminary observations from the first Mars year of HiRISE imaging. Icarus 205, 211–229. http://dx.doi.org/10.1016/j.icarus.2009.08.020.

Kochel, R. C., Piper, J. F., 1986. Morphology of large valleys on Hawaii: Evidence for groundwater sapping and comparisons with Martian valleys. J. Geophys. Res. 91(B13), E175–E192. http://dx.doi.org/10.1029/JB091iB13p0E175.

Laity, J. E., Malin, M. C., 1985. Sapping processes and the development of theater-headed valley networks on the Colorado Plateau. Geological Society of America Bulletin, 96, 2, 203-217. http://dx.doi.org/10.1130/0016-7606(1985)96<203:SPATDO>2.0.CO;2.

Lanagan, P. D., McEwen, A. S., Keszthelyi, L. P., Thordarson, T., 2001. Rootless cones on Mars indicating the presence of shallow equatorial ground ice in recent times. Geophys. Res. Lett., 28, 12, 2365-67. http://dx.doi.org/10.1029/2001gl012932.

Lantuit, H., Pollard, W. H., 2008. Fifty years of coastal erosion and retrogressive thaw slump activity on Herschel Island, southern Beaufort Sea, Yukon Territory, Canada.

Geomorphology 95, 84–102.

Lavigne, F., Thouret, J.-C., 2000. Les lahars: depots, origins et dynamique. Bulletin de la Societe Geologique de France 171(5), 545–557.

Leask, H. J., Wilson, L., Mitchell, K. L., 2006. Formation of Aromatum Chaos, Mars: Morphological development as a result of volcano-ice interactions. J. Geophys. Res. 111, E08071. http://dx.doi.org/10.1029/2005JE002549.

Leask, H. J., Wilson, L., Mitchell, K. L., 2007. Formation of Mangala Valles outflow channel, Mars: Morphological development and water discharge and duration estimates. J. Geophys. Res. 112, E08003. http:/dx.doi.org/10.1029/2006JE002851.

Leverington, D. W., 2004. Volcanic rilles, streamlined islands, and the origin of outflow channels on Mars. J. Geophys. Res. 109, E10011. http://dx.doi.org/10.1029/2004JE002311.

Leverington, D.W., 2011. A volcanic origin for the outflow channels of Mars: Key evidence and major implications. Geomorphology 132, 3-4, 51-75.

Lognonné, P., 2005. Planetary seismology. Annu. Rev. Earth Planet. Sci., 33, 571–604. http://dx.doi.org/10.1146/annurev.earth.33.092203.122604.

Lowell, R., 1991. Modeling continental and submarine hydrothermal systems. Rev. Geophys. 29(3), 457–476. http://dx.doi.org/10.1029/91RG01080.

Lowell, R. P., Rona, P. A., 2004. Tectonics/Hydrothermal activity. In: Encyclopedia of Geology, Ed: Selley, R. C., Cocks, L. R. M., Plimer, I. R., pp. 362–372, Elsevier, Oxford, U.K.

Malin, M. C., Bell III J. F., Cantor, B. A., Caplinger, M. A., Calvin, W. M., Clancy, R. T., Edgett, K. S., Edwards, L., Haberle, R. M., James, P. B., et al., 2007. Context Camera Investigation on board the Mars Reconnaissance Orbiter. J. Geophys. Res., 112, E05S04. http://dx.doi.org/10.1029/2006je002808.

Marra, W. A., Braat, L., Baar, A. W., Kleinhans, M. G., 2014. Valley formation by groundwater seepage, pressurized groundwater and crater-lake overflow in flume experiments with implications for Mars. Icarus 232, 97-117.

Mastin, L. G., Pollard, D. D., 1988. Surface deformation and shallow dike intrusion proceses at Inyo Craters, Long Valley, California. J. Geophys. Res. 93(B11), 13221-13235. http://dx.doi.org/10.1029/JB093iB11p13221.

Mattox, T. N., Heliker, C., Kauahikaua, J., Hon, K., 1993. Development of the 1990 Kalapana Flow Field, Kilauea Volcano, Hawaii. Bulletin of Volcanoloy 55, 6, 407-413.

McEwen, A. S., Preblich, B. S., Turtle, E. P., Artemieva, N. A., Golombek, M. P., Hurst, M., Kirk, R. L., Burr, D. M., Christensen, P. R., 2005. The rayed crater Zunil and interpretations of small impact craters on Mars. Icarus 176, 351–381.

McEwen, A. S., Eliason, E. M., Bergstrom, J. W., Bridges, N. T., Hansen, C. J., Delamere, W. A., Grant, J. A., Gulick, V. C., Herkenhoff, K. E., Keszthelyi, L., et al., 2007. Mars Reconnaissance Orbiter's High Resolution Imaging Science Experiment (HiRISE). J. Geophys. Res., 112, E05S02. http://dx.doi.org/10.1029/2005je002605.

Mège, D., Masson, P., 1996. A plume tectonics model for the Tharsis province, Mars. Planet. Space Sci. 44, 1499–1546. http://dx.doi.org/10.1016/S0032-0633(96)00113-4.

Mège, D., Cook, A. C., Garel, E., Lagabrielle, Y., Cormier, M.-H., 2003. Volcanic rifting at Martian grabens. J. Geophys. Res., 108, E5, 5044. http://dx.doi.org/10.1029/2002JE001852.

Mouginis-Mark, P. J., 1990. Recent water release in the Tharsis region of Mars. Icarus 84, 362–373. http://dx.doi.org/10.1016/0019-1035(90)90044-A.

Neukum, G., Jaumann, R., Hofmann, H., Hauber, E., Head, J. W., Basilevsky, A. T., Ivanov, B. A., Werner, S. C., van Gasselt, S., Murray, J. B., McCord, T., The HRSC Co-Investigator Team. Nature 432. 971-979. http://dx.doi.org/ 10.1038/nature03231.

Nummedal, D., Prior, D. B., 1981. Generation of Martian chaos and channels by debris flows. Icarus 45, 77-86.

Neumann, G., Rowlands, D., Lemoine, F., Smith, D., Zuber, M., 2001. Crossover analysis of Mars Orbiter Laser Altimeter data. J. Geophys. Res., 106(E10), 23753-23768. http://dx.doi.org/10.1029/2000JE001381.

Okubo, C. H., Martel, S. J., 1998. Pit crater formation on Kilauea volcano, Hawaii. J. Volc. Geotherm. Res. 86, 1-18.

Page, D. P., 2010. Resolving the Elysium Controversy: An open invitation to explain the evidence. Planetary and Space Science 58, 10, 1406-1413.

Pedersen, G. B. M., 2013. Frozen Martian lahars? Evaluation of morphology, degradation and geologic development in the Utopia-Elysium transition zone. Planetary and Space Science 85, 59-77.

Pendleton, M. W., Kattenhorn, S. A., Burr, D. M., 2013. Unraveling the formation mechanisms of the Cerberus Fossae, Mars. Geological Society of America Abstracts with Programs. Vol. 45, No. 7, p.296

Platz, T., Michael, G., 2011. Eruption history of the Elysium Volcanic Province, Mars, Earth Planet. Sci. Lett. 312, 140-51. http://dx.doi.org/10.1016/j.epsl.2011.10.001.

Plescia, J. B., 1990. Recent Flood Lavas in the Elysium Region of Mars. Icarus 88, 465-490. http://dx.doi.org/D10.1016/0019-1035(90)90095-Q.

Plescia, J. B., 2003. Cerberus Fossae, Elysium, Mars: a source for lava and water. Icarus 164, 79-95. http://dx.doi.org/10.1016/s0019-1035(03)00139-8.

Pollack, J. B., Kasting, J. F., Richardson, S. M., Poltakoff, K., 1987. The case for a wet, warm climate on early Mars. Icarus 39, 88–110.

Reidel, S. P., 1998, Emplacement of Columbia River flood basalt. J. Geophys. Res. 103 (B11), 27393-27410.

Richardson, J. A., Bleacher, J. E., Glaze, L. S., 2013. The volcanic history of Syria Planum, Mars. J. Volc. Geotherm. Res. 252, 1-13.

Rodriguez, J. A. P., Kargel, J., Crown, D. A., Bleamaster III, L. F., Tanaka, K. L., Baker, V., Miyamoto, H., Dohm, J. M., Sasaki, S., Komatsu, G., 2006. Headward growth of chasmata by volatile outbursts, collapse, and drainage: Evidence from Ganges chaos, Mars. Geophys. Res. Lett., 33, L18203. http://dx.doi.org/10.1029/2006GL026275.

Rossbacher, L. A., Judson, S., 1981. Ground ice on Mars: Inventory, distribution, and resulting landform. Icarus 45, 39-59.

Rowland, S. K., Munro, D. C., 1993. The 1919-1920 eruption of Mauna Iki, Kilauea: chronology, geologic mapping, and magma transport mechanisms. Bulletin of Volcanology 55, 3, 190-203.

Rubin, A. M., Pollard, D. D., 1988. Dike-induced faulting in rift zones of Iceland and Afar. Geology 16, 5, 413-417. http://dx.doi.org/10.1130/0091-7613(1988)016<0413:DIFIRZ>2.3.CO;2.

Rubin, A., 1992. Dike-induced faulting and graben subsidence in volcanic rift zones. J. Geophys. Res. 97 (B2), 1839-1858.

Russell, P. S., Head, J. W., 2003. Elysium-Utopia flows as mega-lahars: A model of dike intrusion, cryosphere cracking, and water-sediment release. J. Geophys. Res. 108(E6). http://dx.doi.org/10.1029/2002JE001995.

Schumm, S., Boyd, K., Wolff, C., Spitz, W., 1995. A ground-water sapping landscape in the Florida Panhandle. Geomorphology 12, 281–297. http://dx.doi.org/10.1016/0169-555X(95)00011-S.

Self, S., Keszthelyi, L., Thordarson, T., 1998. The importance of pahoehoe. Annu. Rev. Earth Planet. Sci., 26 81–110. http://dx.doi.org/10.1146/annurev.earth.26.1.81.

Sharp, R. P., 1973. Mars: Fretted and chaotic terrains. J. Geophys. Res. 78(20), 4073–4083. http://dx.doi.org/10.1029/JB078i020p04073.

Smith, G. A., Fritz, W. J., 1989. Volcanic influences on terrestrial sedimentation. Geology 17, 375–376. http://dx.doi.org/10.1130/0091-7613(1989)017o0375:VIOTS42.3CO;2.

Smith, D.E., Neumann, G.A., Ford, P.G., Arvidson, R.E., Guinness, E.A., Slavney, S., 2003. Mars Global Surveyor Laser Altimeter Precision Experiment Data Record. MGS-MMOLA-3-PEDR-L1A-V1.0, NASA Planetary Data System.

Soderblom, L. A., Wenner, D. B., 1978. Possible fossil H2O liquid–ice interfaces in the martian crust. Icarus 34, 622–637.

Tanaka, K. L., Scott, D. H., 1986. The youngest channel system on Mars. 17th Lunar and Planetary Science Conference, 865-66.

Tanaka, K. L., Chapman, M. G., Scott, D. H. 1992. Geologic map of the Elysium region of Mars. U.S. Geol. Surv. Misc. Invest. Ser. Map I-2147.

Tanaka, K. L., Skinner, J. A., Hare, T. M., 2005. Geologic map of the Northern Plains of Mars. U.S. Geol. Surv. Misc. Invest. Ser. Map I-2811.

Tanaka, K. L., Robins, S. J., Fortezzo, C. M.,Skinner Jr., J. A., Hare, T. M., 2014. The digital global geologic map of Mars: Chronostratigraphic ages, topographic and crater morphologic characteristics, and updated resurfacing history. Planetary and Space Science 95, 11-24.

Taylor, J., Teanby, N. A., Wookey, J., 2013. Estimates of seismic activity in the Cerberus Fossae region of Mars. J. Geophys. Res. Planets, 118, 2570–2581, http://dx.doi.org/10.1002/2013JE004469.

Teanby, N. A., Wookey, J., 2011. Seismic detection of meteorite impacts on Mars. Phys. Earth Planet. Inter., 186, 70–80.

Tentler, T., Mazzoli, S., 2005. Architecture of normal faults in the rift zone of central north Iceland. J. Struct. Geol. 27, 1721-1739. http://dx.doi.org/10.1016/j.jsg.2005.05.018

Thomas, R. J., 2013. Identification of possible recent water/lava source vents in the Cerberus plains: Stratigraphic and crater count age constraints. J. Geophys. Res. Planets, 118, 789-802. http://dx.doi.org/10.1002/jgre.20071.

Thorarinsson, S., 1953. The Crater Groups in Iceland. Bulletin of Volcanology 14, 3-44.

Vallence, J. W., 2000. Lahars. In: Encyclopedia of Volcanoes, Eds: Sigurdsson, H., Houghton, B. F., McNutt, S. R., Rymer, H., Stix, J., Academic Press, 601–616.

Vallence, J. W., Scott, K. M., 1997. The osceola mudflow from mount Rainier: Sedimentology and hazard implications of a huge clay-rich debris flow. Geological Society of America Bulletin 109(2), 143–163. http://dx.doi.org/10.1130/0016-7606(1997)109<0143:TOMFMR>2.3.CO;2.

Vaucher, J., Baratoux, D., Mangold, N., Pinet, P., Kurita, K., Gregoire, M., 2009a. The volcanic history of central Elysium Planitia: Implications for martian magmatism. Icarus 204, 418-42. http://dx.doi.org/10.1016/j.icarus.2009.06.032.

Vaucher, J., Baratoux, D., Toplis, M. J., Pinet, P., Mangold, N., Kurita, K., 2009b. The morphologies of volcanic landforms at Central Elysium Planitia: Evidence for recent and fluid lavas on Mars, Icarus 200, 39-51. http://dx.doi.org/10.1016/j.icarus.2008.11.005.

Vetterlein, J., Roberts, G. P., 2009. Postdating of flow in Athabasca Valles by faulting of the Cerberus Fossae, Elysium Planitia, Mars. J. Geophys. Res. 114, E07003. http://dx.doi.org/10.1029/2009JE003356.

Vetterlein, J., Roberts, G. P., 2010. Structural evolution of the Northern Cerberus Fossae graben system, Elysium Planitia, Mars. J. Struct. Geol., 32, 4, 394-406. http://dx.doi.org/10.1016/j.jsg.2009.11.004.

Walker, G. P. L., 1991. Structure, and origin by injection of lava under surface crust, of tumuli, ‘‘lava rises’’, ‘‘lava-rise pits’’, and ‘‘lava-inflation clefts’’ in Hawaii. Bulletin of Volcanology, 53, 546-558.

Wallace, D., Sagan, C., 1979. Evaporation of ice in planetary atmospheres: Ice-covered rivers on Mars. Icarus 39, 385-400.

Werner, S. C., van Gasselt, S., Neukum, G., 2003. Continual geological activity in Athabasca Valles, Mars. J. Geophys. Res., E12, 108, 8081. http://dx.doi.org/10.1029/2002JE002020.

Whitehead, P. W., Stephenson, P. J., 1998. Lava rise ridges of the Toomba basalt flow, north Queensland, Australia. J. Geophys. Res., 103, 27371-27382. http://dx.doi.org/10.1029/98JB00029.

Wilson, L., Head III, J. W., 2002. Tharsis-radial graben systems as the surface manifestation of plume-related dike intrusion complexes: Models and implications. J. Geophys. Res. 107(E8), http://dx.doi.org/10.1029/2001JE001593.

Zegers, T. E., Oosthoek, J. H. P., Rossi, A. P., Blom, J. K., Schumacher, S., 2010. Melt and collapse of buried water ice: An alternative hypothesis for the formation of chaotic terrains on Mars. Earth Planet Sci. Lett. 297, 3-4, 496-504. http://dx.doi.org/10.1016/j.epsl.2010.06.049.